A MONTE CARLO APPROACH TO DOMINANT SCATTERER TRACKING OF A SINGLE EXTENDED TARGET IN HIGH RANGE-RESOLUTION RADAR

by

Allan De Freitas

Submitted in partial fulfilment of the requirements for the degree

Master of Engineering (Electronic Engineering)

in the

Department of Electrical, Electronic and Computer Engineering
Faculty of Engineering, Built Environment and Information Technology
UNIVERSITY OF PRETORIA

April 2013

SUMMARY

A MONTE CARLO APPROACH TO DOMINANT SCATTERER TRACKING OF A SINGLE EXTENDED TARGET IN HIGH RANGE-RESOLUTION RADAR

by

Allan De Freitas

Supervisor(s):	Dr. J.P. de Villiers & Mr. W.A.J. Nel
Department:	Electrical, Electronic and Computer Engineering
University:	University of Pretoria
Degree:	Master of Engineering (Electronic Engineering)
Keywords:	Extended Target, tracking, high range-resolution radar, high range-resolution profile, particle filtering, ISAR, particle Markov chain Monte Carlo, particle marginal Metropolis-Hastings sampler, static parameter estimation

In high range-resolution (HRR) radar systems, the returns from a single target may fall in multiple adjacent range bins which individually vary in amplitude. A target following this representation is commonly referred to as an extended target and results in more information about the target. However, extracting this information from the radar returns is challenging due to several complexities. These complexities include the single dimensional nature of the radar measurements, complexities associated with the scattering of electromagnetic waves, and complex environments in which radar systems are required to operate. There are several applications of HRR radar systems which extract target information with varying levels of success. A commonly used application is that of imaging referred to as synthetic aperture radar (SAR) and inverse SAR (ISAR) imaging. These techniques combine multiple single dimension measurements in order to obtain a single two dimensional image. These techniques rely on rotational motion between the target and the radar occurring during the collection of the single dimension measurements. In the case of ISAR, the radar is stationary while motion is induced by the target.

There are several difficulties associated with the unknown motion of the target when standard Doppler processing techniques are used to synthesise ISAR images. In this dissertation, a non-standard Dop-

pler approach, based on Bayesian inference techniques, was considered to address the difficulties. The target and observations were modelled with a non-linear state space model. Several different Bayesian techniques were implemented to infer the hidden states of the model, which coincide with the unknown characteristics of the target. A simulation platform was designed in order to analyse the performance of the implemented techniques. The implemented techniques were capable of successfully tracking a randomly generated target in a controlled environment. The influence of varying several parameters, related to the characteristics of the target and the implemented techniques, was explored. Finally, a comparison was made between standard Doppler processing and the Bayesian methods proposed.

OPSOMMING

'N MONTE CARLO BENADERING TOT OORHEERSENDE WEERKAATSING VOLGING VAN 'N ENKELE UITGEBREIDE TEIKEN IN HOË AFSTANDSRESOLUSIE RADAR

deur

Allan De Freitas

Studieleier(s):	Dr. J.P. de Villiers & Mr. W.A.J. Nel
Departement:	Elektriese, Elektroniese en Rekenaar-Ingenieurswese
Universiteit:	Universiteit van Pretoria
Graad:	Magister in Ingenieurswese (Elektroniese Ingenieurswese)
Sleutelwoorde:	Uitgebreide Teiken, volging, hoë afstandsresolusie radar, hoë afstandsresolusie profiel, partikel filtering, ISSR, partikel Markov ketting Monte Carlo, partikel marginale Metropolis-Hastings monsteringsmetode, statiese parameter estimasie

In hoë afstandsresolusie radar (HAR) stelsels, kan 'n radarpuls se weerkaatsing vanaf 'n enkele teiken in verskeie aaneenlopende afstandshekke val waarvan elkeen kan wissel in amplitude. 'n Teiken wat op hierdie manier voorgestel word, word 'n uitgebreide teiken genoem en verskaf meer inligting oor die teiken. As gevolg van verskeie komplikasies is dit egter nie so eenvoudig om hierdie inligting uit die weerkaatsing te onttrek nie. Hierdie komplikasies is as volg: die enkel-dimensionele aard van die radarmetings; kompleksiteite wat verband hou met die weerkaatsing van elektromagnetiese golwe; die komplekse omgewings waarin radar stelsels moet funksioneer. Daar is verskillend HAR-verwante algoritmes wat die teiken inligting kan onttrek, elk met verskillende vlakke van sukses. 'n Algemene benadering is die van beeldvorming waarna verwys word as sintetiese stralingsvlak radar (SSR) en inverse SSR (ISSR) beeldvorming. Hierdie tegnieke kombineer verskeie enkel-dimensionele metings om 'n enkele twee-dimensionele beeld te kry. Verder maak hierdie tegnieke staat op die beweging tussen die teiken en die radar tydens die versameling van die enkel-dimensionele metings. In die geval van ISSR, is die radar stilstaande terwyl die teiken die beweging veroorsaak.

Daar is verskeie probleme wat verband hou met die onbekende beweging van die teiken wanneer standaard Doppler verwerkingstegnieke gebruik word om ISSR beelde te vorm. In hierdie verhandeling, word die standaard Doppler benadering nie gevolg nie, maar ’n benadering gebaseer op Bayesiese afleidingstegnieke. Die teiken en waarnemings word gemodelleer deur ’n nie-lineêre toestandsruimte model. ’n Verskeidenheid Bayesiese tegnieke was geïmplementeer om die verborge toestande van die model af te lei. Hierdie verborge toestande verteenwoordig die onbekende eienskappe van die teiken. ’n Simulasie platform is ontwerp om die prestasie van die geïmplementeerde tegnieke te analiseer. Die geïmplementeerde tegnieke was daartoe in staat om suksesvol die willekeurige gegenereerde teiken in ’n beheerde omgewing te volg. Die invloed van die wisseling van verskeie parameters, wat verband hou met die eienskappe van die teiken en die geïmplementeerde tegnieke, is ondersoek. Laastens word ’n vergelyking getref tussen die standaard Doppler verwerking en die voorgestelde Bayesiese metodes.

ACKNOWLEDGEMENTS

I would like to extend my gratitude to the following people and organisations for the support they offered me while I endeavoured to complete my research:

- First and foremost, I would like to thank my Lord and Saviour for granting me the opportunity and talent to conduct this research.
- I would like to thank my study leader Dr. J.P. de Villiers. Without Dr. de Villiers' help and guidance this work would not have been possible.
- My parents, grandmother and siblings, who encouraged me through out this research project and also supported me financially.
- My wife, Trinette, and her family, for all their support and encouragement.
- I extend my thanks to all the numerous people who helped review and edit the dissertation.
- The Council for Scientific and Industrial Research (CSIR), King Abdulaziz City for Science and Technology (KACST), and the University of Pretoria for their financial support.

LIST OF ABBREVIATIONS

APF	Auxiliary Particle Filter
BPF	Bootstrap Particle Filter
DSA	Dominant Scatterer Algorithm
EKF	Extended Kalman Filter
EM	Electromagnetic
ESS	Effective Sample Size
FFT	Fast Fourier Transform
HF	High-Frequency
HRR	High Range-Resolution
ISAR	Inverse Synthetic Aperture Radar
KF	Kalman Filter
LFM	Linear Frequency Modulated
MCMC	Markov Chain Monte Carlo
MH	Metropolis-Hastings
MTT	Multi-Target Tracking
PF	Particle Filter
PMMH	Particle Marginal Metropolis-Hastings
PRF	Pulse Repetition Frequency
RCS	Radar Cross Section
RMSE	Root Mean Square Error
SAR	Synthetic Aperture Radar
SFW	Stepped Frequency Waveform
SIS	Sequential Importance Sampling
SMC	Sequential Monte Carlo
SNR	Signal-to-Noise Ratio
SUT	Scaled Unscented Transformation
UKF	Unscented Kalman Filter
UPF	Unscented Particle Filter

TABLE OF CONTENTS

CHAPTER 1

INTRODUCTION

1.1 BACKGROUND & CONTEXT

Radar systems are used in a wide range of applications including, but not limited to, weather monitoring [1], target detection [2], target classification [3], scene imaging [4], and target tracking [5]. Radar systems utilise electromagnetic waves to detect and infer different characteristics of a target located within a specific region. This is performed through a two step process which includes the illumination of a specific region with electromagnetic waves, followed by the reception of any electromagnetic scatter which is reflected from objects in the region towards the radar system. The target is considered to be a specific object of interest and differs according to the application. Reflections from other objects within the region are referred to as clutter. When an electromagnetic wave is incident upon the surface of a target, it is scattered in a complex manner. The scattered wave directed towards the radar system from a target originates primarily from multiple individual reflection points, referred to as dominant scatterers [6]. This was observed experimentally in [7] using an imaging and tracking radar system, where dominant scattering sources for multiple types of aircraft were consistently measured over a time period of up to 20 seconds with changes in range and aspect angles.

A large variety of radar configurations exist [8], this research focuses on processing returns obtained by monostatic pulsed radar systems capable of achieving a high range-resolution (HRR). HRR systems transmit high bandwidth waveforms to achieve the required range-resolution. Processing the raw returns, observed by the radar, results in a discrete complex HRR profile. A HRR profile is a projection of the observable scatterers located in a three dimensional space to a single dimension, referred to as the range dimension, located along the radar line of sight [9]. Similarly, a synthetic aperture radar (SAR) and inverse SAR (ISAR) image is a projection of the observable scatterers loc-

ated in a 3-D space to a 2-D image plane. A SAR/ISAR image can be generated from a sequence of HRR profiles that are obtained at different azimuth angles between the radar platform and the target [10]. This is achieved due to the effective rotational motion of the target and/or radar platform during the collection of HRR profiles. This research is associated with ISAR due to the assumption of a stationary radar sensor and a target subjected to unknown motion.

1.2 MOTIVATION

The motion of a target may vary depending on the type of target. Vehicles on land have restricted motion when compared to aircraft and maritime vessels. The motion of an unconstrained target located in a three dimensional space contains 6 degrees of freedom. This includes 3 degrees of freedom of rotational and translational motion respectively, as illustrated in Figure 1.1. In ISAR

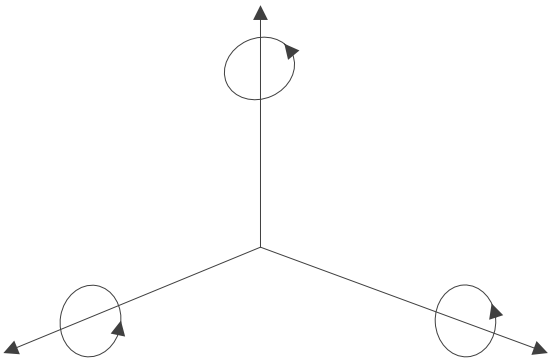

Figure 1.1: Illustration of the 6 degrees of freedom for the motion of an unconstrained target in a 3-D co-ordinate system.

processing, the target motion is ideally a constant rate of rotation about a fixed axis. In this case, and under the assumption that HRR profiles are collected over a period in which no migration of scatterers through resolution cells occurs, an undistorted ISAR image can be obtained by performing a fast Fourier transform (FFT) on each range bin. When the motion of the target also consists of translational motion components further preprocessing is required, prior to the FFT on each range bin, to remove the effects thereof. Translational motion compensation focuses on removing the component of motion directed along the line of sight of the radar which jointly affects all the scatterers, whilst retaining the rotational motion. It is either carried out as a single step, or firstly as coarse range alignment followed by fine phase correction [11]. Conventional motion compensation algorithms generally assume that the rotational motion of the target is constrained to a 2-D plane during the

interval in which the target is observed [12]. It has been found that many real world targets exhibit rotation in a 3-D plane, including aircraft undergoing fast manoeuvres [13] and ships at sea [14]. The presence of rotation in a 3-D plane may result in distorted ISAR images. It has also been found that ISAR images of targets subjected to a time-varying perturbed motion can lead to distortion in ISAR images [10].

The rotation induced by the target is essential in order to resolve the scatterers in the cross-range dimension, the direction perpendicular to the range dimension. However, the unknown complex motion of a target can result in severe distortion of ISAR images. Knowledge of the motion of the target would allow for the compensation of the distortive effects. Since ISAR is generally performed on uncooperative targets, a need to estimate the motion of a target prior to the generation of ISAR images is clearly evident.

1.3 OBJECTIVE

The primary objective of this research is to design an algorithm which is capable of tracking the locations of multiple dominant scatterers and motion parameters of an extended target that is observed by a monostatic pulsed HRR radar. It is assumed that the target is uncooperative and hence only the measurements obtained from the radar are available. Techniques based on Bayesian frameworks were explored due to the stochastic nature of the motion of the target and radar measurements.

In order to achieve this objective, the design and implementation of a simulation test platform was required. The simulation test platform includes the simulation of the target, the evolution of the target's location through time, and the simulation of a monostatic pulsed HRR radar system which obtains measurements from the target.

1.4 CONTRIBUTION

The contribution which this research makes to the field of radar is the novel application of several Monte Carlo techniques that extract information of an extended target from measurements taken by a monostatic pulsed HRR radar. The motivation for the research was based on the extraction of the motion parameters of the extended target to aid in the reduction of distortion in ISAR imagery, however, additionally inferring the locations of multiple dominant scatterers on the extended target may also aid in systems which perform automatic target recognition based on HRR profiles [3].

There are several approaches [15, 16, 17] which utilise the dominant scatterer assumption to infer scatterer locations and target motion parameters from monostatic pulsed HRR radar. This dissertation applies a novel approach, based on Bayesian inference techniques, to the problem.

1.5 OUTLINE OF DISSERTATION

The dissertation is separated into 6 chapters. Chapter 2 introduces the reader to the radar principles and processing which is used extensively in the dissertation. Chapter 3 introduces the reader to Bayesian non-linear tracking, with the focus on Monte Carlo methods which are capable of state estimation as well as joint state and static parameter estimation. Chapter 4 introduces the reader to the target model, radar simulator and state space modelling created specifically for the HRR radar application. In Chapter 5 the results obtained by applying several different techniques that are capable of inference based on the state space models defined in Chapter 4 are presented. In Chapter 6 conclusions are drawn based on the results obtained and recommendations for future research are highlighted.

1.6 PUBLICATIONS

1.6.1 Conference Proceedings

The following paper was presented at the international Information Fusion conference in Singapore 2012. The paper has been published in the peer reviewed proceedings of the conference.

1. A. De Freitas and J. De Villiers, "Multiple Scatterer Tracking in High Range-Resolution Radar." in *Information Fusion (FUSION), 2012 15th International Conference on*, July 2012, pp. 1683-1688.

1.6.2 Journal Publications

The following article was submitted to a peer-reviewed and ISI accredited journal.

1. A. De Freitas, J. De Villiers and W. Nel, "A Particle Filter Approach to Extended Target Tracking in High Range-Resolution Radar." *IEEE Signal Processing Letters*, submitted for publication.

CHAPTER 2

RADAR PRINCIPLES

2.1 INTRODUCTION

Historically, conventional radar systems have been used to infer knowledge of different aspects of a target of interest. This knowledge included the range, velocity and heading of the target relative to the radar system [18]. With advancements in radar technology, modern radar systems are capable of identifying, imaging, tracking and classifying targets while suppressing incident reflections which are not associated with the target. Much of the functionality associated with modern radar systems is made possible through HRR radar.

This chapter introduces important concepts related to HRR radar which are used by the HRR radar simulator and the observation extraction process which are both further elaborated on in Chapter 4.

2.2 SCATTERING MECHANISMS

HRR radar systems illuminate regions which may contain targets with electromagnetic (EM) energy. Once the EM energy is incident upon a target in the region, it is scattered in a complex manner. There are several different scattering mechanisms which may result in EM energy being redirected back towards the radar system. The dominant types of scattering mechanisms are dependent on the size of the target relative to the wavelength of the transmitted EM energy and generally fall under one of the following three regions [8]:

1. Rayleigh region dipole scattering.

2. Resonant region scattering.

3. High-frequency (HF) optics region scattering.

Typically HRR radar systems fall under the HF optics region scattering [7]. In this region the wavelength of the EM energy is assumed to be much smaller than the extent of the target. The four primary scattering mechanisms which occur in this region are:

1. Direct illumination specular scattering which is normal to surfaces.

2. Multiple specular scattering induced through the EM energy bouncing between structures on the target.

3. Diffractive scattering from the end regions of finite targets.

4. Travelling wave scattering along edges.

The specific dominant scattering mechanisms that generate scatter are dependent on the geometry and material composition of the target. The scatter of interest is that which is directed towards the radar, referred to as the backscatter direction. A traditional measure of a target's scattering behaviour in the backscatter direction is the radar cross section (RCS). The RCS is a measure of the reflective strength of a target [19]. Due to normalisation, the RCS is not dependent on the distance between a target and the radar system or the transmitter power level of the radar system. When the dominant scattering mechanisms are those in the HF optics region, the target may be modelled as a collection of scattering centres referred to as scatterers. The RCS of a target may fluctuate greatly due to the fact that the total coherent RCS of multiple scatterers is dependent on the phase of each scatterer. The total coherent RCS for N scatterers is represented mathematically as

$$\sigma_{total} = \left| \sum_{i=1}^{N} \sqrt{\sigma_i} e^{\frac{j4\pi R_i}{\lambda}} \right|^2, \tag{2.1}$$

where $\sqrt{\sigma_i}$ and R represents the scatterer amplitude and distance between the radar system and scatterer i respectively, and λ represents the wavelength of the transmitted EM wave. The RCS for a target may vary greatly depending on the complexity of the target and the aspect angle between the radar and the target. As such, an exact RCS pattern for an individual target is hard to determine and would also be of limited use due to the limited knowledge that a radar system has of an uncooperative target. Thus statistical models that use probability distributions to describe the variations in the RCS

have been described. Well known models include the Swerling target models [18].

2.3 RADAR FUNDAMENTALS

A monostatic pulsed radar system illuminates a region with a pulsed radar waveform. The time delay between when the pulsed waveform is transmitted and a reflection from a target in the region of illumination is sensed by the radar system, is directly related to the distance between the target and the radar system according to the following equation

$$t = \frac{2R}{c}, \tag{2.2}$$

where t represents the time delay, and c represents the speed of light ($c \approx 3\times10^8$ m/s).

2.3.1 Range Resolution

Range resolution describes the minimum distance, specifically in terms of the range dimension, with which a radar system is capable of resolving two sources of reflections [6]. In the context of HRR, the sources of reflections are the individual scatterers located on a single target. The range resolution is related to the bandwidth of the radar waveform through the following expression

$$\Delta R_{cell} \approx \frac{c}{2B}, \tag{2.3}$$

where ΔR_{cell} represents the extent of a range resolution cell and B represents the bandwidth of the radar waveform.

The complex returns of all the scatterers which are located within a single range resolution cell constructively or destructively interfere to result in a combined response, as illustrated by Equation 2.1 for the RCS. In general, the aim is to minimise the range resolution in order to obtain more information about the target.

2.3.2 Range Ambiguity

A pulsed radar system retransmits the radar waveform at a specific frequency referred to as the pulse repetition frequency (PRF). The PRF of the radar determines the maximum range to a target which can be measured by the radar system. Targets located further away which are still detected by the radar system result in an ambiguous measurement that will lead to the target being measured as closer

to the radar than in reality. The unambiguous target range is given by

$$R_u = \frac{c}{2 \cdot PRF}. \tag{2.4}$$

2.3.3 Doppler Frequency

The Doppler effect describes the phenomenon of the change in center frequency of a waveform that is incident upon a target which is undergoing motion relative to the radiation source of the waveform. The change in frequency is induced due to an increase or decrease in the wavelength of the waveform when the target is receding or closing respectively. The Doppler frequency is the difference in the centre frequency of a waveform that is transmitted, incident upon a target undergoing motion relative to the source of transmission and received. The Doppler frequency is represented mathematically as

$$f_d = \frac{2v_r}{c}, \tag{2.5}$$

where v_r represents the radial velocity of the target. In terms of HRR radar systems, the target typically contains velocity components that are not only directly towards or away from the radar system. For a more general velocity, the Doppler frequency is given by

$$f_d = \frac{2v}{c} \cos\theta_a, \tag{2.6}$$

where θ_a represents the angle between the radar line of sight and the velocity vector of the target.

2.4 HIGH RANGE-RESOLUTION PROFILES

A HRR profile is a projection of the complex returns from the observable scatterers on a target located in a 3-dimensional space to a 1-dimensional space. The 1-dimensional space is referred to as the range dimension and is located along the line of sight of the radar. Figure 2.1 illustrates an example of how the magnitude of a complex HRR profile is related to a target in range. The HRR profile is a discrete complex result. A range bin is the minimum range resolution cell that is resolved in the HRR profile. The amplitude of each range bin is dependent on the strength of the return from the scatterer located within the range bin. Constructive or destructive interference may occur when multiple scatterers are located in a single range bin as illustrated in Figure 2.2. In Figure 2.2 (a) a target consisting of four dominant scatterers is illustrated. The magnitude of the HRR profile for the case when the target

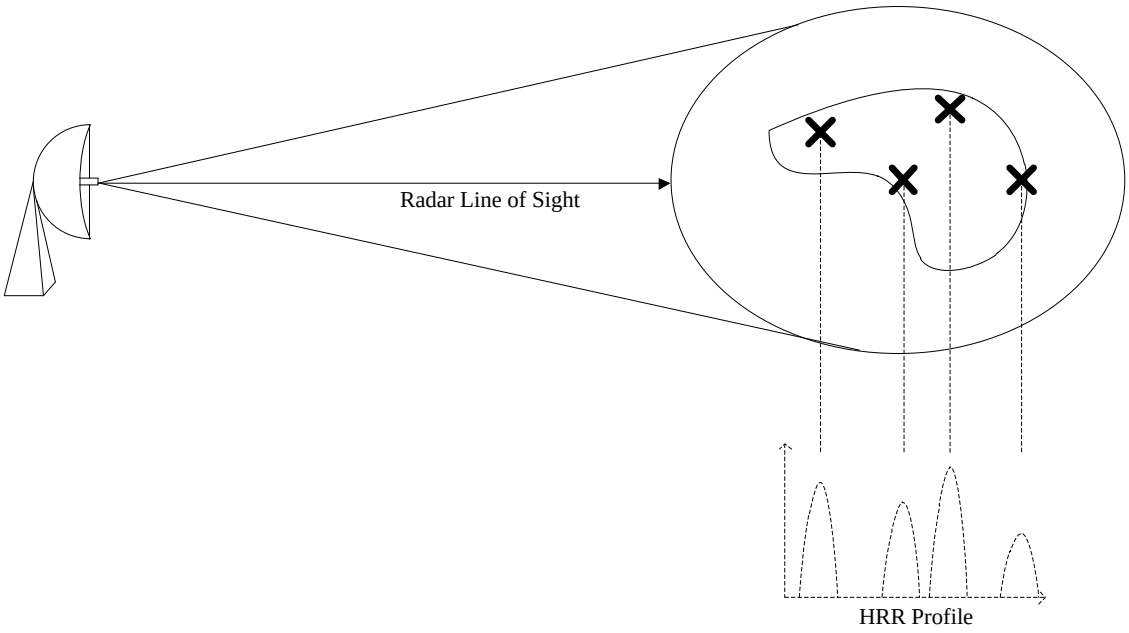

Figure 2.1: Illustration of the relation between a target and the magnitude of a complex HRR profile.

only consists of each dominant scatterer and when the target consists of all the dominant scatterers is overlayed in Figure 2.2 (b).

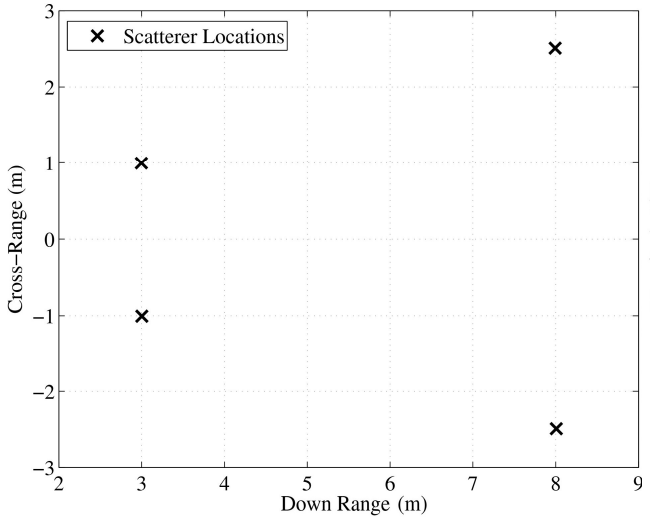

(a) A target consisting of 4 dominant scatterers. Zero of down range dimension shifted to 10000.

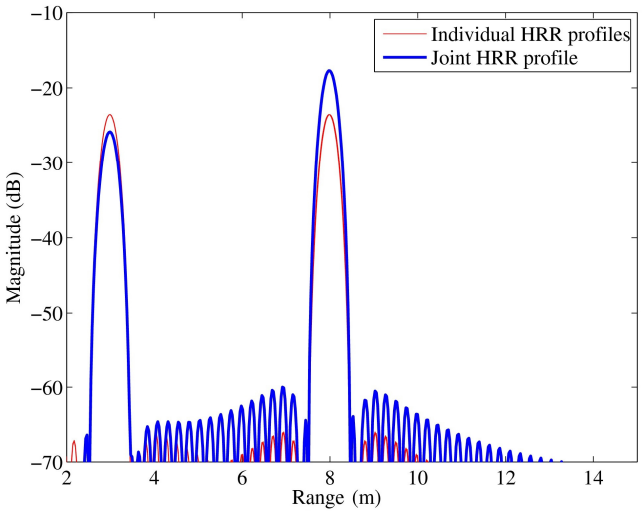

(b) The corresponding magnitude of HRR profile for the 4 dominant scatterer target. Zero of range dimension shifted to 10000.

Figure 2.2: Illustration of constructive and destructive interference in a HRR profile.

It is clear from Figure 2.2 (b) that the two dominant scatterers on the left and on the right result in destructive and constructive interference respectively. The effect of the interference on the magnitude of the complex return for a single range bin due to multiple scatterers is dependent on the type of scatterers located in the range bin. Three possible categories for the type of scatterers located in a range bin have been identified:

1. When a range bin contains a large number of small scatterers with no dominant scatterers.

2. When a range bin contains a number of small scatterers with a single dominant scatterer present.

3. When a range bin contains a number of small scatterers with multiple dominant scatterers present.

Statistical models for the fluctuations in each category have been explored [20]. It is impossible to determine the number or type of scatterers located in a range bin from the HRR profile. The error caused in the amplitude and phase of the complex return, due to the assumption that only a single scatterer is located in a range bin when there are actually multiple scatterers, is referred to as scintillation and glint noise respectively [18]. This noise is more predominant when dominant scatterers interfere and is reduced in HRR radar systems due to the relatively high range-resolution which allows for a higher degree of dominant scatterer isolation.

2.5 HIGH RANGE-RESOLUTION RADAR WAVEFORMS

Three groups of radar waveforms are utilised by HRR radar systems to obtain HRR profiles. These include,

1. fixed frequency waveforms,

2. pulse-compression waveforms, and

3. inter-pulse modulated waveforms.

The bandwidth of a standard rectangular pulse waveform is inversely proportional to the duration of the pulse. Increasing the bandwidth of the waveform results in a finer range resolution according to Equation 2.3. With a standard rectangular pulse waveform, a larger bandwidth can be obtained by decreasing the duration of the pulse. However, this approach is practically limited as a minimisation

in pulse duration requires analogue electronics capable of higher sampling rates and also requires the transmitter to output a higher peak output power in order to maintain a specific average power. These limitations lead to the development of pulse-compression and inter-pulse modulation.

Pulse-compression waveforms consist of techniques which do not require the minimisation of the pulse duration in order to obtain large increases in the bandwidth of the signal. This is done through linear or non-linear amplitude, frequency or phase modulation. One of the most commonly used pulse-compression waveforms is the linear frequency modulated (LFM) waveform. The waveform is produced by linearly increasing the frequency of an oscillator. The advantages of the LFM waveform includes the ability to easily generate the waveform through the application of either active or passive techniques, and the fact that the LFM pulse shape and signal-to-noise ratio (SNR) are relatively insensitive to changes in the frequency of the returned signal [21]. Changes in the frequency of the received signal occur when the target being measured by the radar system is subjected to motion, due to the Doppler effect. HRR profiles are typically obtained through either matched filtering or stretch processing when pulse compression waveforms are utilised [22].

Inter-pulse modulated waveforms are used in radar systems which are subjected to hardware limitations. Specifically related to limitations in the instantaneous bandwidth available for the demodulation of the received signal. A stepped frequency waveform (SFW) is a inter-pulse technique commonly used in HRR radar systems [6, 23]. The requirement for a high instantaneous bandwidth is overcome by SFWs, by transmitting n narrowband radar waveforms. Each narrowband radar waveform is transmitted at a different carrier frequency. The carrier frequency is stepped by a fixed frequency step. This is essentially sampling in the frequency domain. The received in-phase and quadrature samples are stored for each pulse. Spectral weighting is applied if necessary to reduce the magnitude of the sidelobes in the received signal at the expense of degrading the range resolution. Finally the inverse discrete Fourier transform is applied to the data to obtain the data in the time domain. The time domain representation is directly related to the range domain through Equation 2.2 resulting in a synthetic HRR profile. The equivalent bandwidth of a SFW is given by

$$B = n\Delta f, \tag{2.7}$$

where Δf is the inter-pulse frequency difference. The unambiguous range window for the SFW is limited to the unambiguous range for a single pulse,

$$R_{u,w} = \frac{c}{2\Delta f}. \tag{2.8}$$

The disadvantage of utilising SFWs is that the time period that it takes to collect measurements is n times longer when compared to an equivalent pulse-compressed waveform. This may be an obvious disadvantage for time constrictive applications, however, uncompensated motion of the target which occurs during the collection of the n profiles may distort the resulting synthetic HRR profile.

The SFW method of HRR profile synthesis was utilised by the radar simulator in Section 4.3. The main reason for the selection of this HRR profile synthesis technique was due to the availability of real world data obtained by a HRR radar system that utilises SFW. This supports future research aimed at applying the techniques developed in this dissertation on the real world data. The next chapter introduces the Bayesian techniques used to infer the motion parameters of a target and the location of the dominant scatterers on a target from a set of HRR profiles.

CHAPTER 3

TRACKING ALGORITHMS

3.1 INTRODUCTION

Object tracking is a challenging problem which appears in multiple fields. The application of this dissertation is related to the tracking of multiple dominant scatterers located on a single target being observed by a HRR radar system. However, regardless of the application, a general procedure for designing an object tracking algorithm exists. This chapter introduces the general procedure for object tracking algorithm design and highlights several filtering methods which were utilised in this research.

3.2 OBJECT TRACKING

The general procedure for designing an object tracking algorithm is summarised by the following steps [24]:

1. Object Representation - The first step required in an object tracking application is to clearly define how the object is represented. This representation is largely dependent on the mechanism used to observe the object. In conventional tracking radar, a target of interest is represented by a single point in space [25]. In HRR radar systems, it is possible to treat multiple dominant scatterers on a target of interest as points in space.

2. Feature Selection - It is required to first obtain features from the raw observations of the object. Depending on the application, it may be necessary to first perform feature extraction. If multiple features are present, features which contribute the most information about the object

representation may be chosen. A limited number of features where extracted and used in the dominant scatterer tracking application.

3. Object Detection - A method for the detection of the object from the raw observations is required. This method is utilised each time a new observation is available for processing which then allows for the extraction of the selected features that describe the object.

4. Tracking Algorithm Selection - Many different tracking algorithms exist. Statistical methods were considered due to the existence of noise in the observations and the possibility of perturbations in the motion of the target.

The application investigated by this research is considered to fall in the framework of a multi-target tracking (MTT) problem as a target consists of multiple individual dominant scatterers which are required to be tracked. Typical MTT applications are concerned with the tracking of multiple independent point targets [26]. However, in this application, the multiple point targets are fixed on a rigid body and cannot be considered independent. Targets which are represented in this manner are referred to as extended targets. There are two difficulties which are associated with the following statistical approaches to extended target tracking [27]:

1. Realistic models for the target dynamics and the measurement processes are often non-linear and perturbed by non-Gaussian noise.

2. The sensor typically yields unlabelled measurements of the point targets.

The first difficulty is the main focus of this research. The second difficulty is commonly referred to as the data association problem. Ideal data association was assumed as there are several classic techniques which have been applied to solving data association in the same statistical framework as used in this research, including multiple hypothesis tracking [28], joint probabilistic data association filter [29], nearest neighbour association [29], and probabilistic multiple hypothesis tracking [30].

3.3 STATE SPACE MODELLING

Tracking, in a statistical framework, consists of the estimation of the states of an object undergoing motion based on noisy measurements. Filtering is the estimation of the current state of a dynamic system given the past and current observations. Estimation of future states given the past and current

observations is referred to as prediction, and the estimation of states given past and future observations is referred to as smoothing. Tracking applications generally perform filtering at each time step [31]. A state space model may be either continuous time, continuous-discrete time or discrete time [32] and consists of models for the observations and dynamics of the states. A discrete state space model is represented by

$$\begin{aligned} \boldsymbol{x}_k &= a(\boldsymbol{x}_{k-1}, \boldsymbol{w}_k), \\ \boldsymbol{y}_k &= b(\boldsymbol{x}_k, \boldsymbol{v}_k), \end{aligned} \tag{3.1}$$

where $\boldsymbol{x}_k$ and $\boldsymbol{y}_k$ represent the states and observations at discrete time instant k respectively, $\boldsymbol{w}_k$ and $\boldsymbol{v}_k$ represent stochastic variables modelling the noise disturbances in the state dynamics and observations respectively, and $a(\cdot)$ and $b(\cdot)$ represent generation functions for the states and observations. A probabilistic equivalent to the equations presented in Equation 3.1 are given by

$$\begin{aligned} \boldsymbol{x}_k &\sim f(\boldsymbol{x}_k|\boldsymbol{x}_{k-1}), \\ \boldsymbol{y}_k &\sim g(\boldsymbol{y}_k|\boldsymbol{x}_k), \end{aligned} \tag{3.2}$$

where $f(\cdot)$ is referred to as the state transition density and $g(\cdot)$ is referred to as the observation density and are probability distribution functions. A general assumption for the state dynamics in tracking applications is that the state variables form a temporal Markov chain. It is also assumed that the observations are mutually independent and independent of the state at previous time steps [33]. This model is illustrated graphically in Figure 3.1.

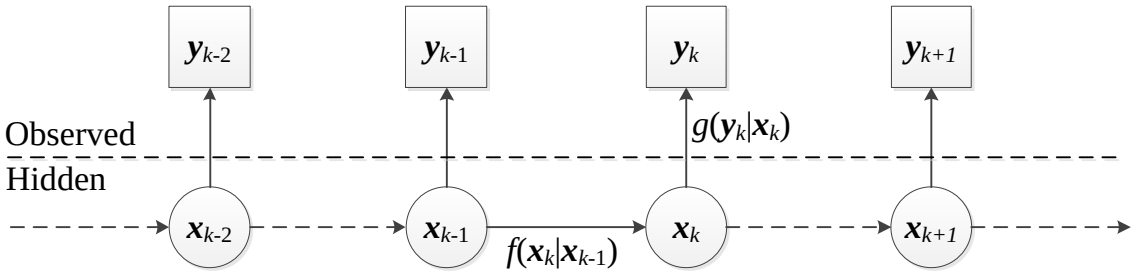

Figure 3.1: Illustration of a typical discrete time state space model.

3.4 BAYESIAN FILTERING

Bayesian inference relies on the posterior distribution, $p(\boldsymbol{x}_{1:T}|\boldsymbol{y}_{1:T})$, where $\boldsymbol{x}_{1:T} = \{\boldsymbol{x}_1, \boldsymbol{x}_2, \ldots, \boldsymbol{x}_T\}$, $\boldsymbol{y}_{1:T} = \{\boldsymbol{y}_1, \boldsymbol{y}_2, \ldots, \boldsymbol{y}_T\}$, and T represents the final discrete time step. The filtering distribution is the posterior distribution up to the current discrete time step, k, with the states of the previous time

steps marginalised out, $p(\boldsymbol{x}_k|\boldsymbol{y}_{1:k})$. The filtering distribution is the probability of interest in tracking applications utilising a Bayesian framework. The filtering distribution can be iteratively computed when the filtering distribution at the previous time step, $p(\boldsymbol{x}_{k-1}|\boldsymbol{y}_{1:k-1})$, is available. This is achieved through a two step process [34]. The first step is referred to as the prediction step and is based on the state transition density, via the Chapman-Kolmogorov equation

$$p(\boldsymbol{x}_k|\boldsymbol{y}_{1:k-1}) = \int f(\boldsymbol{x}_k|\boldsymbol{x}_{k-1})p(\boldsymbol{x}_{k-1}|\boldsymbol{y}_{1:k-1})d\boldsymbol{x}_{k-1}. \tag{3.3}$$

A new observation is then made at time instant k and incorporated through the second step referred to as the update step, via Bayes' rule

$$p(\boldsymbol{x}_k|\boldsymbol{y}_{1:k}) = \frac{g(\boldsymbol{y}_k|\boldsymbol{x}_k)p(\boldsymbol{x}_k|\boldsymbol{y}_{1:k-1})}{\int g(\boldsymbol{y}_k|\boldsymbol{x}_k)p(\boldsymbol{x}_k|\boldsymbol{y}_{1:k-1})d\boldsymbol{x}_k}. \tag{3.4}$$

The recursive relationship of Equations 3.3 and 3.4 form the optimal Bayesian solution. Utilising these equations for Bayesian filtering is generally not possible since an analytical solution only exists in certain circumstances. A commonly used analytical solution of the Bayesian recurrence relationship is the Kalman filter (KF) [31]. The KF assumes that the filtering distribution follows a Gaussian distribution. Additionally, the state space models are linear and perturbed by Gaussian noise. The performance of the KF is poor when applied to tracking applications which consist of state space models characterised by non-linearity and/or described by non-Gaussian statistics.

Several extensions of the KF have been developed to deal with non-linearities in state space models. Two popular extensions are the extended Kalman filter (EKF) [31] and unscented Kalman filter (UKF) [35]. The EKF has several different forms, in general the EKF linearises all non-linear models so that the traditional KF can be applied. The EKF is applied in a wide range of applications, however, a general consensus within the tracking and control community is that difficulties lie in the implementation and tuning of the EKF. The EKF performance is only reliable for systems that are almost linear on the time scale of the update intervals [36]. The UKF improves upon the EKF by representing the filtering distribution through a set of carefully chosen sample points which capture the mean and covariance of the Gaussian distribution. The sample points are then propagated through the true non-linear state space model. Ultimately neither the EKF, UKF or other Kalman based filters can approximate non-Gaussian filtering distributions.

The alternative to Kalman based filters explored throughout this research was that of sequential Monte Carlo (SMC) methods. The primary underlying SMC method of interest was the particle filter (PF) which is capable of dealing with state space models which are non-linear and/or contain non-Gaussian noise.

3.5 PARTICLE FILTERING

In Monte Carlo simulation, an approximation of the posterior distribution up to the current discrete time step, k, is represented by a weighted set of samples,

$$\hat{p}(\boldsymbol{x}_{0:k}|\boldsymbol{y}_{1:k}) = \frac{1}{N}\sum_{i}^{N}\delta_{\tilde{\boldsymbol{X}}_{0:k}^{i}}(\boldsymbol{x}_{0:k}), \tag{3.5}$$

where $\tilde{\boldsymbol{X}}_{0:k}^{i} \sim p(\boldsymbol{x}_{0:k}|\boldsymbol{y}_{1:k})$ and N represents the total number of samples[1] selected for the representation. In this context, the state at discrete time $k = 0$ is included in the representation of the posterior distribution as $p(\boldsymbol{x}_0)$ represents the prior distribution. It is commonly required to determine the properties of the posterior distribution, such as expectations of the form

$$\mathbb{E}[h_k(\boldsymbol{x}_{0:k})] = \int h_k(\boldsymbol{x}_{0:k})p(\boldsymbol{x}_{0:k}|\boldsymbol{y}_{1:k})d\boldsymbol{x}_{0:k}, \tag{3.6}$$

where $h_k(\boldsymbol{x}_{0:k})$ is a meaningful function for estimation. Using the Monte Carlo representation, the expectation can be approximated by

$$\overline{h}_k(\boldsymbol{x}_{0:k}) = \frac{1}{N}\sum_{i}^{N}h_k(\tilde{\boldsymbol{X}}_{0:k}^{i}), \tag{3.7}$$

and according to the law of large numbers $\overline{h}_k(\boldsymbol{x}_{0:k}) \xrightarrow[N\to\infty]{} \mathbb{E}[h_k(\boldsymbol{x}_{0:k})]$. However, owing to the lack of an analytical solution for the posterior distribution, it is impossible to obtain samples for the posterior distribution, $\tilde{\boldsymbol{X}}_{0:k}^{i}$. Importance sampling [34] is a method which overcomes this problem of sampling from the posterior distribution by obtaining samples from a known proposal distribution, $q(\boldsymbol{x}_{0:k}|\boldsymbol{y}_{1:k})$. Substituting the proposal distribution into Equation 3.6 results in

$$\mathbb{E}[h_k(\boldsymbol{x}_{0:k})] = \int h_k(\boldsymbol{x}_{0:k})\frac{p(\boldsymbol{x}_{0:k}|\boldsymbol{y}_{1:k})}{q(\boldsymbol{x}_{0:k}|\boldsymbol{y}_{1:k})}q(\boldsymbol{x}_{0:k}|\boldsymbol{y}_{1:k})d\boldsymbol{x}_{0:k}. \tag{3.8}$$

This expression can be further expanded by applying Bayes' rule to the posterior distribution

$$\mathbb{E}[h_k(\boldsymbol{x}_{0:k})] = \int h_k(\boldsymbol{x}_{0:k})\frac{g(\boldsymbol{y}_{1:k}|\boldsymbol{x}_{0:k})f(\boldsymbol{x}_{0:k})}{p(\boldsymbol{y}_{1:k})q(\boldsymbol{x}_{0:k}|\boldsymbol{y}_{1:k})}q(\boldsymbol{x}_{0:k}|\boldsymbol{y}_{1:k})d\boldsymbol{x}_{0:k}. \tag{3.9}$$

The importance weights are defined as

$$w_k(\boldsymbol{x}_{0:k}) = \frac{g(\boldsymbol{y}_{1:k}|\boldsymbol{x}_{0:k})f(\boldsymbol{x}_{0:k})}{q(\boldsymbol{x}_{0:k}|\boldsymbol{y}_{1:k})}. \tag{3.10}$$

Substituting the importance weights into the expression in Equation 3.9 results in

$$\mathbb{E}[h_k(\boldsymbol{x}_{0:k})] = \int h_k(\boldsymbol{x}_{0:k})\frac{w_k(\boldsymbol{x}_{0:k})}{p(\boldsymbol{y}_{1:k})}q(\boldsymbol{x}_{0:k}|\boldsymbol{y}_{1:k})d\boldsymbol{x}_{0:k}. \tag{3.11}$$

[1] Each sample is also commonly referred to as a particle as the name of the SMC technique suggests.

The density in the denominator, $p(\boldsymbol{y}_{1:k})$, is an unknown normalising constant that can be removed from the integration,

$$\mathbb{E}[h_k(\boldsymbol{x}_{0:k})] = \frac{\int h_k(\boldsymbol{x}_{0:k}) w_k(\boldsymbol{x}_{0:k}) q(\boldsymbol{x}_{0:k}|\boldsymbol{y}_{1:k}) d\boldsymbol{x}_{0:k}}{p(\boldsymbol{y}_{1:k})}. \tag{3.12}$$

In order to simplify this expression further, it is firstly required to expand the unknown normalising constant in the denominator,

$$\mathbb{E}[h_k(\boldsymbol{x}_{0:k})] = \frac{\int h_k(\boldsymbol{x}_{0:k}) w_k(\boldsymbol{x}_{0:k}) q(\boldsymbol{x}_{0:k}|\boldsymbol{y}_{1:k}) d\boldsymbol{x}_{0:k}}{\int g(\boldsymbol{y}_{1:k}|\boldsymbol{x}_{0:k}) f(\boldsymbol{x}_{0:k}) d\boldsymbol{x}_{0:k}}. \tag{3.13}$$

Introducing the proposal distribution in the denominator allows for the term in the denominator to be simplified in terms of the importance weights in Equation 3.10,

$$\begin{aligned}\mathbb{E}[h_k(\boldsymbol{x}_{0:k})] &= \frac{\int h_k(\boldsymbol{x}_{0:k}) w_k(\boldsymbol{x}_{0:k}) q(\boldsymbol{x}_{0:k}|\boldsymbol{y}_{1:k}) d\boldsymbol{x}_{0:k}}{\int g(\boldsymbol{y}_{1:k}|\boldsymbol{x}_{0:k}) f(\boldsymbol{x}_{0:k}) \frac{q(\boldsymbol{x}_{0:k}|\boldsymbol{y}_{1:k})}{q(\boldsymbol{x}_{0:k}|\boldsymbol{y}_{1:k})} d\boldsymbol{x}_{0:k}} \\ &= \frac{\int h_k(\boldsymbol{x}_{0:k}) w_k(\boldsymbol{x}_{0:k}) q(\boldsymbol{x}_{0:k}|\boldsymbol{y}_{1:k}) d\boldsymbol{x}_{0:k}}{\int w_k(\boldsymbol{x}_{0:k}) q(\boldsymbol{x}_{0:k}|\boldsymbol{y}_{1:k}) d\boldsymbol{x}_{0:k}}.\end{aligned} \tag{3.14}$$

Similarly to Equation 3.7, the Monte Carlo approximation for the expression in Equation 3.14 is given by

$$\overline{h}_k(\boldsymbol{x}_{0:k}) = \frac{\frac{1}{N}\sum_i^N h_k(\boldsymbol{X}_{0:k}{}^i) w_k(\boldsymbol{X}_{0:k}{}^i)}{\frac{1}{N}\sum_i^N w_k(\boldsymbol{X}_{0:k}{}^i)}, \tag{3.15}$$

where $\boldsymbol{X}_{0:k}^i \sim q(\boldsymbol{x}_{0:k}|\boldsymbol{y}_{1:k})$. The normalised importance weights are represented by

$$\tilde{w}_k^i = \frac{w_k^i}{\sum_j^N w_k^j}. \tag{3.16}$$

The Monte Carlo approximation is then simplified in terms of the normalised importance weights

$$\overline{h}_k(\boldsymbol{x}_{0:k}) = \sum_i^N h_k(\boldsymbol{X}_{0:k}{}^i) \tilde{w}_k^i. \tag{3.17}$$

The Monte Carlo approximation for the posterior distribution is thus represented by

$$\hat{p}(\boldsymbol{x}_{0:k}|\boldsymbol{y}_{1:k}) = \sum_i^N \tilde{w}_k^i \delta_{\boldsymbol{X}_{0:k}^i}(\boldsymbol{x}_{0:k}). \tag{3.18}$$

However, this is a non-sequential method of obtaining an approximation for the posterior distribution. In order to obtain a sequential approximation, it is required to factor the proposal distribution

$$q(\boldsymbol{x}_{0:k}|\boldsymbol{y}_{1:k}) = q(\boldsymbol{x}_{0:k-1}|\boldsymbol{y}_{1:k-1}) q(\boldsymbol{x}_k|\boldsymbol{x}_{0:k-1}, \boldsymbol{y}_{1:k}). \tag{3.19}$$

Substituting the new form of the proposal distribution into Equation 3.10 and utilising the assumptions that the observations are mutually independent and the states form a temporal Markov chain, leads

to a sequential update for the importance weights. This is illustrated by firstly substituting the new proposal distribution into Equation 3.10,

$$w_k(\boldsymbol{x}_{0:k}) = \frac{g(\boldsymbol{y}_{1:k}|\boldsymbol{x}_{0:k})f(\boldsymbol{x}_{0:k})}{q(\boldsymbol{x}_{0:k-1}|\boldsymbol{y}_{1:k-1})q(\boldsymbol{x}_k|\boldsymbol{x}_{0:k-1},\boldsymbol{y}_{1:k})}. \tag{3.20}$$

Multiplying this expression with the importance weights from the previous time step in both the numerator and denominator results in,

$$w_k(\boldsymbol{x}_{0:k}) = \frac{w_{k-1}(\boldsymbol{x}_{0:k-1})}{w_{k-1}(\boldsymbol{x}_{0:k-1})} \frac{g(\boldsymbol{y}_{1:k}|\boldsymbol{x}_{0:k})f(\boldsymbol{x}_{0:k})}{q(\boldsymbol{x}_{0:k-1}|\boldsymbol{y}_{1:k-1})q(\boldsymbol{x}_k|\boldsymbol{x}_{0:k-1},\boldsymbol{y}_{1:k})}. \tag{3.21}$$

Expanding the importance weights from the previous time step in the denominator according to Equation 3.10 results in,

$$w_k(\boldsymbol{x}_{0:k}) = \frac{w_{k-1}(\boldsymbol{x}_{0:k-1})q(\boldsymbol{x}_{0:k-1}|\boldsymbol{y}_{1:k-1})}{g(\boldsymbol{y}_{1:k-1}|\boldsymbol{x}_{0:k-1})f(\boldsymbol{x}_{0:k-1})} \frac{g(\boldsymbol{y}_{1:k}|\boldsymbol{x}_{0:k})f(\boldsymbol{x}_{0:k})}{q(\boldsymbol{x}_{0:k-1}|\boldsymbol{y}_{1:k-1})q(\boldsymbol{x}_k|\boldsymbol{x}_{0:k-1},\boldsymbol{y}_{1:k})}. \tag{3.22}$$

Finally, simplifying this expression results in,

$$w_k = w_{k-1} \frac{g(\boldsymbol{y}_k|\boldsymbol{x}_k)f(\boldsymbol{x}_k|\boldsymbol{x}_{k-1})}{q(\boldsymbol{x}_k|\boldsymbol{x}_{0:k-1},\boldsymbol{y}_{1:k})}, \tag{3.23}$$

where the dependence on $\boldsymbol{x}_{0:k}$ for the importance weights was dropped for notational convenience. The sequential importance sampling (SIS) PF makes use of this relationship to iteratively update the approximation for the filtering distribution. This procedure is summarised in Algorithm 3.1.

Algorithm 3.1 Sequential Importance Sampling

Initialisation: $k = 0$

for i = 1,...,N **do**

Sample $\boldsymbol{X}_0^i \sim q_0(\boldsymbol{x}_0)$

end for

for k = 1,...,T **do**

for i = 1,...,N **do**

Sample $\boldsymbol{X}_k^i \sim q_k(\boldsymbol{x}_k|\boldsymbol{X}_{k-1}^i,\boldsymbol{y}_k)$

Evaluate the importance weights according to Equation 3.23.

end for

for i = 1,...,N **do**

Normalise the importance weights according to Equation 3.16.

end for

end for

* Where T represents the final time interval and $q_0(\boldsymbol{x}_0)$ represents the prior proposal distribution.

Although theoretically sound, the SIS algorithm is prone to weight degeneracy. Weight degeneracy occurs since the variance of the importance weights increases over time [37]. Essentially, a single particle will tend to have a normalised weight of 1, while the other particles weights tend towards zero, resulting in a poor representation of the posterior distribution. To partially overcome weight degeneracy, the introduction of a resampling step after the evaluation of the importance weights was proposed [38, 39]. Through resampling, particles which contain higher weights are duplicated while particles with lower weights are eliminated greatly alleviating the weight degeneracy problem. However, resampling may cause sample impoverishment, which is when particles with high weights are favoured to a large degree and can ultimately result in the entire set of particles being duplicates of a single particle. In order to prevent sample impoverishment, it has been proposed [34] to only perform resampling when weight degeneracy is severe. There are several measures of weight degeneracy that are utilised to determine when resampling should be performed. A commonly used measure is the effective sample size (ESS) [40],

$$\widehat{N}_{eff} = \frac{1}{\sum_i^N (\tilde{w}_k^i)^2}. \tag{3.24}$$

A value of 1 would indicate that all the probability mass is assigned to a single particle, indicating severe degeneracy, and conversely, the effective sample size approaches N when the weights tend to be uniformly spread among the particles. The generic PF is described by Algorithm 3.2.

The resultant of both the SIS PF and generic PF at each time step k is an approximation of the filtering distribution in the form

$$\hat{p}(\boldsymbol{x}_k|\boldsymbol{y}_{1:k}) = \sum_i^N \tilde{w}_k^i \delta_{\boldsymbol{X}_k^i}(\boldsymbol{x}_k). \tag{3.25}$$

There are several different resampling strategies currently applied in particle filters. The most common techniques are [41]:

1. multinomial resampling,
2. stratified resampling,
3. systematic resampling, and
4. residual resampling.

Algorithm 3.2 Generic Particle Filter

Initialisation: $k = 0$

for $i = 1,...,N$ **do**

Sample $\boldsymbol{X}_0^i \sim q_0(\boldsymbol{x}_0)$

end for

for $k = 1,...,T$ **do**

for $i = 1,...,N$ **do**

Sample $\boldsymbol{X}_k^i \sim q_k(\boldsymbol{x}_k|\boldsymbol{X}_{k-1}^i, \boldsymbol{y}_k)$

Evaluate the importance weights according to Equation 3.23.

end for

Normalise the importance weights according to Equation 3.16.

Calculate the severity of weight degeneracy, using a measure such as in Equation 3.24.

if Weight degeneracy detected **then**

Resample $\boldsymbol{X}_k^i$

for $i = 1,...,N$ **do**

Set $\tilde{w}_k^i = w_k^i = \frac{1}{N}$

end for

end if

end for

In multinomial resampling, a new set of samples are obtained through resampling and replacement based on the normalised importance weights. All the resampling strategies can be performed in $O(N)$ operations. Theoretically it has been shown that systematic resampling results in superior performance [41]. The choice of resampling strategy generally has a small effect on the performance of the PF [41, 42].

The success of an implementation of a PF is dependent on the validity of two assumptions. The first assumption is that the discrete Dirac point-mass approximation is a sufficient representation of the filtering distribution. This relates to the number of particles used to represent the filtering distribution, N. This value differs and is dependent on several factors including the application, the dimensionality of the state space, and the design of the PF, specifically the filter structure and initialisation [43]. Initialisation of the filter is a crucial step and is based on the prior knowledge of the states.

The second assumption is that it is possible to obtain samples from the filtering distribution by sampling from the proposal distribution and applying importance sampling corrections. This assumption is related to the choice of the proposal distribution. The choice of proposal distribution is one of the most important design issues in importance sampling algorithms. Theoretically, there is an infinite number of possible choices for the proposal distribution, as the only criteria for the proposal distribution is that its support must include that of the filtering distribution [44]. However, the optimal proposal distribution is the distribution which minimises the variance of the importance weights [45],

$$q_k(\boldsymbol{x}_k|\boldsymbol{X}_{k-1}^i,\boldsymbol{y}_k) = p(\boldsymbol{x}_k|\boldsymbol{X}_{k-1}^i,\boldsymbol{y}_k). \tag{3.26}$$

Substituting this proposal distribution into Equation 3.23 results in the following iterative importance weight update

$$w_k^i \propto w_{k-1}^i p(\boldsymbol{y}_k|\boldsymbol{X}_{k-1}^i) = w_{k-1}^i \int g(\boldsymbol{y}_k|\boldsymbol{x}_k) f(\boldsymbol{x}_k|\boldsymbol{X}_{k-1}^i) d\boldsymbol{x}_k. \tag{3.27}$$

However, sampling from this proposal distribution and solving the integral in Equation 3.27 is not possible with the exception of very few state space models. Alternatives to implementing the optimal proposal distribution includes using sub-optimal proposal distributions and using approximations of the optimal proposal distribution.

3.5.1 Bootstrap Particle Filter

In the seminal paper by Gordon et al. [39] it was proposed that the state transition density be used as the proposal distribution in the generic PF structure

$$q_k(\boldsymbol{x}_k|\boldsymbol{X}_{k-1}^i,\boldsymbol{y}_k) = f(\boldsymbol{x}_k|\boldsymbol{X}_{k-1}^i). \tag{3.28}$$

Subsequently, the importance weight update equation simplifies to

$$w_k^i = w_{k-1}^i g(\boldsymbol{y}_k|\boldsymbol{X}_k^i). \tag{3.29}$$

This specific PF structure is referred to as the bootstrap PF (BPF). The BPF has been widely used in several different fields such as in computer vision, where it is referred to as the condensation algorithm [46]. This selection of proposal distribution also has the advantage of reducing the computational complexity required for the calculation of the importance weights. However, unlike the optimal proposal distribution, this choice of proposal distribution fails to take the current observation into account when propagating the particles through the state space. This may lead to PF degeneracy, especially in applications where the likelihood density is relatively peaked in comparison to

the state transition density. Blindly propagating the particles through the state space in such an application could result in the particles being distributed into areas of low probability of the filtering distribution.

3.5.2 Auxiliary Particle Filter

There have been several different approaches that propose improvements on the BPF. One of the most notable approaches is referred to as the Auxiliary PF (APF), first proposed in [47]. In the APF, it is proposed that samples from the optimal importance distribution may be obtained through the introduction of an auxiliary variable. The original APF was improved into the algorithm commonly applied today [48]. In the BPF, the general structure of the algorithm is to first propagate the particles through the state transition density at each time step, followed by the weighting and possibly resampling of the particles. In contrast, the APF initially performs resampling of the particles based on the latest observation prior to the propagation of the particles through the state space. The APF is described by Algorithm 3.3.

It was suggested in [47] that the following simplifications be made

$$\begin{aligned} g(\boldsymbol{y}_k|\boldsymbol{X}_{k-1}^i) &= g(\boldsymbol{y}_k|\mu_k^i), \\ q_k(\boldsymbol{x}_k|\boldsymbol{X}_{k-1}^i,\boldsymbol{y}_k) &= f(\boldsymbol{x}_k|\boldsymbol{X}_{k-1}^i), \end{aligned} \tag{3.30}$$

where μ_k^i is a point value of the state, typically the mean or mode of $f(\boldsymbol{x}_k|\boldsymbol{X}_{k-1}^i)$. However, even though the APF takes the latest observation into account, it has been shown [49] that utilising the APF does not guarantee improved performance over the BPF.

Algorithm 3.3 Auxiliary Particle Filter

Initialisation: $k = 0$

for $i = 1,...,N$ **do**

Sample $\boldsymbol{X}_0^i \sim q_0(\boldsymbol{x}_0)$

end for

for $k = 1,...,T$ **do**

for $i = 1,...,N$ **do**

Evaluate the temporary weights $v_{k-1}^i = w_{k-1}^i g(\boldsymbol{y}_k|\boldsymbol{X}_{k-1}^i)$.

end for

Select N particle indices $j_i \in \{1,...,N\}$ according to the temporary weights.

for $i = 1,...,N$ **do**

Set $\boldsymbol{X}_{k-1}^i = \boldsymbol{X}_{k-1}^{j_i}$ and update the first stage weights $u_{k-1}^i = \frac{w_{k-1}^{j_i}}{v_{k-1}^{j_i}}$.

end for

for $i = 1,...,N$ **do**

Sample $\boldsymbol{X}_k^i \sim q_k(\boldsymbol{x}_k|\boldsymbol{X}_{k-1}^i, \boldsymbol{y}_k)$

Evaluate the importance weights $w_k^i = u_{k-1}^i \frac{g(\boldsymbol{y}_k|\boldsymbol{X}_k^i) f(\boldsymbol{X}_k^i|\boldsymbol{X}_{k-1}^i)}{q_k(\boldsymbol{X}_k^i|\boldsymbol{X}_{k-1}^i, \boldsymbol{y}_k)}$.

end for

Normalise the importance weights according to Equation 3.16.

end for

3.5.3 Unscented Particle Filter

There have also been several approaches which are based on the generic PF and approximate the optimal proposal distribution. One of the most notable approaches is referred to as the unscented PF (UPF) [42]. The UPF approximates the optimal proposal distribution with a Gaussian distribution. The UPF achieves this approximation through the implementation of the UKF. The UKF is based upon the scaled unscented transformation (SUT), which is essentially a method for determining the statistics of a random variable which undergoes a non-linear transformation.

Given a random variable $\boldsymbol{x}$ of dimension n_x that follows a Gaussian distribution with mean $\bar{\boldsymbol{x}}$ and covariance $\boldsymbol{P}_x$. The random variable is subjected to a nonlinear transformation resulting in a new random variable

$$\boldsymbol{y} = g(\boldsymbol{x}). \tag{3.31}$$

The aim of the SUT is to determine the first two moments of the distribution of $\boldsymbol{y}$. Initially a set of $2n_x+1$ weighted samples, $\boldsymbol{S}=\{\boldsymbol{W},\boldsymbol{X}\}$ referred to as sigma points, are deterministically selected. The sigma points capture the statistics of the distribution of $\boldsymbol{x}$. The sigma points are determined according to the following set of equations [50]

$$\begin{aligned}
X_0 &= \bar{\boldsymbol{x}} \\
X_i &= \bar{\boldsymbol{x}} + \left(\sqrt{(n_x+\lambda)\boldsymbol{P}_x}\right)_i \quad i=1,...,n_x \\
X_i &= \bar{\boldsymbol{x}} - \left(\sqrt{(n_x+\lambda)\boldsymbol{P}_x}\right)_i \quad i=n_x,...,2n_x \\
W_0^{(m)} &= \frac{\lambda}{(n_x+\lambda)} \\
W_0^{(c)} &= \frac{\lambda}{(n_x+\lambda)+(1-\alpha^2+\beta)} \\
W_i^{(m)} &= W_i^{(c)} = \frac{1}{2(n_x+\lambda)} \quad i=1,...,2n_x,
\end{aligned} \tag{3.32}$$

where $\lambda=\alpha^2(n_x+\kappa)-n_x$, and α, β and κ are scaling parameters. The indices (m) and (c) represent the weights for the mean and covariance. Each sigma point is then propagated through the non-linear transformation,

$$Y_i = g(X_i) \quad i=0,...,2n_x. \tag{3.33}$$

The first two moments of the transformed random variable, $\boldsymbol{y}$, can then be approximated by

$$\begin{aligned}
\bar{\boldsymbol{y}} &= \sum_{i=0}^{2n_x} W_i^{(m)} Y_i \\
\boldsymbol{P}_y &= \sum_{i=0}^{2n_x} W_i^{(c)} [Y_i-\bar{\boldsymbol{y}}][Y_i-\bar{\boldsymbol{y}}]^T.
\end{aligned} \tag{3.34}$$

The UKF utilises the SUT to perform recursive minimum mean-square-error estimation [36]. The random variable is redefined as the concatenation of the state variables and associated noise variables, $\boldsymbol{x}_k^a=[\boldsymbol{x}_k^T\,\boldsymbol{w}_k^T\,\boldsymbol{v}_k^T]^T$, described by Equation 3.1. The algorithm for the UKF is presented in Algorithm 3.4.

Algorithm 3.4 Unscented Kalman Filter

Initialisation: $k = 0$

$\bar{\boldsymbol{x}} = E[\boldsymbol{x}]$

$\boldsymbol{P}_0 = E\left[(\boldsymbol{x} - \bar{\boldsymbol{x}}) - (\boldsymbol{x} - \bar{\boldsymbol{x}})^T\right]$

$\bar{\boldsymbol{x}}_0^a = \left[\bar{\boldsymbol{x}}^T \boldsymbol{0}\ \boldsymbol{0}\right]^T$

$$\boldsymbol{P}_0^a = \begin{bmatrix} \boldsymbol{P}_0 & \boldsymbol{0} & \boldsymbol{0} \\ \boldsymbol{0} & \boldsymbol{Q} & \boldsymbol{0} \\ \boldsymbol{0} & \boldsymbol{0} & \boldsymbol{R} \end{bmatrix}$$

for $k = 1,\ldots,\infty$ **do**

Calculate sigma points, $\boldsymbol{S}_{k-1}^a$, according to Equation 3.32 based on $\bar{\boldsymbol{x}}_{k-1}^a$ and $\boldsymbol{P}_{k-1}^a$.

Perform time updates:

$\boldsymbol{X}_{k|k-1}^x = a\left(\boldsymbol{X}_{k-1}^x, \boldsymbol{X}_{k-1}^w\right)$

$\bar{\boldsymbol{x}}_{k|k-1} = \sum_{i=0}^{2n_a} W_i^{(m)} X_{i,k|k-1}^x$

$\boldsymbol{P}_{k|k-1} = \sum_{i=0}^{2n_a} W_i^{(c)} [X_{i,k|k-1}^x - \bar{\boldsymbol{x}}_{k|k-1}][X_{i,k|k-1}^x - \bar{\boldsymbol{x}}_{k|k-1}]^T$

$\boldsymbol{Y}_{k|k-1} = b\left(\boldsymbol{X}_{k|k-1}^x, \boldsymbol{X}_{k-1}^v\right)$

$\bar{\boldsymbol{y}}_{k|k-1} = \sum_{i=0}^{2n_a} W_i^{(m)} Y_{i,k|k-1}$

Perform measurement updates:

$\boldsymbol{P}_{\tilde{\boldsymbol{y}}_k \tilde{\boldsymbol{y}}_k} = \sum_{i=0}^{2n_a} W_i^{(c)} [Y_{i,k|k-1} - \bar{\boldsymbol{y}}_{k|k-1}][Y_{i,k|k-1} - \bar{\boldsymbol{y}}_{k|k-1}]^T$

$\boldsymbol{P}_{\tilde{\boldsymbol{x}}_k \tilde{\boldsymbol{y}}_k} = \sum_{i=0}^{2n_a} W_i^{(c)} [X_{i,k|k-1}^x - \bar{\boldsymbol{x}}_{k|k-1}][Y_{i,k|k-1} - \bar{\boldsymbol{y}}_{k|k-1}]^T$

$\boldsymbol{K}_k = \boldsymbol{P}_{\tilde{\boldsymbol{x}}_k \tilde{\boldsymbol{y}}_k} \boldsymbol{P}_{\tilde{\boldsymbol{y}}_k \tilde{\boldsymbol{y}}_k}^{-1}$

$\bar{\boldsymbol{x}}_k = \bar{\boldsymbol{x}}_{k|k-1} + \boldsymbol{K}_k(\boldsymbol{y}_k - \bar{\boldsymbol{y}}_{k|k-1})$

$\boldsymbol{P}_k = \boldsymbol{P}_{k|k-1} - \boldsymbol{K}_k \boldsymbol{P}_{\tilde{\boldsymbol{y}}_k \tilde{\boldsymbol{y}}_k} \boldsymbol{K}_k^T$

end for

*Where $\boldsymbol{X}^a = \left[(\boldsymbol{X}^x)^T (\boldsymbol{X}^w)^T (\boldsymbol{X}^v)^T\right]^T$, $n_a = n_x + n_w + n_v$, and $\boldsymbol{Q}$ and $\boldsymbol{R}$ are the process and measurement noise covariances respectively.

The UPF follows Algorithm 3.2 with the UKF described by Algorithm 3.4 calculated at each time step for each particle resulting in a sample from an approximation of the optimal proposal distribution.

3.6 STATIC PARAMETER ESTIMATION

The PF model, based upon the state space representation of Equation 3.2 assumed that all the static parameters associated with the state space model were known. Practically, there may be several static parameters which are unknown which would result in Equation 3.2 being more accurately represented by

$$\begin{aligned} \boldsymbol{x}_k &\sim f(\boldsymbol{x}_k|\boldsymbol{x}_{k-1},\boldsymbol{\theta}), \\ \boldsymbol{y}_k &\sim g(\boldsymbol{y}_k|\boldsymbol{x}_k,\boldsymbol{\theta}), \end{aligned} \tag{3.35}$$

where $\boldsymbol{\theta}$ represents a vector consisting of the static parameters associated with the model. There are two different sets of approaches which have been applied in attempts to solve the problem of static parameter estimation in systems which perform particle filtering. The first set of approaches are based upon frequentist parameter estimation. These approaches are concerned with maximum likelihood static parameter estimation in state space models [51, 52]. The second set of approaches are based upon Bayesian parameter estimation. There is a wide variety of attempts which follow the Bayesian approach, based on the state space representation in Equation 3.35. The filtering distribution of interest is represented by

$$p(\boldsymbol{x}_k,\boldsymbol{\theta}|\boldsymbol{y}_{1:k}). \tag{3.36}$$

Earlier methods proposed treating the static parameters as states through the augmentation of the state vector [53]. The static parameters are initialised according to a prior distribution but do not propagate through the state space owing to the static nature of the parameters. However, this may lead to severe degeneration since the state space is only explored upon initialisation and not at each time step. This was extended by exploring the state space in the dimensions of the static parameters with an artificial noise whose variance tends towards zero as N approaches infinity [53, 54].

In [55] it was proposed that the posterior distribution can be decomposed as

$$p(\boldsymbol{x}_{1:k},\boldsymbol{\theta}|\boldsymbol{y}_{1:k}) = Cp(\boldsymbol{x}_{1:k-1}|\boldsymbol{y}_{1:k-1})p(\boldsymbol{\theta}|\boldsymbol{T}_{k-1})p(\boldsymbol{x}_k|\boldsymbol{x}_{k-1},\boldsymbol{\theta})p(\boldsymbol{y}_k|\boldsymbol{x}_k,\theta), \tag{3.37}$$

where C is a constant that is not dependent on the state or static parameters, and $\boldsymbol{T}_k(\boldsymbol{x}_{1:k},\boldsymbol{y}_{1:k})$ represents a set of low dimensional sufficient statistics. The sufficient statistics can commonly be written in a recursive form based on the past sufficient statistics, the states, and the observations at the current time period, $\boldsymbol{T}_k(\boldsymbol{x}_{1:k},\boldsymbol{y}_{1:k}) = \boldsymbol{T}_k(\boldsymbol{x}_k,\boldsymbol{y}_k,\boldsymbol{T}_{k-1})$. Each particle is then redefined to include the sufficient statistics and static parameters. At each iteration, the state variables are propagated through a proposal

distribution conditional on the existing parameters. The sufficient statistics are updated according to their recursive formulation and finally new parameters are simulated from a proposal distribution conditioned on the sufficient statistics. The success of algorithms which follow an approach based on sufficient statistics is dependent on the mixing properties of the Markov kernels within the algorithm [56]. Information about the parameters may not always accumulate in the PF due to the degeneracy of paths introduced by resampling. The accumulation of errors in the PF may lead to the degeneracy of the static parameters [56].

An approach not based on the requirement of sufficient statistics for the joint estimation of the state and static parameters for the posterior distribution, $p(\boldsymbol{x}_{1:T}, \boldsymbol{\theta}|\boldsymbol{y}_{1:T})$, is proposed in [57]. This approach is based on Markov chain Monte Carlo (MCMC) techniques. A standard MCMC technique commonly used to obtain samples from an unknown distribution is known as the Metropolis-Hastings (MH) algorithm. The MH algorithm obtains samples from an unknown distribution through the generation of a Markov chain. Firstly, a proposed sample is generated from a known proposal distribution, $x^* \sim q(x^*|x_k)$. The proposed sample is accepted as x_{k+1} based on the following probability

$$\min\left(1, \frac{P(x^*)q(x^*|x_k)}{P(x_k)q(x_k|x^*)}\right). \tag{3.38}$$

If the proposed sample is rejected, then the old sample is kept through to the next time step, $x_{k+1} = x_k$. The approach presented in [57] states that it is possible to target the full posterior distribution with a MH algorithm through the following selection of the proposal distribution

$$q((\boldsymbol{x}^*_{1:T}, \boldsymbol{\theta}^*)|(\boldsymbol{x}_{1:T}, \boldsymbol{\theta})) = q(\boldsymbol{\theta}^*|\boldsymbol{\theta})p(\boldsymbol{x}^*_{1:T}|\boldsymbol{y}_{1:T}, \boldsymbol{\theta}^*). \tag{3.39}$$

This is equivalent to first obtaining a proposed sample for the static parameters, $\boldsymbol{\theta}^* \sim q(\boldsymbol{\theta}^*|\boldsymbol{\theta})$, followed by obtaining a proposed sample for the state space given the proposed static parameters, $\boldsymbol{x}^*_{1:T} \sim p(\boldsymbol{x}_{1:T}|\boldsymbol{y}_{1:T}, \boldsymbol{\theta}^*)$. The corresponding MH acceptance probability is then given by

$$\min\left(1, \frac{p(\boldsymbol{x}^*_{1:T}, \boldsymbol{\theta}^*|\boldsymbol{y}_{1:T})q((\boldsymbol{x}_{1:T}, \boldsymbol{\theta})|(\boldsymbol{x}^*_{1:T}, \boldsymbol{\theta}^*))}{p(\boldsymbol{x}_{1:T}, \boldsymbol{\theta}|\boldsymbol{y}_{1:T})q((\boldsymbol{x}^*_{1:T}, \boldsymbol{\theta}^*)|(\boldsymbol{x}_{1:T}, \boldsymbol{\theta}))}\right), \tag{3.40}$$

and it is shown in [57] that this simplifies to the following acceptance probability

$$\min\left(1, \frac{p(\boldsymbol{y}_{1:T}|\boldsymbol{\theta}^*)p(\boldsymbol{\theta}^*)q(\boldsymbol{\theta}|\boldsymbol{\theta}^*)}{p(\boldsymbol{y}_{1:T}|\boldsymbol{\theta})p(\boldsymbol{\theta})q(\boldsymbol{\theta}^*|\boldsymbol{\theta})}\right). \tag{3.41}$$

However, there is also no analytical expression available for the posterior distribution given a known static parameter which is required for sampling, $p(\boldsymbol{x}_{1:T}|\boldsymbol{y}_{1:T}, \boldsymbol{\theta})$. It was proposed that a numerical approximation for this posterior distribution be obtained through a PF algorithm. In addition, the PF

presents a numerical approximation of the marginal likelihood, $p(\boldsymbol{y}_{1:T}|\boldsymbol{\theta})$, at no additional computational cost. This numerical approximation for the marginal likelihood is available from the unnormalised weights in the PF algorithm

$$\hat{p}(\boldsymbol{y}_{1:T}|\boldsymbol{\theta}) = \prod_{k=1}^{T} \hat{p}(\boldsymbol{y}_k|\boldsymbol{y}_{1:k-1}) = \prod_{k=1}^{T} \sum_{i=1}^{N} w_k^i. \tag{3.42}$$

This numerical approximation for the marginal likelihood is used in the acceptance probability of the MH algorithm in Equation 3.41, which is targeted at the full posterior distribution. The disadvantage of this method, referred to as the particle marginal Metropolis-Hastings (PMMH) sampler, is that it is not sequential and hence requires all the observations to obtain estimates for the states and static parameters. The PMMH sampler is summarised for completeness in Algorithm 3.5.

Algorithm 3.5 Particle marginal Metropolis-Hastings sampler

Initialisation: $i = 0$

Sample $\boldsymbol{\theta}_0 \sim q_0(\boldsymbol{\theta})$

Sample $(\boldsymbol{x}_{1:T})_0 \sim \hat{p}(\boldsymbol{x}_{1:T}|\boldsymbol{y}_{1:T}, \boldsymbol{\theta}_0)$ using a PF such as in Algorithm 3.2.

for $i = 1,...,N$ **do**

Sample $\boldsymbol{\theta}^* \sim q(\boldsymbol{\theta}^*|\boldsymbol{\theta}_{i-1})$

Sample $\boldsymbol{x}_{1:T}^* \sim \hat{p}(\boldsymbol{x}_{1:T}|\boldsymbol{y}_{1:T}, \boldsymbol{\theta}^*)$ using a PF such as in Algorithm 3.2.

Accept $(\boldsymbol{x}_{1:T})_i = \boldsymbol{x}_{1:T}^*$ according to min $\left(1, \frac{\hat{p}(\boldsymbol{y}_{1:T}|\boldsymbol{\theta}^*)p(\boldsymbol{\theta}^*)q(\boldsymbol{\theta}_{i-1}|\boldsymbol{\theta}^*)}{\hat{p}(\boldsymbol{y}_{1:T}|\boldsymbol{\theta}_{i-1})p(\boldsymbol{\theta}_{i-1})q(\boldsymbol{\theta}^*|\boldsymbol{\theta}_{i-1})}\right)$

Else $(\boldsymbol{x}_{1:T})_i = (\boldsymbol{x}_{1:T})_{i-1}$

end for

The next chapter describes the radar simulator that was designed and implemented and introduces the state space models of an extended target.

CHAPTER 4

TARGET & SENSOR MODELLING APPROACH

4.1 INTRODUCTION

The first step required in any tracking application based upon a Bayesian structure is that of defining the target with a state space representation. The state vector includes the hidden dynamic states. The state space model includes a statistical description of how the states vary with time, and how the states are related to the observations.

This chapter describes the simulator which was designed to simulate the target and the HRR radar signals observed from the target at each time step. The state space representation and models of the target, its motion, and radar observations are also presented.

4.2 TARGET DESCRIPTION

A target is represented as a set of points based on the assumption that a target consists of multiple dominant scatterers [6]. The points are located in a 2-dimensional space as illustrated by an example in Figure 4.1. It is assumed that the number of persistent scatterers is fixed and constant during the observation period [7]. The dimensions are referred to as the down range, represented by $x^{\rightarrow}$, and cross-range, represented by $x^{\perp}$. The radar is stationary and located at the origin of the co-ordinate system. The down range dimension corresponds to the look direction of the radar. The cross-range dimension is perpendicular to the down range dimension with the 0 point representing the centre of the radar beamwidth which is aligned to the centroid of rotation of the target. Figure 4.2 illustrates the down range and cross-range dimensions relative to a target and the radar in a 2-D space. In reality, the maximum distance to a target that can result in the collection of a HRR profile, which corresponds

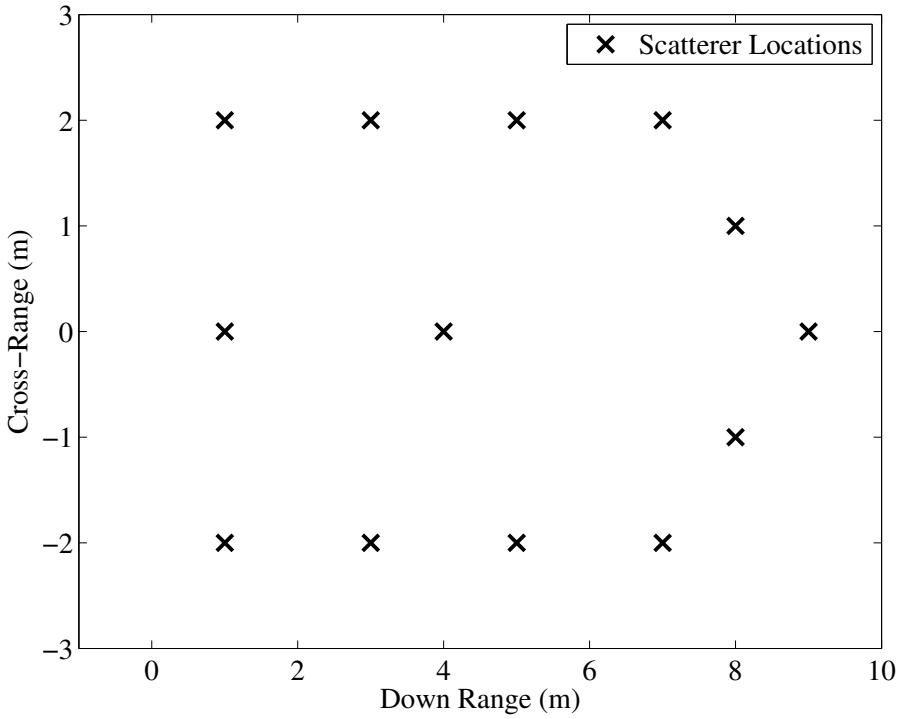

Figure 4.1: Example of a target represented with dominant scatterers. Zero reference point of axes shifted to [10000,0].

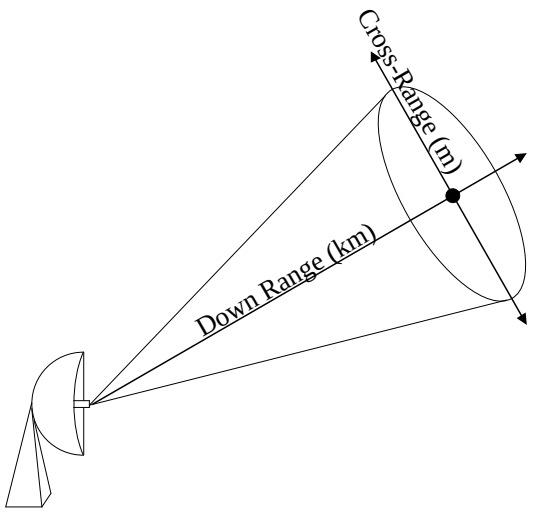

Figure 4.2: Illustration of the axes relative to a target and the stationary radar.

to the down range dimension, is dependent on the operating characteristics of the radar system. The minimum and maximum extent of the target in the cross-range is dependent on the range resolution of the radar system and the dimensions of the target respectively.

4.3 RADAR SIMULATOR

A HRR radar simulator was designed in order to easily obtain radar measurements from different targets in a controlled environment. This allowed for the full control of the target and associated parameters. This also allowed for the comparison between the results obtained from the tracking algorithms and the true underlying parameters.

The output required from a radar simulator influences the manner in which the simulation is carried out. A RCS simulator requires a detailed electromagnetic approach because the amplitude of the simulated returns are required to approximate the amplitude of the true world returns. The HRR simulator designed was not required to model the electromagnetic phenomena to such a degree in order to achieve the required HRR profiles.

The HRR radar simulator consists of 3 main subsystems

1. target creation,
2. target update,
3. and radar signal processing.

Target Creation

The target creation subsystem deals with the initial description of the target in the simulation space. It is assumed that the target is a rigid body with no moving parts, as is assumed in standard ISAR processing [4], and consists of a set of dominant scatterers. The inputs for this subsystem include:

1. The number of dominant scatterers used to represent the target.
2. The physical dimensions of the target.
3. A vector including the down range and cross-range co-ordinates for each of the dominant scatterers. Alternatively, a parameter can be set which results in the dominant scatterers being uniformly distributed within the specified target dimensions.
4. The amplitude of the reflection received by the radar of each dominant scatterer.

In real world systems the amplitude of a reflection received by the radar from a target is dependent on the distance to the target, the power of the waveform transmitted by the radar system and several other factors. In reality the amplitude can vary to a large degree between time steps, and hence the amplitude is not a feature which is utilised for tracking a dominant scatterer. The only criteria that the amplitude is required to meet is to be large enough to overcome a threshold which separates the dominant scatterers from noise. Owing to the persistent dominant scatterer assumption [7], all dominant scatterers met this criteria.

The output of the target creation subsystem is a structure array which completely describes the target and is utilised and further modified by the other subsystems.

Target Update

The target update subsystem applies the motion models, elaborated on further in Section 4.5, to the co-ordinates of the dominant scatterers. This essentially determines the true location of each of the dominant scatterers at each time step of the simulation. The structure array describing the target is updated with this information before being transferred to the radar signal processing subsystem.

Radar Signal Processing

The different types of backscatter found in radar systems were discussed in Section 2.2. In this research only high frequency optical scattering was considered, and more specifically, direct illumination scattering. This is referred to as the point scatterer model and produces a return with a specific amplitude and phase when illuminated by the radar. For a single scatterer, the radar return is given by

$$s_r(t) = \sigma_{\text{RCS}}\, s(t - \delta_t), \tag{4.1}$$

where $s(t)$ is the signal transmitted by the radar, σ_{RCS} represents the amplitude of the returned signal based on the radar cross section and range which is a specified input, and δ_t represents the time period between when the signal was transmitted and received. In our application it is assumed that δ_t is only a function of the distance between the radar and the scatterer. This time delay translates into a phase difference between the original transmitted signal and received signal.

The radar waveform selected for the synthesis of the HRR profiles was a SFW as described in Section 2.5. The radar parameters utilised by the simulator are listed in Table 4.1, followed by the algorithm

to obtain a HRR profile based on the use of SFWs described by Algorithm 4.1.

Table 4.1: SFW based HRR radar simulator parameters.

Symbol	Radar Parameter
Δf	Step frequency
n	Number of narrowband pulses transmitted in a burst
f_0	Centre frequency
PRF	Effective pulse repetition frequency
SNR	Signal-to-noise ratio

Algorithm 4.1 Synthetic HRR profile generation through SFW processing

Initialisation: Complex radar returns, $S = 0$, and discrete frequencies, $f = \left(\frac{-n\Delta f}{2} : \Delta f : \frac{n\Delta f}{2}\right) + f_0$.

for $h = 1 : n$ **do**

for $d = 1 : M$ **do**

Calculate the range to dominant scatterer d, $R = \sqrt{x_d^{\rightarrow 2} + x_d^{\perp 2}}$.

Update the radar returns, $S(h) = S(h) + \sqrt{\sigma_{\mathrm{RCS}_d}} \exp\left(\frac{-4j\pi f(h)R}{c}\right)$.

end for

end for

Calculate the power in the complex radar returns.

Add complex white noise, according to the SNR, to the complex radar returns.

Multiply the complex radar returns by the Hamming window.

Perform inverse fast Fourier transform on the complex radar returns to obtain the HRR profile, $HRRP = IFFT(S)$.

* Where $x_d^{\rightarrow}$ and $x_d^{\perp}$ represent the down range and cross-range co-ordinates for scatterer d at the current time step respectively.

It is noted that the noise is added to the input signal at a specific SNR. The processing performed to obtain the HRR profile may induce signal gain increasing the SNR of the HRR profile. It is assumed that there is no motion between the radar and target during the collection of the data which is utilised to obtain a single HRR profile. This assumption negated the requirement for additional radar signal processing during the collection of measurements for a single HRR profile [22]. Algorithm 4.1 was

applied at each time step to obtain a set of synthetic HRR profiles. The validity of the radar simulator was verified by comparing the extracted observations from the HRR profiles with the true values expected for the target in a noiseless system.

4.4 OBSERVATION EXTRACTION

Mathematically, a single HRR profile is represented by

$$s_o(t) = \sum_i \sigma_{\text{RCS}_i} e^{\frac{-j4\pi f_0 R_i}{c}} x\left(t - \frac{2R_i}{c}\right) + e_n, \tag{4.2}$$

where i represents the scatterer index, $x(t)$ represents the point spread function, which is related to the bandwidth of the transmit waveform used by the radar, R_i represents the distance between the radar and scatterer i, f_0 represents the radar operating carrier frequency, c represents the speed of light, and e_n represents complex noise which is induced during the signal processing of the radar measurements. The procedure described by Algorithm 4.1 results in a discretised form of the above equation.

The location in a HRR profile which results in the most information about each dominant scatterer occurs at the time delay which corresponds to the range between the radar and the dominant scatterer. Generally, the magnitude of the HRR profile results in a peak at this point. However, as seen in Equation 4.2, the value at each discrete range in the HRR profile is a complex summation and may result in destructive interference when two or more dominant scatterers are located within a close proximity with respect to range to the radar. Other peaks in the magnitude of the HRR profile may correspond to noise, or side lobes which are unwanted signal processing artifacts. The first processing step performed was thresholding of the magnitude of the HRR profile. This was performed in order to isolate the peaks related to dominant scatterers. The threshold level was manually set according to the SNR in the simulation. The discrete ranges corresponding to the peaks in the magnitude of the HRR profile were then obtained through a basic peak detection algorithm. The corresponding range obtained from the peaks represent the range to each dominant scatterer.

The range to each dominant scatterer is the only information that can be extracted from the magnitude of the HRR profile. However, additional information can be extracted from the complex HRR profile by finding the phase at the extracted range to each dominant scatterer. The phase measurement is a highly accurate range measurement which suffers from a very large degree of ambiguity. The phase information obtained for a dominant scatterer from an individual HRR profile does not provide any usable information due to a large degree of ambiguity. However, finding the difference in phase,

referred to as the delta phase, for a dominant scatterer between two consecutive HRR profiles results in an informative observation. The delta phase is related to the radial velocity of a single dominant scatterer through

$$v_r = \frac{\Delta\phi\lambda}{4\pi\Delta t}, \tag{4.3}$$

where $\Delta\phi$ represents the delta phase and λ represents the wavelength.

Owing to the discrete nature of the HRR profile, a parabola was fit using the discrete peak of the HRR profile and its two neighbouring samples [58]. This allowed for a better approximation of the true observed range value. The required shift to the estimated true peak of discrete HRR profile $X[k]$, whose peak is located at discrete instance k_0 is

$$\Delta k = \frac{-\frac{1}{2}\{X[k_0+1]-X[k_0-1]\}}{X[k_0-1]-2X[k_0]+X[k_0+1]}. \tag{4.4}$$

4.5 STATE SPACE MODELLING

Two different discrete state space models were developed and are presented individually below.

4.5.1 Model I

This model was presented by the author in [59] and is characterised by:

1. Rotational motion only,
2. constant radial velocity,
3. noise added to the position of the dominant scatterers,
4. and range only measurements,

and is detailed below.

4.5.1.1 State Space Representation

The state vector is represented by

$$\boldsymbol{x}_k = \left[\; x^{\rightarrow}_{1,k}, x^{\perp}_{1,k}, \ldots, x^{\rightarrow}_{M,k}, x^{\perp}_{M,k} \; \right], \tag{4.5}$$

where $x_{c,k}^{\rightarrow}$ represents the down range co-ordinate and $x_{c,k}^{\perp}$ represents the cross-range co-ordinate for scatterer $c = [1,\ldots,M]$ at discrete time instant k.

4.5.1.2 Motion Model

Only rotational motion about a fixed point in space is explored. The motion model parameters are assumed static, owing to the fact that over the time interval when measurements are collected, the motion model parameters do not vary noticeably. Analysing rotational motion results in two static parameters which characterise the motion

$$\boldsymbol{\theta} = \left[\ \theta_1, \theta_2\ \right] = \left[\ x_{\times}, \omega_r\ \right], \tag{4.6}$$

where $x_{\times}$ is the distance to the center of rotation of the rigid body from the radar in the down range and ω_r represents the angular velocity of the rigid body. The next state is determined through the following generation functions

$$\begin{aligned} x_{c,k}^{\rightarrow} &= (x_{c,k-1}^{\rightarrow} - \theta_1)\cos(\theta_2 \Delta t) - x_{c,k-1}^{\perp}\sin(\theta_2 \Delta t) + \theta_1 + w_k, \\ x_{c,k}^{\perp} &= (x_{c,k-1}^{\rightarrow} - \theta_1)\sin(\theta_2 \Delta t) + x_{c,k-1}^{\perp}\cos(\theta_2 \Delta t) + w_k, \end{aligned} \tag{4.7}$$

where Δt is the constant time elapsed from discrete time instance $k-1$ to k. The stochastic disturbance, w_k, is a zero mean Gaussian random variable.

4.5.1.3 Observation Model

For this model, the observation vector consists of only the range measurements

$$\boldsymbol{y}_k = \left[\ R_{1,k},\ldots,R_{c,k}\ \right], \tag{4.8}$$

where $R_{c,k}$ represents the range of scatterer c at discrete time instance k. In terms of a generation function, the observations are modelled as

$$R_{c,k} = \sqrt{x_{c,k}^{\rightarrow\,2} + x_{c,k}^{\perp\,2}} + v_k, \tag{4.9}$$

where v_k is a zero mean Gaussian random variable.

4.5.2 Model II

In contrast to Model I, this model utilised a polar co-ordinate state vector representation to limit the non-linearities to the observation model only. This model does not consist of static parameters as the

assumption of a uniform rotational rate was not made, and the co-ordinates for the centroid of rotation were assumed known.

4.5.2.1 State Space Representation

The state vector is represented by

$$\boldsymbol{x}_k = \left[\; r_{1,k}, \theta_{1,k}, \ldots, r_{M,k}, \theta_{M,k}, \omega_k \; \right], \tag{4.10}$$

where $r_{c,k}$ and $\theta_{c,k}$ represent the radius and angle of the scatterer $c = [1, \ldots, M]$ relative to the centroid of rotation and the cross-range axis respectively, and ω_k is the angular velocity of the target at discrete time instance k. An example of the state space representation of a random target consisting of two dominant scatterers is illustrated in Figure 4.3.

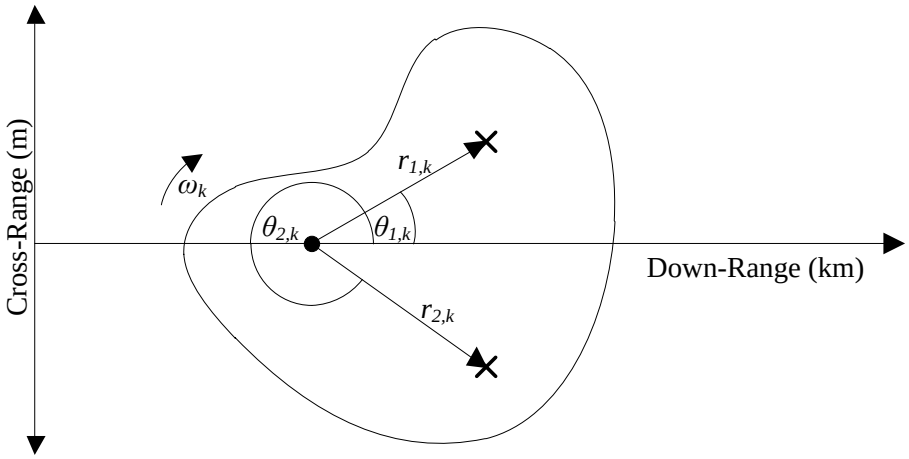

Figure 4.3: Illustration of how the state vector relates to a target in model II. The centre point on the target represents the centroid of rotation.

4.5.2.2 Motion Model

The motion of each dominant scatterer is directly related to the motion of the target. However, a stochastic variation between scatterers was also included. The rotational motion of the target was modelled with a discrete almost constant angular velocity random acceleration model [31]. The

motion model for each state is given by

$$\begin{aligned} r_{c,k} &= r_{c,k-1} + p_{c,k}, \\ \theta_{c,k} &= \theta_{c,k-1} + \omega_{k-1}\Delta t + \frac{1}{2}\Delta t^2 q_k, \\ \omega_k &= \omega_{k-1} + \Delta t q_k, \end{aligned} \tag{4.11}$$

where $p_{c,k}$ and q_k represent zero mean Gaussian random variables.

4.5.2.3 Observation Model

The observation vector includes the range and delta phase measurements,

$$\boldsymbol{y}_k = \left[\; R_{1,k}, \Delta\phi_{1,k}, \ldots, R_{M,k}, \Delta\phi_{M,k} \; \right]. \tag{4.12}$$

In terms of a generation function, the range observations are modelled as

$$R_{c,k} = \sqrt{\left(r_{c,k}\cos(\theta_{c,k}) + x_{\times}^{\rightarrow}\right)^2 + \left(r_{c,k}\sin(\theta_{c,k})\right)^2} + v_k, \tag{4.13}$$

where $x_{\times}^{\rightarrow}$ represents the location of the centroid of rotation in the down range, and v_k is a zero-mean Gaussian random variable.

The delta phase measurement is ambiguous on the interval $[-\pi;\pi]$ but is substantially less likely to wrap around the range in comparison with the absolute phase. The generation function for the delta phase of each scatterer is given by

$$\Delta\phi_{c,k} = \frac{4\pi\Delta R_{c,k}}{\lambda} + e_{\phi}, \tag{4.14}$$

where

$$\Delta R_{c,k} = \sqrt{\left(r_{c,k}\cos(\theta_{c,k}) + x_{\times}^{\rightarrow}\right)^2 + \left(r_{c,k}\sin(\theta_{c,k})\right)^2} - \sqrt{\left(r_{c,k-1}\cos(\theta_{c,k-1}) + x_{\times}^{\rightarrow}\right)^2 + \left(r_{c,k-1}\sin(\theta_{c,k-1})\right)^2},$$

λ is the wavelength of the transmitted signal, and e_{ϕ} is a noise term which corresponds to the effects of the complex noise term in Equation 4.2 on the delta phase measurement of each scatterer. In this application the noise term is induced due to the addition of Gaussian noise on the quadrature and in-phase channels in the radar receiver at a specific SNR as implemented in Algorithm 4.1. The effect of this noise on the delta phase, e_{ϕ}, was approximated with the Von Mises distribution, also referred to as the circular Gaussian distribution. The probability density function of the Von Mises distribution is given by

$$p(\theta|\theta_0, m) = \frac{1}{2\pi I_0(m)}\exp\{m\cos(\theta - \theta_0)\} \quad \theta \in [0, 2\pi) \tag{4.15}$$

where $I_0(m)$ is the zeroth-order Bessel function of the first kind, θ_0 is the mean, and m is the concentration parameter. The mean and concentration parameter are analogous to the mean and inverse variance of a univariate Gaussian respectively. In this application the mean was equal to 0 and the concentration parameter was found to be dependent on the SNR in the radar simulator.

When compared with the general expression typically used to describe the observation generation function in Equation 3.1, the generation function in Equation 4.14 is dependent on the state at the previous time step which violates the Markovian property of the state space model. This is illustrated in Figure 4.4.

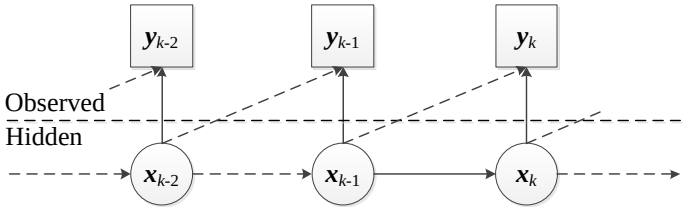

Figure 4.4: Graphical illustration of the state space model for model II prior to state space augmentation.

The state vector was augmented with the states from the previous time step to prevent the violation of the Markovian property, since it is a fundamental property in the development of particle filtering. The augmentation of the state vector is illustrated in Figure 4.5.

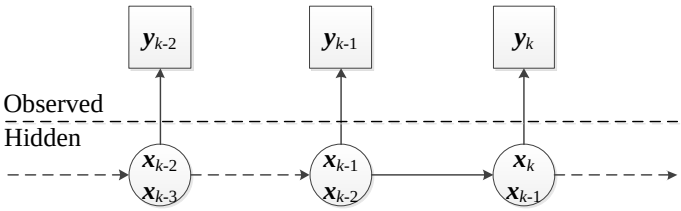

Figure 4.5: Graphical illustration of the state space model for model II after state space augmentation.

Table 4.2 summarises all the assumptions which were made throughout the state space modelling.

Table 4.2: State space modelling assumptions.

Assumption	Validity
The dominant scatterer assumption.	This assumption is extensively used in literature [6, 7, 60].
Persistent dominant scatterers (dominant scatterers are assumed to be visible in all HRR profiles)	Observed in literature [7]. The total angle of rotation was minimised in Model II to increase the validity of the assumption. Future research could eliminate this assumption.
Fixed number of persistent dominant scatterers.	The total angle of rotation was minimised in Model II to increase the validity of the assumption. Future research could eliminate this assumption.
Fixed angular velocity (Model I).	Time period for the collection of HRR profiles was minimised to increase validity of the assumption. Assumption dropped in Model II.
Gaussian and Von Mises distributed noise perturbing the range and delta phase measurements respectively.	This may not be consistent with real world measurements since the radar simulator does not simulate many noise inducing effects which occur in reality, such as other scattering mechanisms. However, verified to be valid through simulation of the radar simulator used to obtain measurements.
Perfect data association.	This is not a valid assumption. Data association was considered outside of the scope of this research as discussed in Section 3.2.

CHAPTER 5

RESULTS & DISCUSSION

5.1 INTRODUCTION

This chapter illustrates and discusses the results obtained by applying the Bayesian inference techniques described in Sections 3.5 and 3.6 to the state space models described in Section 4.5. The targets generated for the experiments in this section are considered generic and do not conform to a specific type of target, such as a maritime vessel.

5.2 MODEL I

5.2.1 Observation Extraction

A randomly generated target consisting of 5 dominant scatterers was created. The number of dominant scatterers is related to the dimensionality of the state space. In this application the number of dominant scatterers was selected to demonstrate the algorithms ability to handle dominant scatterers overlapping and dominant scatterers located at different radii from the centroid of rotation, the influence of varying this parameter was investigated in Section 5.3.4. The trajectory of the dominant scatterers, based on the motion model for Model I is illustrated in Figure 5.1. The parameters of the target and its motion are listed in Table 5.1. The angular velocities and motion model variance were selected arbitrarily with the aim of a sufficient amount of displacement of the location of the dominant scatterers in the cross-range dimension during the duration of the simulation.

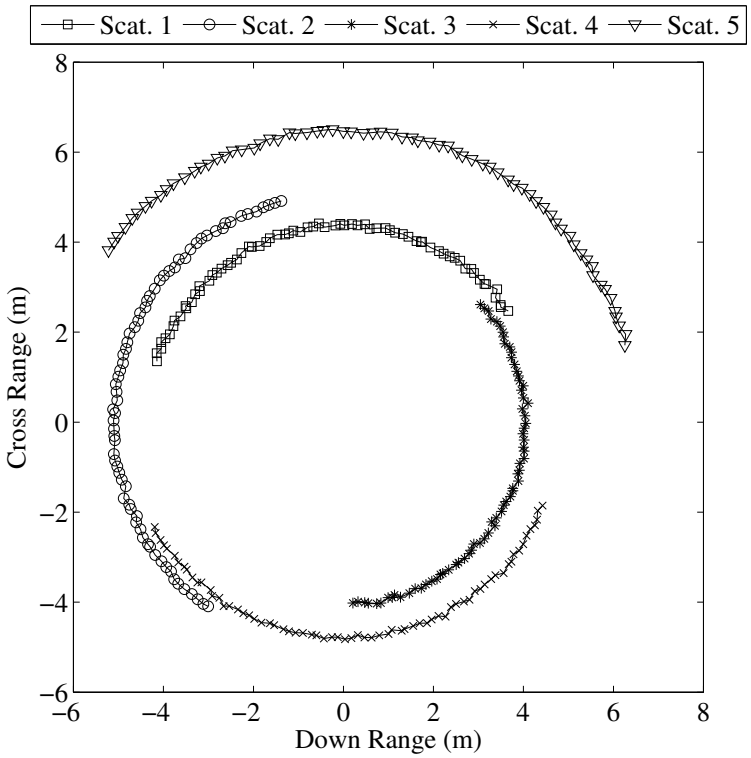

Figure 5.1: Trajectory of a random target consisting of 5 dominant scatterers. The direction of rotation of the target is anti-clockwise. Zero reference point of axes shifted to [10000,0].

Table 5.1: Defining parameters of the random target whose trajectory is illustrated by Figure 5.1.

Parameter	**Parameter Value**
Number of dominant scatterers	5
Angular velocity (ω_r)	5 rad/s
Maximum target angular velocity ($\omega_{r,\max}$)	6 rad/s
Motion model variance (σ_w^2)	1×10^{-3} m
Centroid of rotation co-ordinates($[x_\times, 0]$)	$[10000, 0]$ m
Total time elapsed	0.448 s
Time elapsed between discrete time instances (Δt)	6.4 ms

The parameters of the radar used to obtain the HRR profiles are listed in Table 5.2. The range to the centroid of rotation, the simulation time, and the radar operating parameters were selected based on similar applications found in literature [6, 23] as well as real world radar data which was available

and is the focus of future research [61].

Table 5.2: SFW based HRR radar simulator parameter values.

Radar Parameter	Parameter Value
Step Frequency (Δf)	10 MHz
Number of Pulses (n)	64
Centre Frequency (f_0)	10 GHz
Effective Pulse Repetition Frequency (PRF)	10 KHz
Signal-to-noise Ratio (SNR)	20 dB

The influence of the selected radar parameters on the radar operating characteristics described in Chapter 2 are listed in Table 5.3.

Table 5.3: SFW based HRR radar simulator operating characteristics.

Radar Characteristic	Value	Description
Unambiguous Target Range (R_u)	15 km	Maximum range at which target radial distance is unambiguous.
Unambiguous Target Range Window ($R_{u,w}$)	15 m	Limits the physical extent of the target which can be observed entirely in the window.
Range Resolution (ΔR_{cell})	0.23 m	Minimum distance at which two scatterers can be observed through separate returns.
Maximum Range Difference (ΔR)	7.5 mm	Relates to maximum radial velocity before phase wrap occurs.

The unambiguous target range is inversely related to the PRF of the radar and describes the maximum range in which the unambiguous target range window may be located. The unambiguous target range window is inversely related to the step frequency as illustrated in Figure 5.2. The unambiguous target range window inherently limits the physical extent to which a target can be entirely observed in a HRR profile generated by the radar system. Since the inference techniques presented in this dissertation

will be unable to track the location of the dominant scatterers if their returns are not present in the HRR profiles, the step frequency is required to be carefully chosen to ensure that the entire target extent is located within the unambiguous target range window.

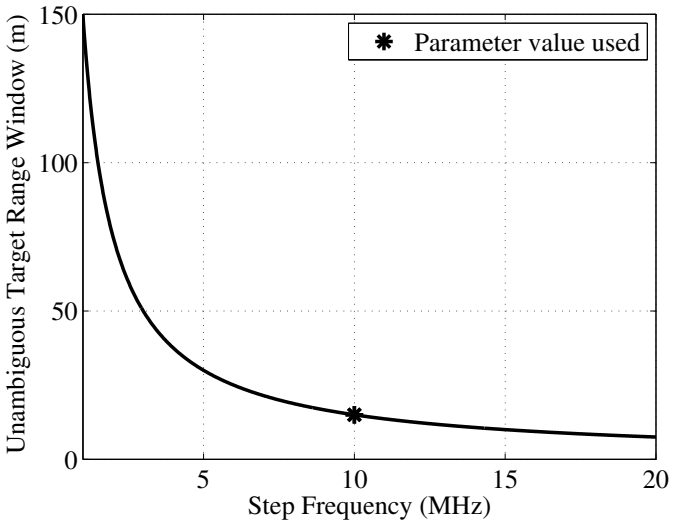

Figure 5.2: The relationship between the unambiguous target range window and the step frequency utilised by a SFW based radar.

However, the step frequency is also inversely related to the range resolution which describes the minimum range required between scatterers in order to distinguish the individual returns from the scatterers. This relationship is also dependent on the number of pulses used by the SFW radar. An illustration of the relationship between the range resolution and step frequency for a fixed number of pulses is illustrated in Figure 5.3.

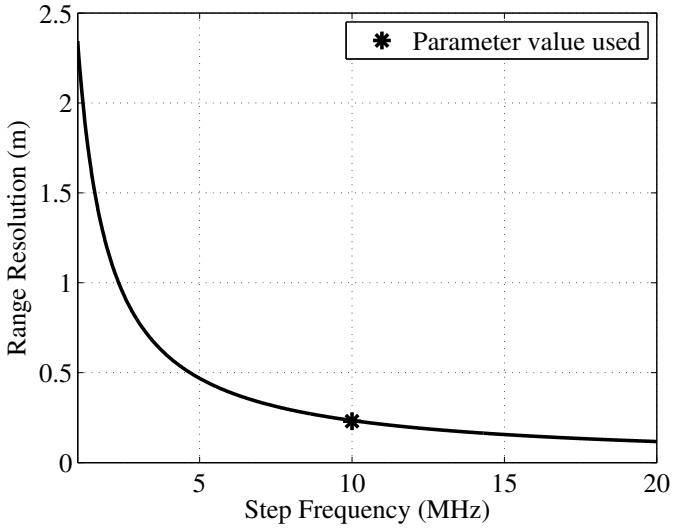

Figure 5.3: The relationship between the range resolution and the step frequency utilised by a SFW based radar with 64 pulses.

An illustration of the relationship between the range resolution and number of pulses with a fixed step frequency is illustrated in Figure 5.4.

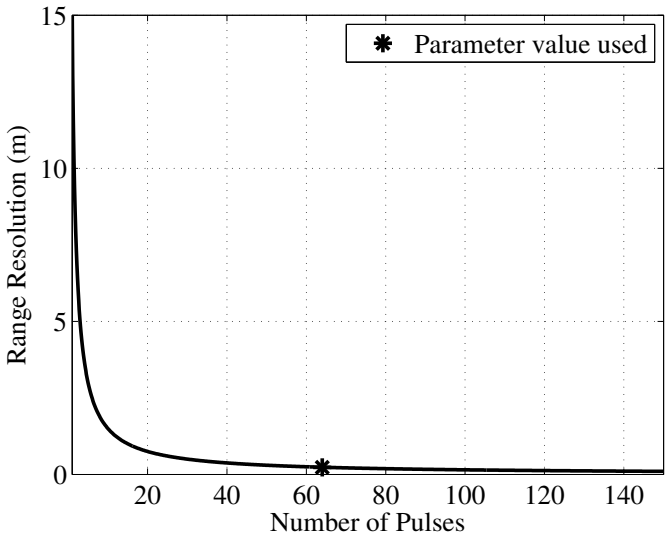

Figure 5.4: The relationship between the range resolution and the number of pulses utilised by a SFW based radar with a step frequency of 10 MHz.

A tradeoff between maximising the step frequency to obtain a finer range resolution and selecting a step frequency to match the target extent is highlighted by comparing Figures 5.2 and 5.3. Increasing

the number of pulses results in a finer range resolution, however this also increases the total time required to synthesis a single HRR profile. The centre frequency of the radar is inversely related to the maximum allowable change in range of a scatterer between any two HRR profiles. The change in range is caused by the motion that the target undergoes between HRR profiles. In this application the change in range is due to noise and rotational motion as described by the state space models in Section 4.5. In reality the change in range could also be influenced by translational motion which would need to be considered for the selection of the centre frequency. Knowledge of the elapsed time between HRR profiles converts the maximum allowable change in range of a scatterer to the maximum radial velocity that a scatterer may exhibit. Exceeding the maximum radial velocity would result in ambiguities in the delta phase measurement, hence rendering the delta phase measurement unusable. The relationship between the maximum radial velocity and the centre frequency of a SFW radar is illustrated in Figure 5.5. The centre frequency should be selected based on the expected radial velocity that the target is capable of generating. This results in the full utilisation of the dynamic range of the delta phase measurement.

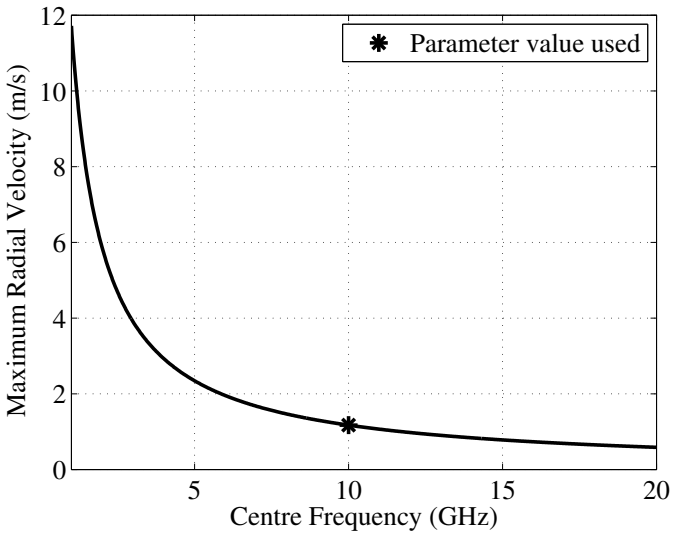

Figure 5.5: The relationship between the radial velocity and the centre frequency utilised by a SFW based radar.

As noted in Table 5.3, the maximum range at which a target can be located from the radar system is 15 km. The maximum extent of the target in range is 15 m, and for the target represented by Model II, the maximum radial velocity of each scatterer is 1.17 m/s. This is owing to the fact that the delta phase measurement is only observed in Model II. The magnitude of the HRR profiles observed from

the target in Figure 5.1 are graphically presented in Figure 5.6.

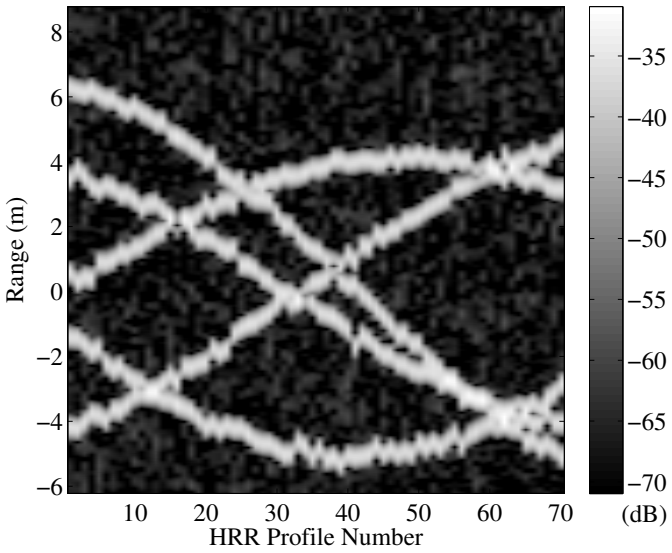

Figure 5.6: HRR profiles generated by the radar simulator based on the radar parameters in Table 5.2. Zero point of range axis shifted to 10000.

The observation vector for model I consists of the ranges for each of the dominant scatterers. The ranges extracted from the HRR profiles are illustrated in Figure 5.7.

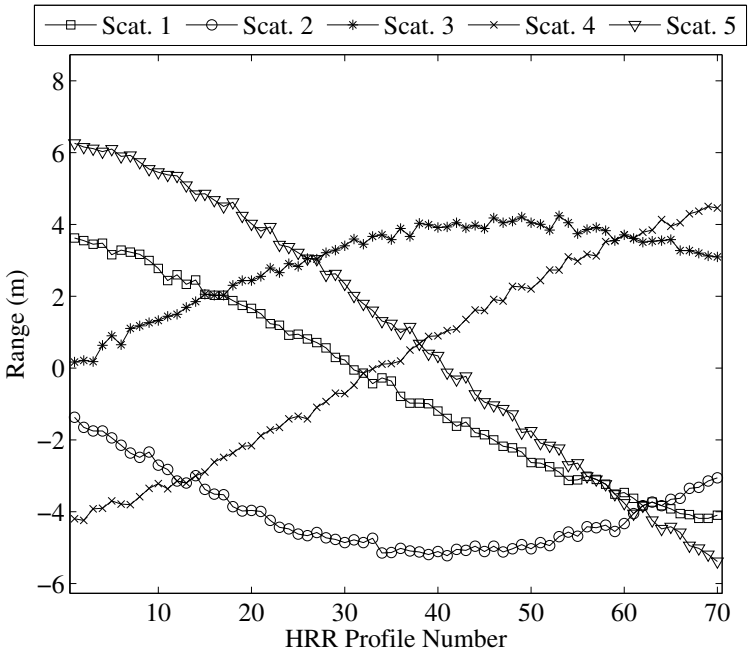

Figure 5.7: The range values extracted from the HRR profiles in Figure 5.6 for each dominant scatterer. Zero point of range axis shifted to 10000.

The observation standard deviation, σ_v, related to the Gaussian random variable in Equation 4.9, may vary depending on the presence of multiple dominant scatterers in the same vicinity. A maximum value of 5 cm was measured and utilised by the techniques applied on Model I.

5.2.2 Bootstrap Particle Filter Approach

The approach followed by [53] in which the state space is augmented with the static parameters was implemented since the framework of the BPF does not support static parameters. The first step in the implementation of the BPF is the initialisation of the particles. Each particle was initialised according to the following probability distributions,

$$\begin{aligned} \begin{bmatrix} x_c^{\rightarrow} \\ x_c^{\perp} \end{bmatrix} &\sim U\left(\begin{bmatrix} R_{I,c}-R_o, R_{I,c}+R_o \\ -\frac{R_E}{2}, \frac{R_E}{2} \end{bmatrix}\right), \\ x_{\times} &\sim U\left(R_D - \frac{R_{u,w}}{2}, R_D + \frac{R_{u,w}}{2}\right), \\ \omega_r &\sim U(0, \omega_{r,\max}), \end{aligned} \tag{5.1}$$

where $R_{I,c}$ are the initial range values observed in the first high range resolution profile, R_E is the targets maximum possible cross-range extent, R_o represents the influence of R_E on the range measurement, and $R_{u,w}$ represents the unambiguous radar range window. R_D represents the range at which a secondary low range-resolution tracking radar detects the extended target. It was assumed that this value corresponded to the true centroid of rotation and results in the initialisation of the down range centroid across the entire down range extent of the target. $U(a,b)$ represents the uniform distribution where a and b represent the minimum and maximum values respectively. The number of particles utilised by a PF is related to the accuracy of the representation of the filtering distribution and to the computational expense of the algorithm. Furthermore, the necessary number of particles required to achieve a specific accuracy is dependent on the complexity of the filtering distribution [62]. These results were obtained utilising a BPF consisting of 10000 particles. Performing the experiment utilising different numbers of particles showed no significant improvement in results with more then 10000 particles for a filtering distribution with the complexity associated with this application. This is further illustrated in Section 5.3.4. The inferred marginal posterior distributions for all the state variables at each time step are illustrated in Figures 5.8 to 5.13.

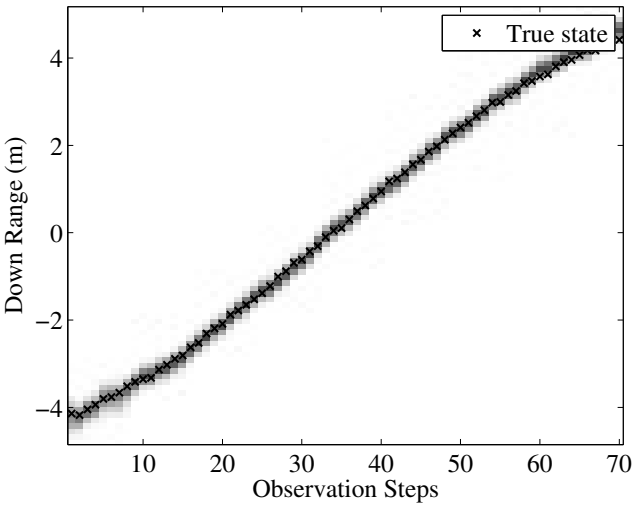

(a) The marginal filtering distribution of $x_1^{\rightarrow}$. Zero of down range dimension shifted to 10000.

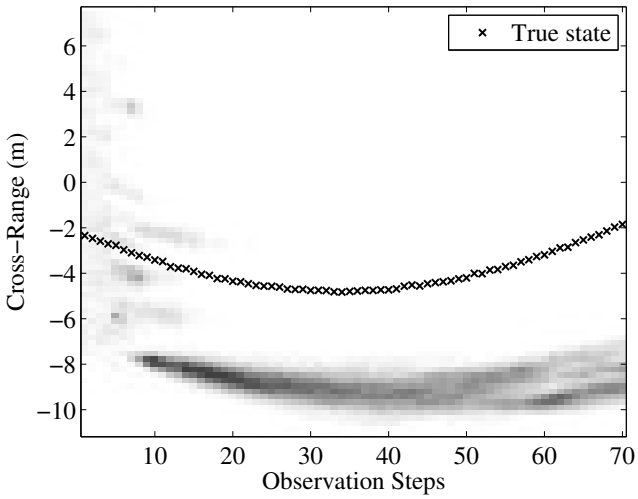

(b) The marginal filtering distribution of $x_1^{\perp}$.

Figure 5.8: The marginal filtering distribution of dominant scatterer 1, obtained at each time step for Model I with an augmented state vector through the BPF.

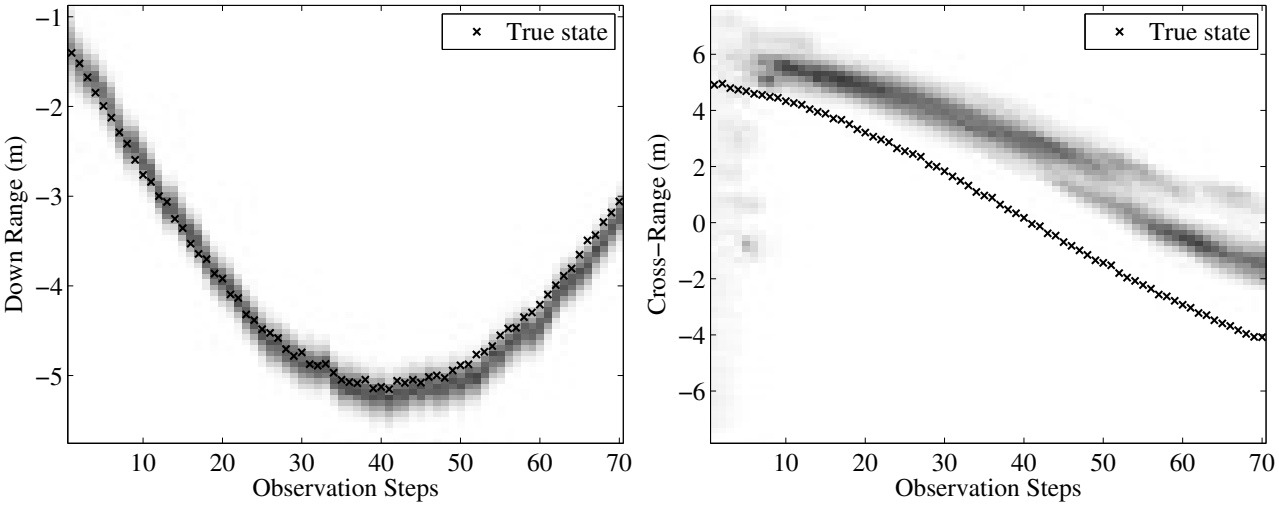

(a) The marginal filtering distribution of $x_2^{\rightarrow}$. Zero of down range dimension shifted to 10000.

(b) The marginal filtering distribution of $x_2^{\perp}$.

Figure 5.9: The marginal filtering distribution of dominant scatterer 2, obtained at each time step for Model I with an augmented state vector through the BPF.

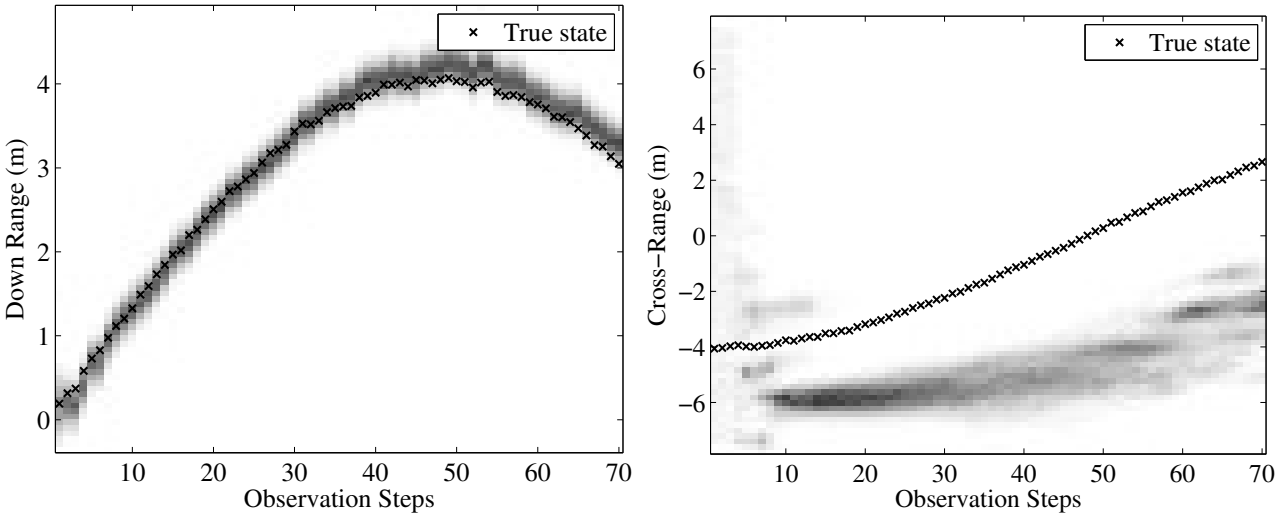

(a) The marginal filtering distribution of $x_3^{\rightarrow}$. Zero of down range dimension shifted to 10000.

(b) The marginal filtering distribution of $x_3^{\perp}$.

Figure 5.10: The marginal filtering distribution of dominant scatterer 3, obtained at each time step for Model I with an augmented state vector through the BPF.

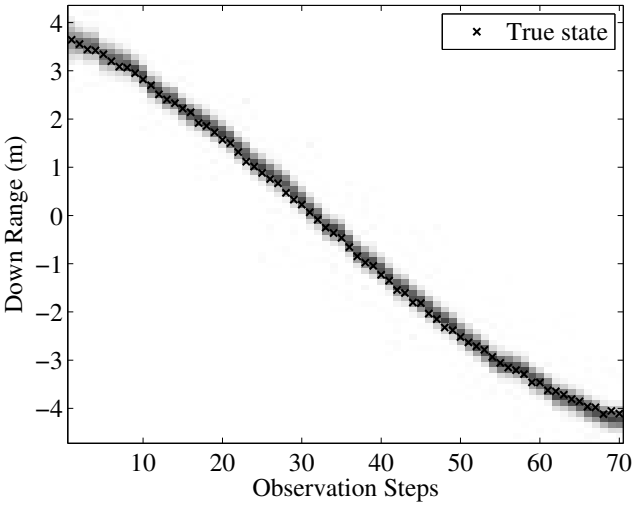

(a) The marginal filtering distribution of $x_4^{\rightarrow}$. Zero of down range dimension shifted to 10000.

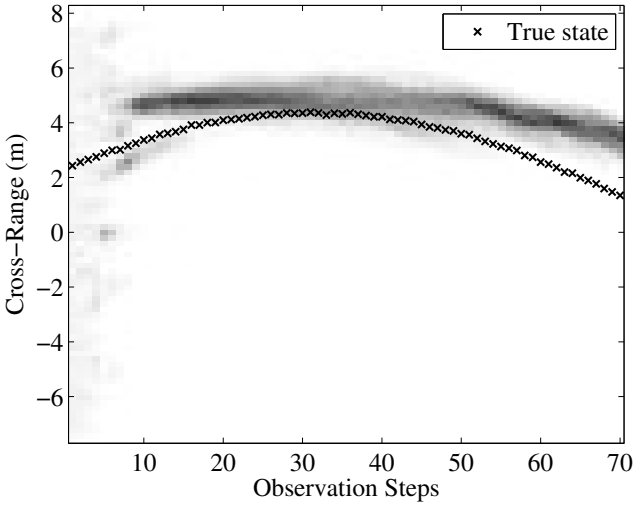

(b) The marginal filtering distribution of $x_4^{\perp}$.

Figure 5.11: The marginal filtering distribution of dominant scatterer 4, obtained at each time step for Model I with an augmented state vector through the BPF.

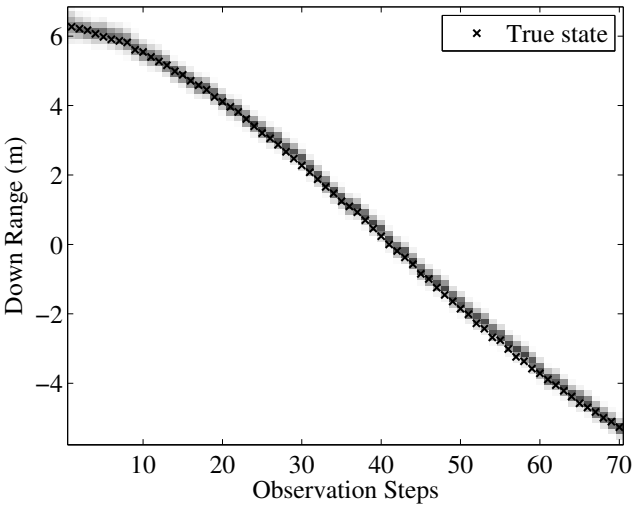

(a) The marginal filtering distribution of $x_5^{\rightarrow}$. Zero of down range dimension shifted to 10000.

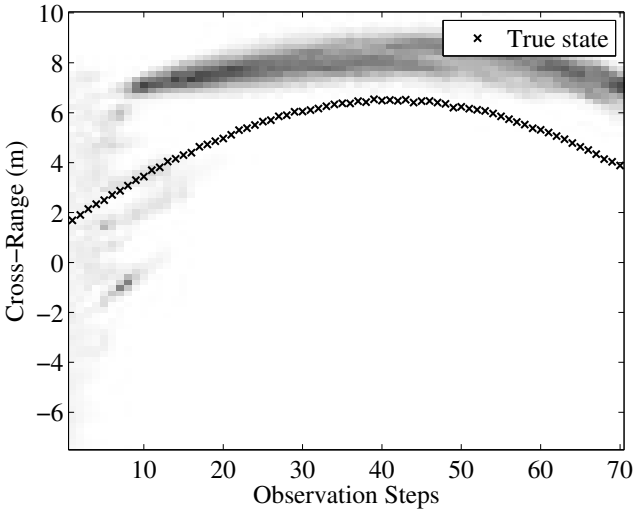

(b) The marginal filtering distribution of $x_5^{\perp}$.

Figure 5.12: The marginal filtering distribution of dominant scatterer 5, obtained at each time step for Model I with an augmented state vector through the BPF.

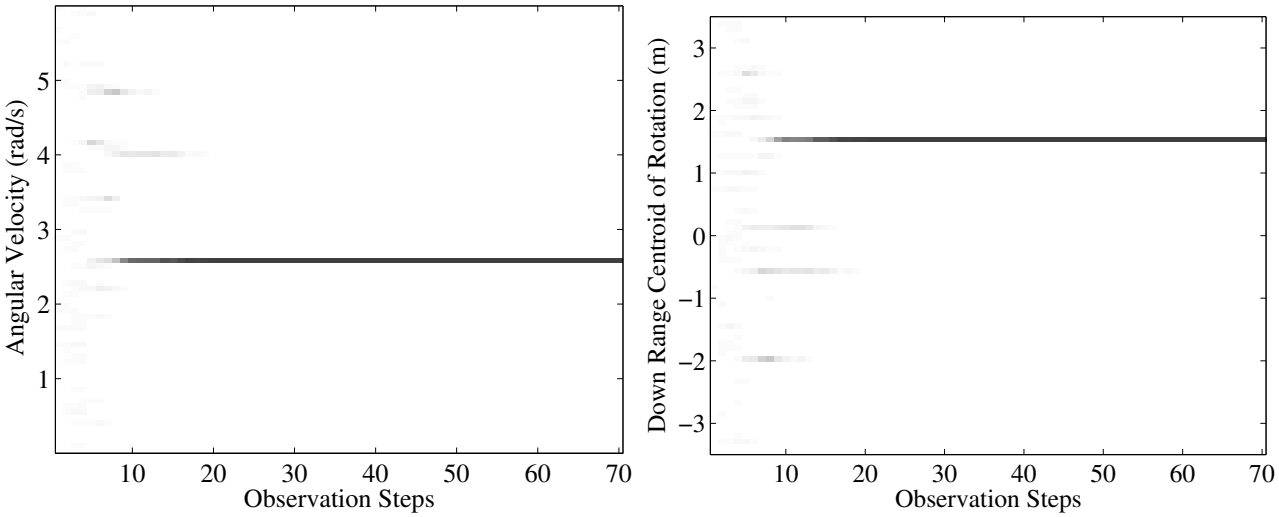

(a) The marginal filtering distribution of ω_r with a true value of 5 rad/s.

(b) The marginal filtering distribution of $x_\times$ with a true value of 10000. Zero of down range dimension shifted to 10000.

Figure 5.13: The marginal filtering distribution of the static parameters, obtained at each time step for Model I with an augmented state vector through the BPF.

It is clear from the results in Figures 5.8 to 5.13 that the filter fails to successfully track the location of the dominant scatterers in the cross-range dimension as well as the static parameters. The inclusion of static parameters in the state space results in severe filter degeneracy. However, the marginal filtering distributions for the down range dimension are accurate. This is due to the fact that the down range term in Equation 4.9 is commonly several magnitudes larger than that of the cross-range term. This results in the majority of the range observation relating to information about the down range dimension. A particle with incorrect states in the cross-range dimensions may still obtain a high weighting due to correct particle states in the down range dimensions. The degeneracy of the static parameters results in an irreversible loss of track in the cross-range dimensions due to sample impoverishment. This corresponds to results in literature [53].

5.2.3 Particle Markov Chain Monte Carlo Approach

The BPF was shown, in Figures 5.8 to 5.13, to clearly be insufficient at inferring the filtering distribution of a state space model which contains static parameters. The fact that the range observation predominantly contains information about the states which correspond to the down-range dimensions for the dominant scatterers was also identified as an application unique problem.

The PMMH sampler was identified in Section 3.6 as a MCMC method which is capable of estimating the static parameters and states of general state space models. The PMMH sampler was applied to jointly inferring the static parameters and states associated with model I, based on the same target and observations which were presented in Section 5.2.1. The inferred marginal posterior distributions for the state variables and static parameters are illustrated in Figures 5.14 to 5.18 and Figure 5.19 respectively. The PMMH sampler utilised a Gaussian proposal distribution for the proposal of the static parameters with a variance of 0.1. The PF utilised by the PMMH sampler was the BPF with 10000 particles. The PMMH sampler was run with 20000 iterations. These parameters resulted in sufficient Markov chain convergence.

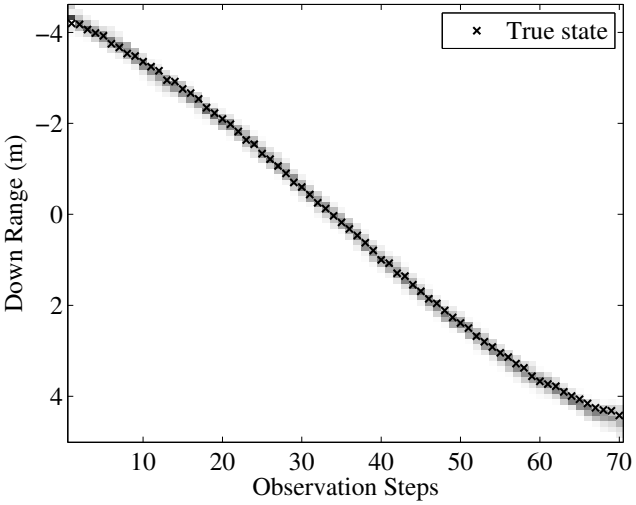

(a) The marginal posterior distribution of $x_1^{\rightarrow}$. Zero of down range dimension shifted to 10000.

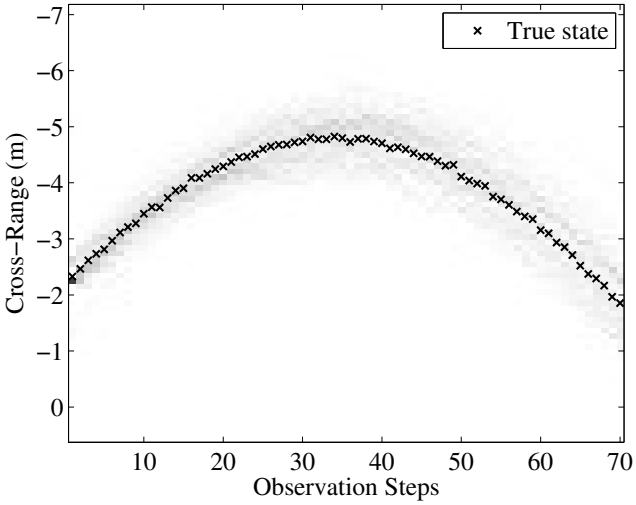

(b) The marginal posterior distribution of $x_1^{\perp}$.

Figure 5.14: The marginal posterior distributions for the states associated with dominant scatterer 1 obtained with the PMMH sampler.

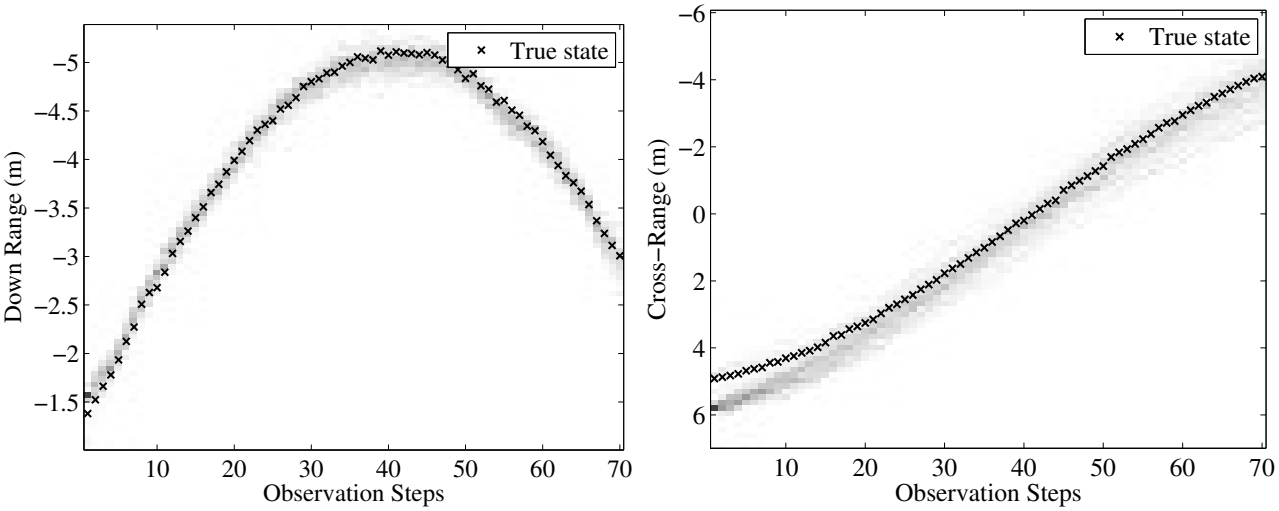

(a) The marginal posterior distribution of $x_2^{\rightarrow}$. Zero of down range dimension shifted to 10000.

(b) The marginal posterior distribution of $x_2^{\perp}$.

Figure 5.15: The marginal posterior distributions for the states associated with dominant scatterer 2 obtained with the PMMH sampler.

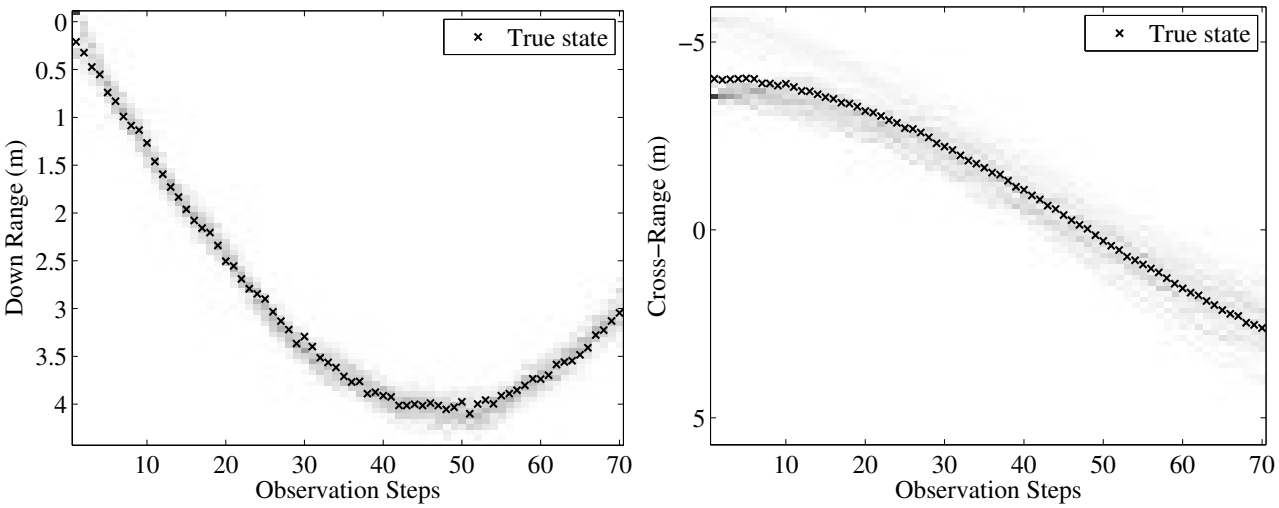

(a) The marginal posterior distribution of $x_3^{\rightarrow}$. Zero of down range dimension shifted to 10000.

(b) The marginal posterior distribution of $x_3^{\perp}$.

Figure 5.16: The marginal posterior distributions for the states associated with dominant scatterer 3 obtained with the PMMH sampler.

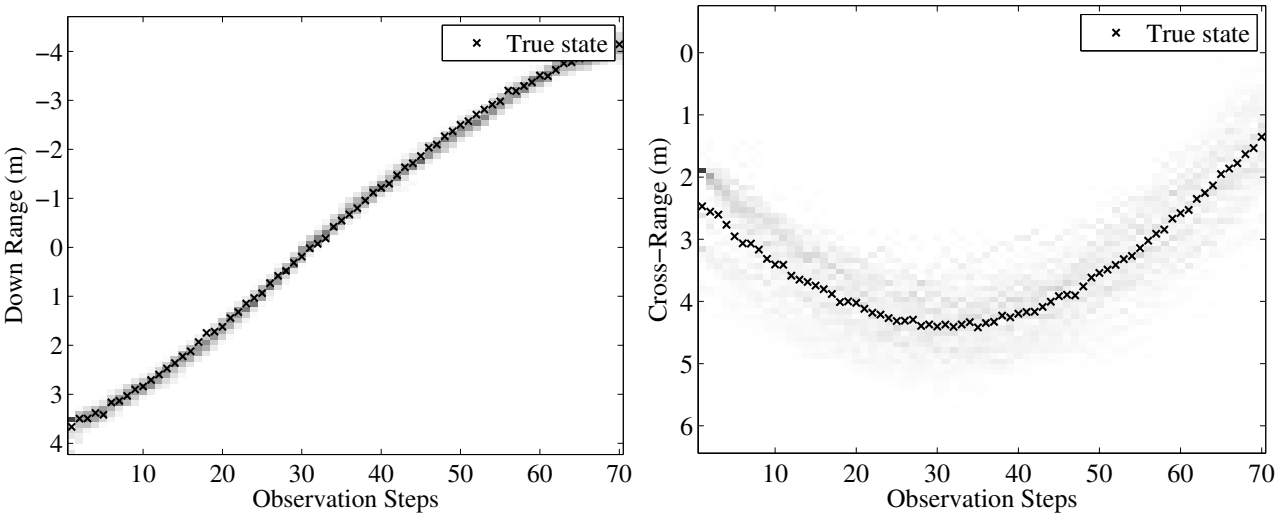

(a) The marginal posterior distribution of $x_4^{\rightarrow}$. Zero of down range dimension shifted to 10000.

(b) The marginal posterior distribution of $x_4^{\perp}$.

Figure 5.17: The marginal posterior distributions for the states associated with dominant scatterer 4 obtained with the PMMH sampler.

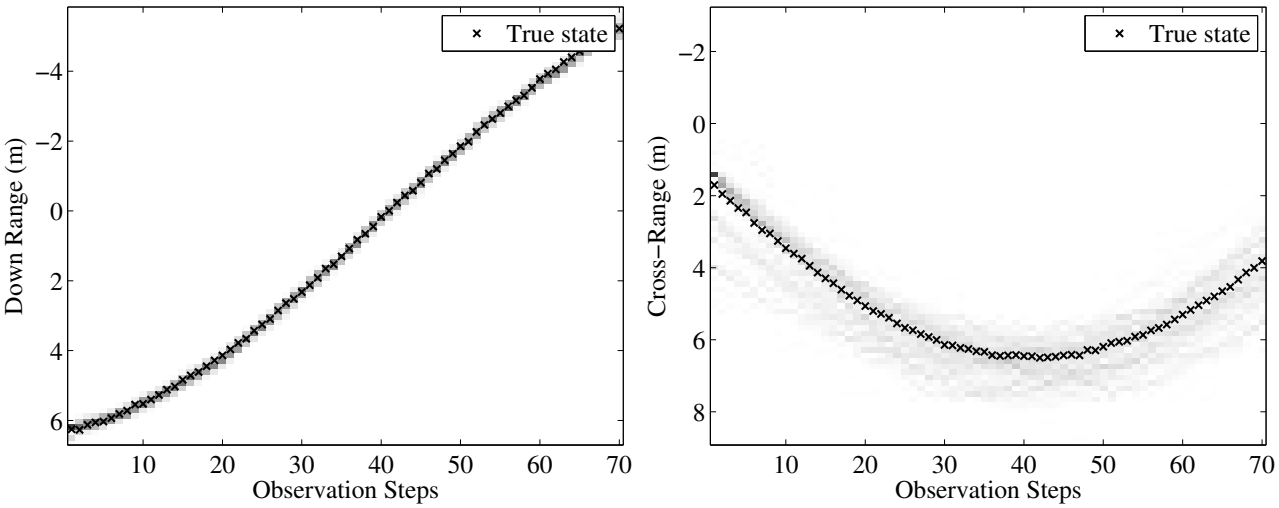

(a) The marginal posterior distribution of $x_5^{\rightarrow}$. Zero of down range dimension shifted to 10000.

(b) The marginal posterior distribution of $x_5^{\perp}$.

Figure 5.18: The marginal posterior distributions for the states associated with dominant scatterer 5 obtained with the PMMH sampler.

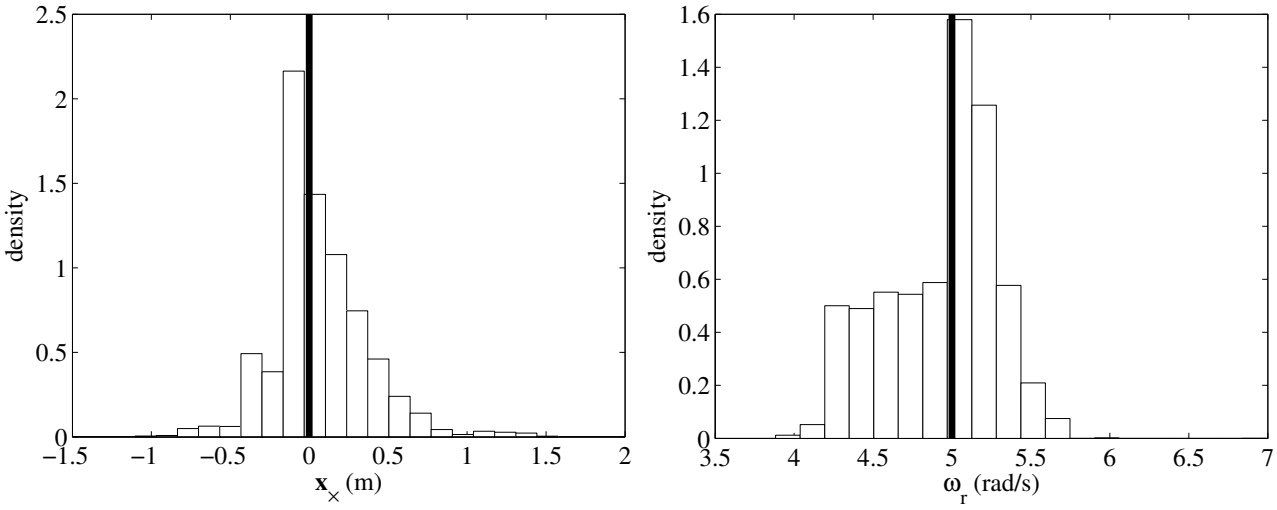

(a) The marginal posterior distribution of θ_1. Zero of down range dimension shifted to 10000.

(b) The marginal posterior distribution of θ_2.

Figure 5.19: The marginal posterior distributions for the static parameters of Model I obtained with the PMMH sampler. The true value for each parameter is indicated by a solid line.

The PMMH sampler successfully estimated the static parameters and state variables associated with model I. The variance of the marginal posterior distributions for the cross-range states are considerably larger than for the down range states. This is due to the majority of information in the range observation pertaining to the down range states. The information pertaining to the cross-range states is based on the motion of the target. This is highlighted by increasing the angular velocity. The simulation was performed again with the only target parameters changing being the angular velocities. The target's angular velocity was increased from 5 to 10 rad/s and the maximum target's angular velocity was increased from 6 to 15 rad/s. The corresponding dominant scatterer trajectories are illustrated in Figure 5.20.

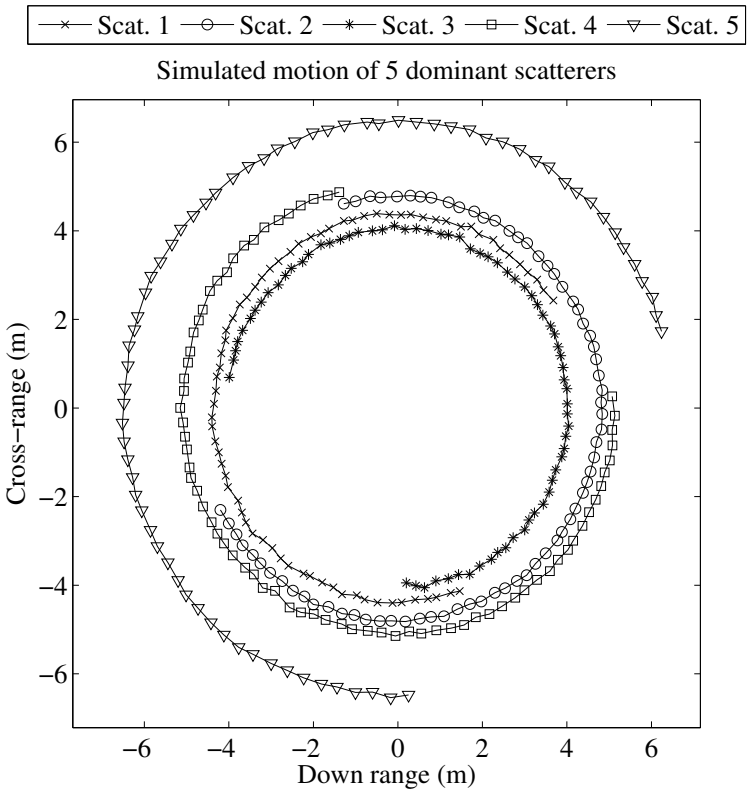

Figure 5.20: Trajectory of a random target consisting of 5 dominant scatterers. The direction of rotation of the target is anti-clockwise. Zero reference point of axes shifted to [10000,0].

The magnitude of the HRR profiles and extracted ranges for the dominant scatterers are illustrated in Figure 5.21. The inferred marginal posterior distributions for the state variables and static parameters are illustrated in Figures 5.22 to 5.26 and Figure 5.27 respectively.

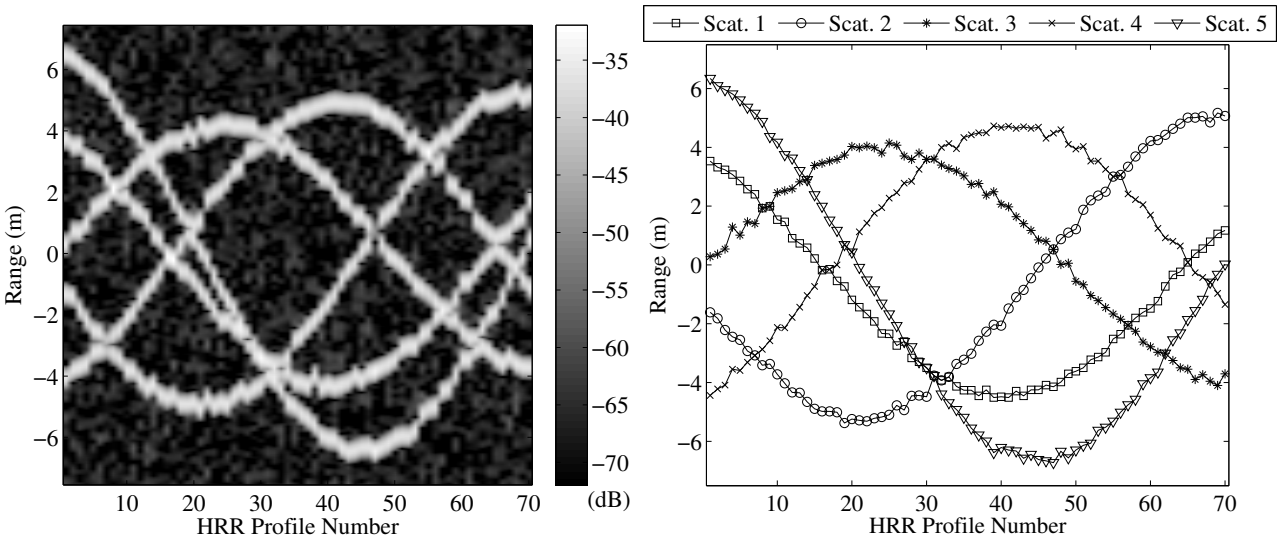

(a) HRR profiles generated by the radar simulator based on the radar parameters in Table 5.2. Zero point of range axis shifted to 10000.

(b) The range values extracted from the HRR profiles for each dominant scatterer. Zero point of range axis shifted to 10000.

Figure 5.21: The magnitude of the HRR profiles and extracted range values for a target with an angular velocity of 10 rad/s.

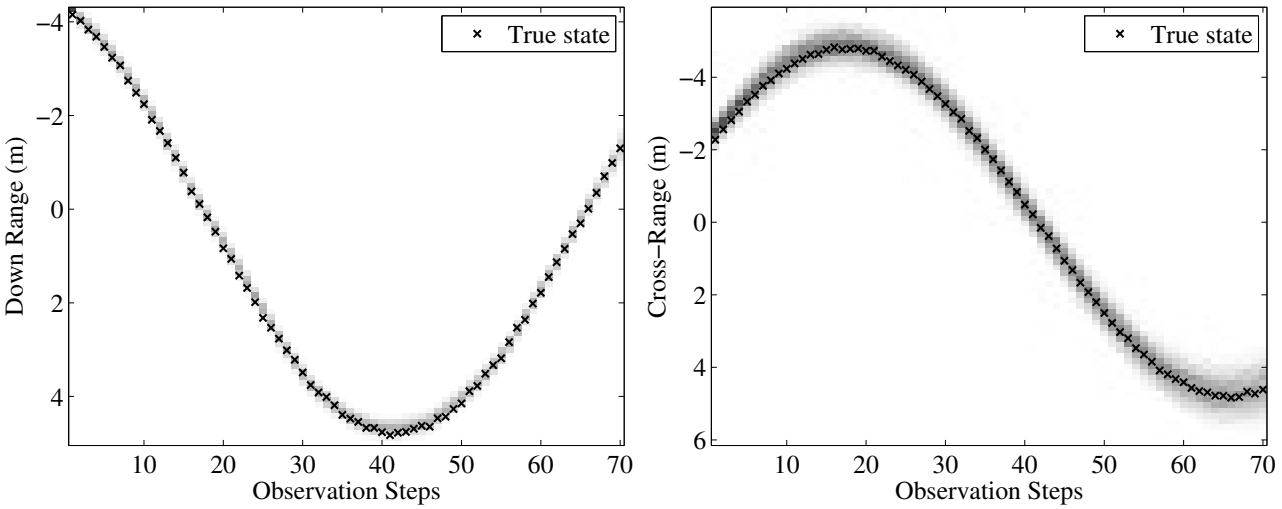

(a) The marginal posterior distribution of $x_1^{\rightarrow}$. Zero of down range dimension shifted to 10000.

(b) The marginal posterior distribution of $x_1^{\perp}$.

Figure 5.22: The marginal posterior distributions for the states associated with dominant scatterer 1 obtained with the PMMH sampler.

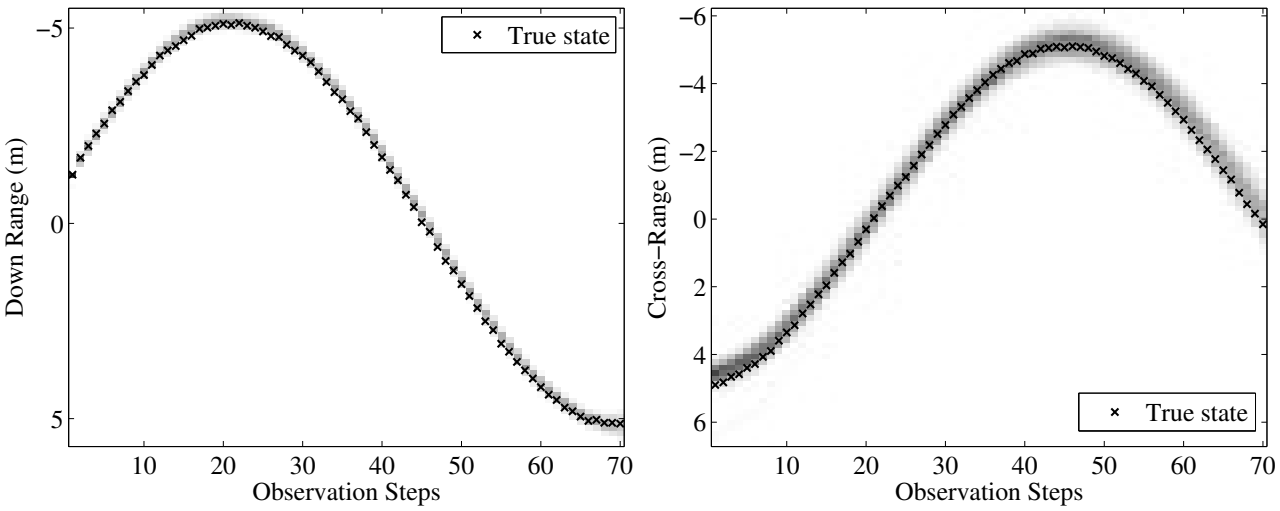

(a) The marginal posterior distribution of $x_2^{\rightarrow}$. Zero of down range dimension shifted to 10000.

(b) The marginal posterior distribution of $x_2^{\perp}$.

Figure 5.23: The marginal posterior distributions for the states associated with dominant scatterer 2 obtained with the PMMH sampler.

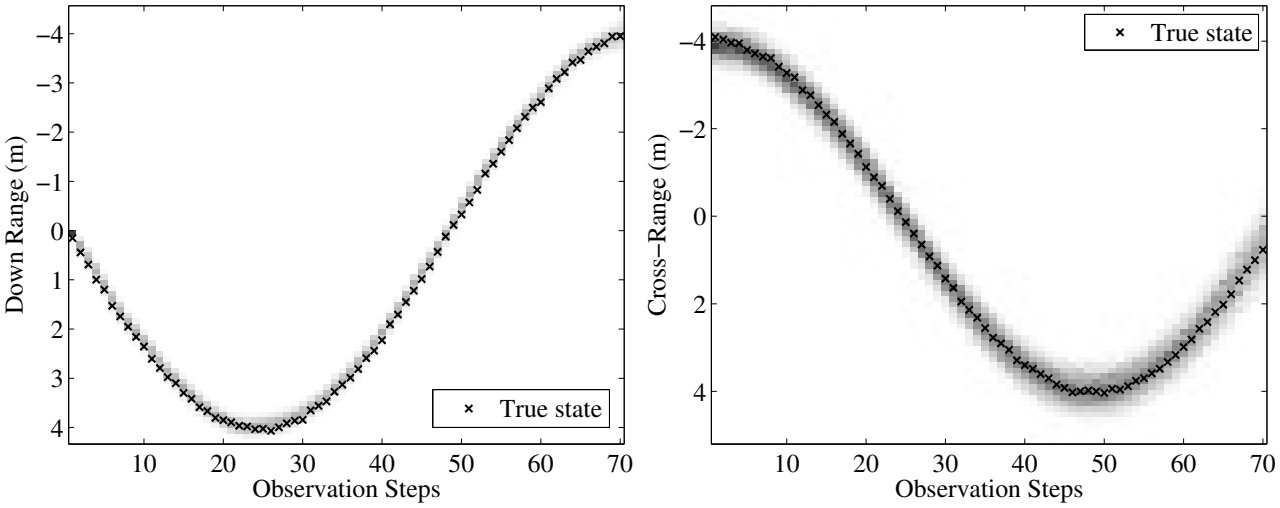

(a) The marginal posterior distribution of $x_3^{\rightarrow}$. Zero of down range dimension shifted to 10000.

(b) The marginal posterior distribution of $x_3^{\perp}$.

Figure 5.24: The marginal posterior distributions for the states associated with dominant scatterer 3 obtained with the PMMH sampler.

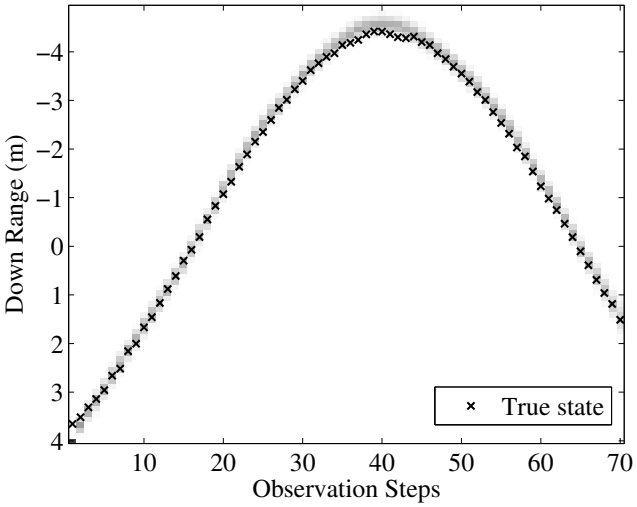

(a) The marginal posterior distribution of $x_4^{\rightarrow}$. Zero of down range dimension shifted to 10000.

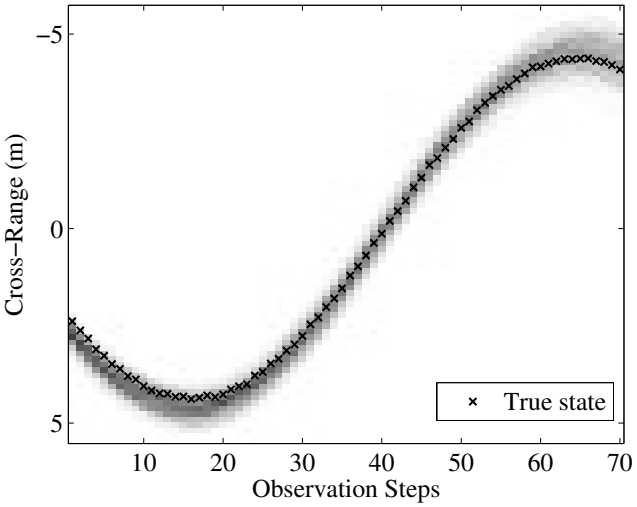

(b) The marginal posterior distribution of $x_4^{\perp}$.

Figure 5.25: The marginal posterior distributions for the states associated with dominant scatterer 4 obtained with the PMMH sampler.

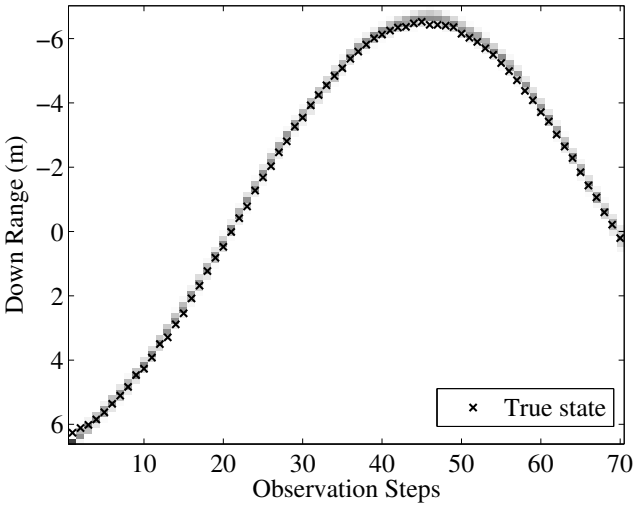

(a) The marginal posterior distribution of $x_5^{\rightarrow}$. Zero of down range dimension shifted to 10000.

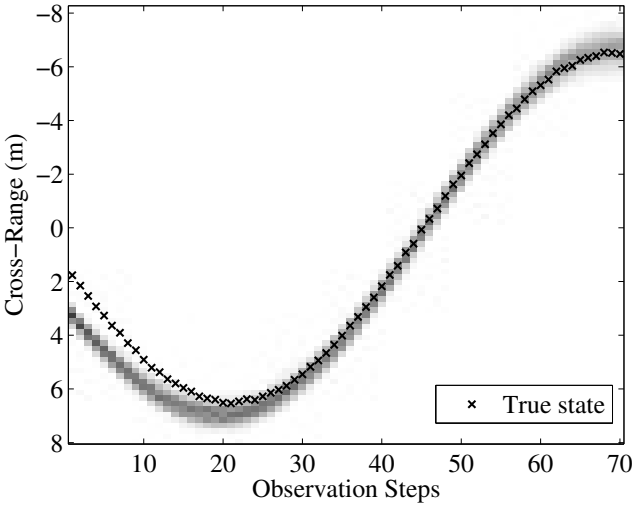

(b) The marginal posterior distribution of $x_5^{\perp}$.

Figure 5.26: The marginal posterior distributions for the states associated with dominant scatterer 5 obtained with the PMMH sampler.

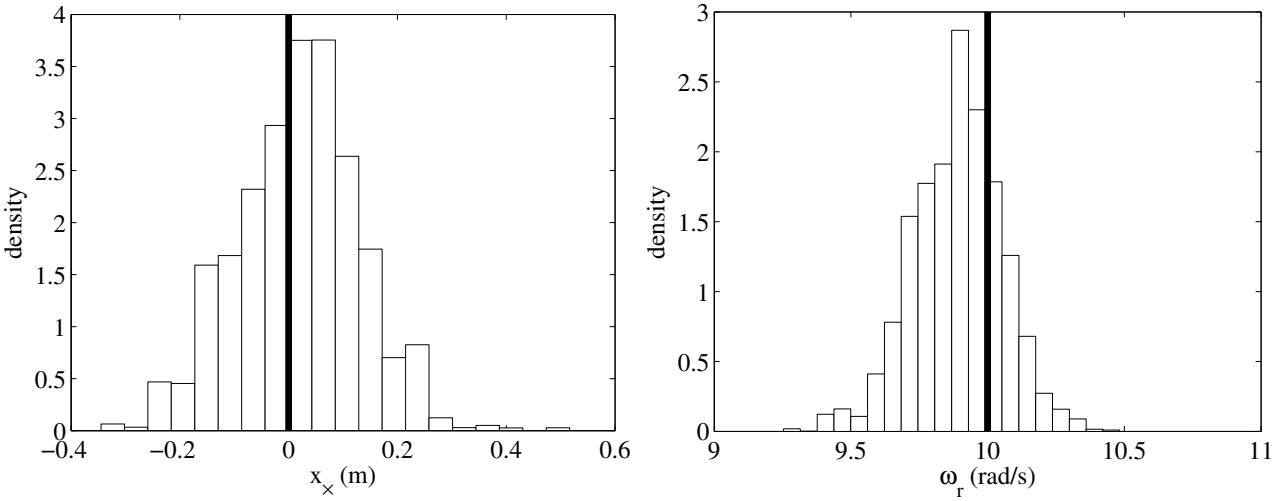

(a) The marginal posterior distribution of θ_1. Zero of down range dimension shifted to 10000.

(b) The marginal posterior distribution of θ_2.

Figure 5.27: The marginal posterior distributions for the static parameters of Model I obtained with the PMMH sampler. The true value for each parameter is indicated by a solid line.

Comparing the marginal posterior distributions for the states corresponding to the cross-range dimensions in Figures 5.14 to 5.18 and Figures 5.22 to 5.26 highlights the difference in the variance of the distributions. A target undergoing a higher angular velocity contains more motion information resulting in a lower variance in the marginal posterior distribution for the states corresponding to the cross-range dimension. It also results in more accurate estimates for the static parameters as noted when comparing Figures 5.19 and Figure 5.27.

5.3 MODEL II

5.3.1 Observation Extraction

Model II is aligned to a more realistic target undergoing substantially less angular velocity in the same time frame as in Model I. A random target consisting of 6 dominant scatterers based upon Model II was created. This value of dominant scatterers was selected to demonstrate the algorithms ability to handle dominant scatterers located at different radii and exhibiting different delta phase observations. The influence of varying this parameter was investigated in Section 5.3.4. The trajectory of the dominant scatterers is presented in Figure 5.28.

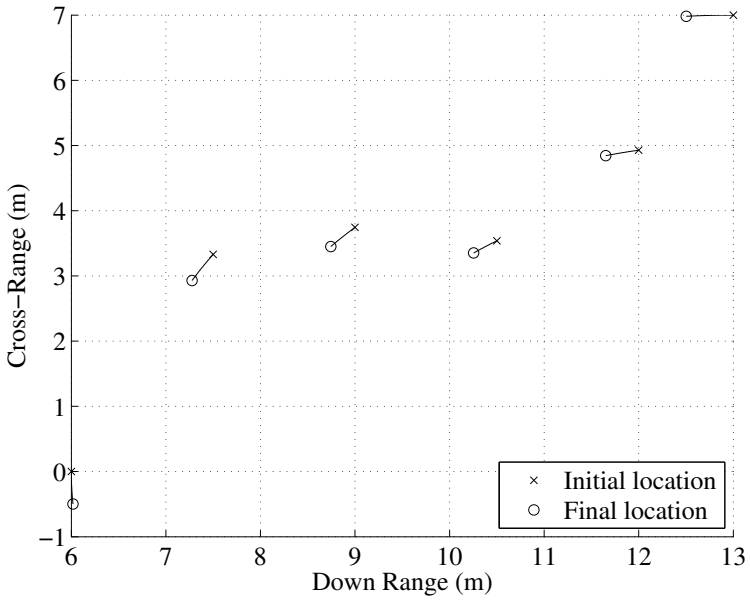

Figure 5.28: Trajectory of a random target consisting of 6 dominant scatterers. Zero reference point of axes shifted to [10000,0].

The parameters of the target and its motion are listed in Table 5.4. The targets motion was selected to coincide with a standard rate two turn of an aircraft. The motion model variance was selected to ensure that the motion of the target from one time step to the next, did not result in delta phase wrapping. The radar parameters utilised in the Model I experiments, listed in Table 5.2, remained the same for the Model II experiments.

Table 5.4: Defining parameters of the random target illustrated by Figure 5.28.

Parameter	Parameter Value
Number of dominant scatterers	6
Angular velocity (ω_r)	0.1 rad/s
Centroid of rotation co-ordinates($[x_\times, 0]$)	$[10013, 0]$ m
Motion model variances ($[\sigma_q^2, \sigma_p^2]$)	$[1 \times 10^{-3}, 1 \times 10^{-9}]$ m
Total time elapsed	0.64 s
Time difference between points (Δt)	6.4 ms

The magnitude of the HRR profiles observed from the target illustrated by Figure 5.28 are graphically

presented in Figure 5.29.

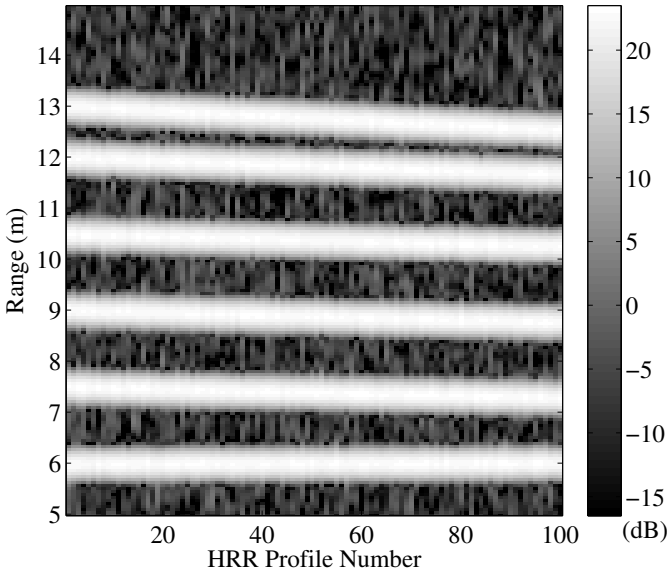

Figure 5.29: HRR profiles generated by the radar simulator based on the radar parameters in Table 5.2. Zero point of range axis shifted to 10000.

The observation vector for Model II consists of the range and the delta phase for each of the dominant scatterers. The extracted ranges from the HRR profiles are illustrated in Figure 5.30. The range noise standard deviation associated with the Gaussian random variable in Equation 4.13 was measured as 3.2 mm from simulation.

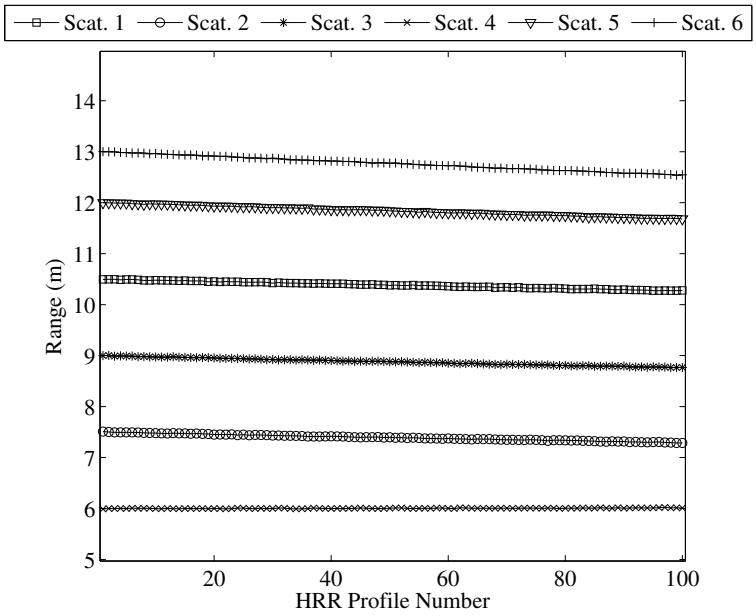

Figure 5.30: The range values extracted from the HRR profiles in Figure 5.29 for each dominant scatterer. Zero point of range axis shifted to 10000.

The extracted delta phase of each dominant scatterer is presented in Figures 5.31 to 5.33.

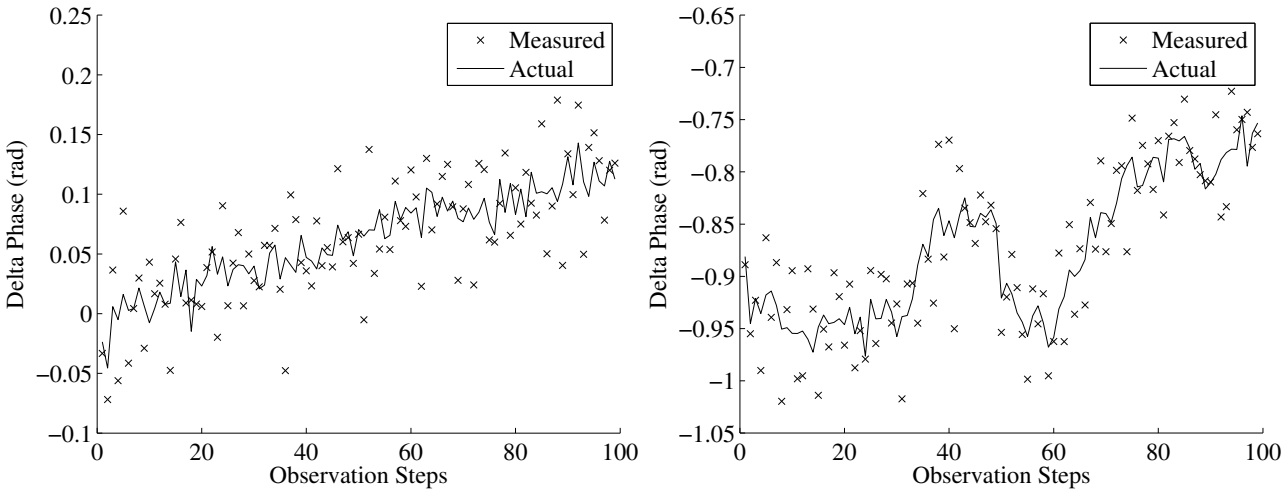

(a) Measured and true delta phase for dominant scatterer 1.

(b) Measured and true delta phase for dominant scatterer 2.

Figure 5.31: The delta phase observations extracted from the complex HRR profiles for the dominant scatterers located on the target illustrated by Figure 5.28.

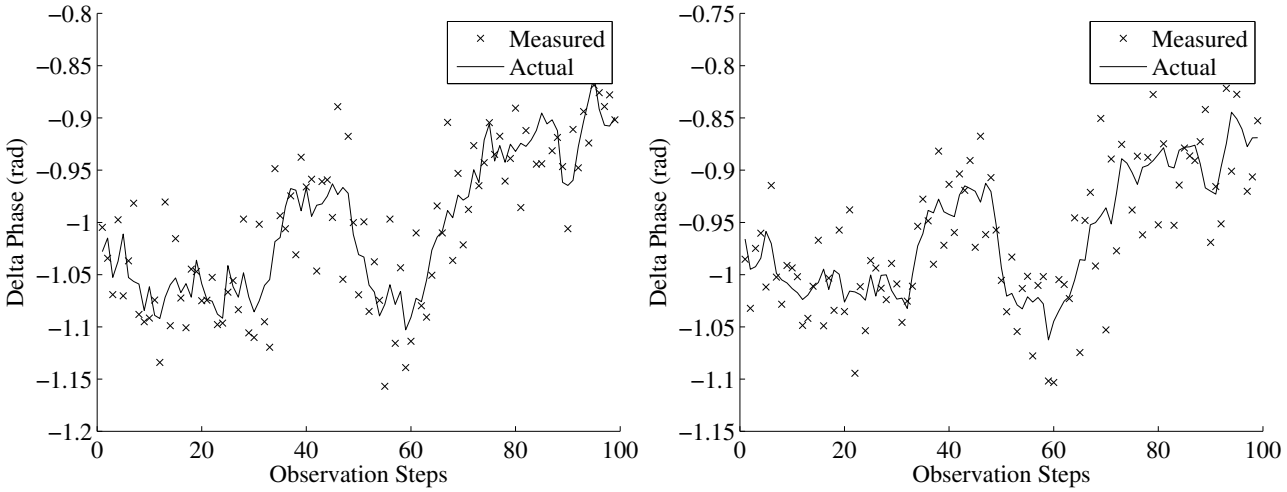

(a) Measured and true delta phase for dominant scatterer 3.

(b) Measured and true delta phase for dominant scatterer 4.

Figure 5.32: The delta phase observations extracted from the complex HRR profiles for the dominant scatterers located on the target illustrated by Figure 5.28.

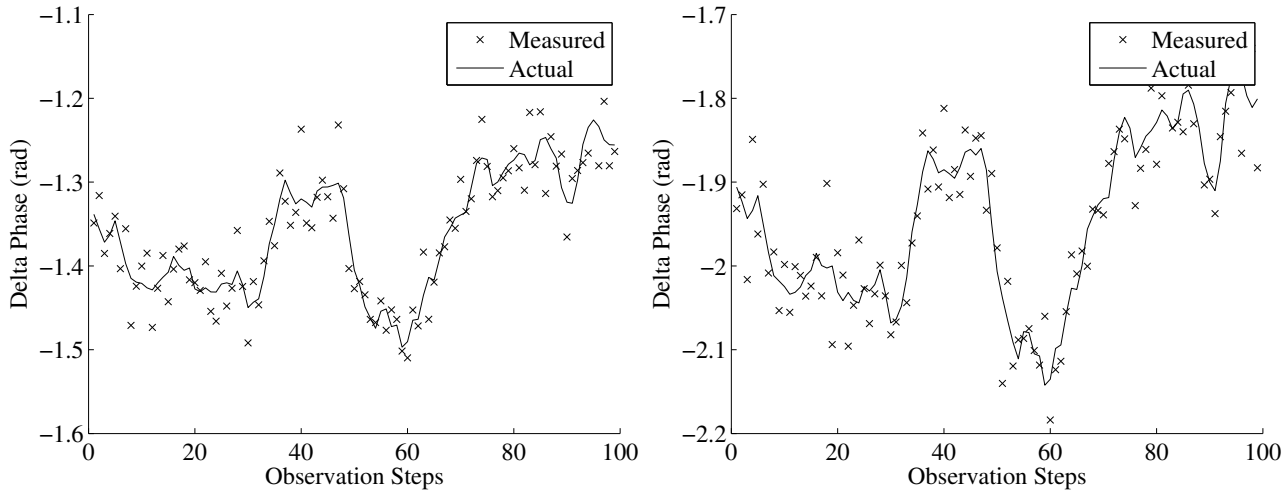

(a) Measured and true delta phase for dominant scatterer 5.

(b) Measured and true delta phase for dominant scatterer 6.

Figure 5.33: The delta phase observations extracted from the complex HRR profiles for the dominant scatterers located on the target illustrated by Figure 5.28.

It was assumed that dominant scatterers do not overlap in range bins since this would result in severe interference in the delta phase measurements. However, this could be countered in the future by increasing the noise variance of the phase measurements when interference is detected, or through the implementation of a multiple observation model PF [63].

The delta phase noise concentration parameter associated with the Von Mises distributed random variable in Equation 4.14 was measured as 769.23 from simulation.

5.3.2 Particle Initialisation

Initialisation of the particles is a crucial step in the implementation of any PF. Initialising the PF based only on the first HRR profile received as was done according to Equation 5.1 for the range only measurement model, resulted in the particles being too sparsely located in the state space and hence resulting in severe PF degeneracy. A smart initialisation scheme was devised based on the observations extracted from the first two HRR profiles.

It is assumed that the target is non-cooperative. Hence, the prior information known about the target is limited to the maximum extent of the target and the assumption that the motion model accurately describes the motion of the target. Observing two HRR profiles results in two range measurements and a delta phase measurement. It was proposed that these observations could aid in obtaining a more accurate particle initialisation. The mapping between the state space and the observation space for Model II is represented by the observation generation functions in Equations 4.13 and 4.14. However, this is not a unique mapping and any observation, when mapped to the state space, can result in many different locations in the state space. This is further influenced by the noise associated with the mapping. The aim is to populate particles in all the regions of the state space which could result in the observations received. The first step is to perturb the observations by the noise which is associated with the observation generation functions. This is done to move the observations possibly towards the true location of the observations without the influence of noise as illustrated in Figure 5.34.

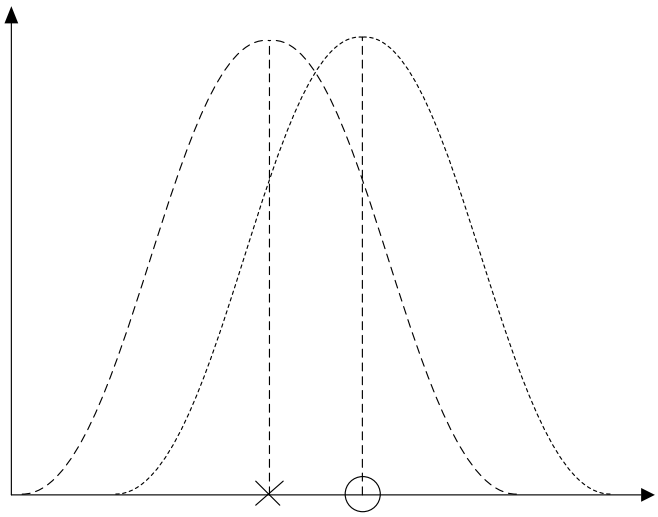

Figure 5.34: Example of sampling from the observation distribution. In this illustration the cross represents the true unknown observation, the circle represents the observation obtained. The solid line distribution represents the true unknown distribution and the dotted line distribution represents the distribution sampled from to obtain a unique observation associated with a specific particle.

This method guarantees that it is possible to sample the true observation when the observation distribution is symmetrical. After this step it is assumed that the noise terms in the observation generation functions are removed, resulting in a noiseless mapping between the state space and observation space,

$$\begin{aligned} R_{c,k} &= \sqrt{(r_{c,k}\cos(\theta_{c,k}) + x_{\times}^{\rightarrow})^2 + (r_{c,k}\sin(\theta_{c,k}))^2} \\ \Delta\phi_{c,k} &= \frac{4\pi\Delta R_{c,k}}{\lambda}, \end{aligned} \tag{5.2}$$

where $\Delta R_{c,k} = R_{c,k} - R_{c,k-1}$. However, these relationships do not describe a complete mapping between the observation space and every dimension of the state space. Comparing the relationships to the state vector in Equation 4.10, it is found that there is no direct relationship between the observation space and the angular velocity dimension in the state space. A relationship was derived to relate the observations to the angular velocity dimension in the state space. Firstly, the delta phase observation is related to the difference in range for each scatterer through

$$\Delta R_c = \frac{\Delta\phi_c\lambda}{4\pi}. \tag{5.3}$$

The difference in range is related to the radial velocity of the scatterer through

$$v_{r,c} = \frac{\Delta R_c}{\Delta t}. \tag{5.4}$$

The radial velocity is related to the angular velocity of the overall target and the down range and cross-range location of the specific scatterer through

$$\begin{aligned} v_{r,c} &= v\cos\theta_{a,c} \\ v_{r,c} &= \omega r_c \cos\theta_{a,c} \\ v_{r,c} &\approx \omega\sqrt{(x_c^{\rightarrow} - x_{\times})^2 + {x_c^{\perp}}^2}\cos\left(\frac{\pi}{2} + \tan^{-1}\left(\frac{x_c^{\perp}}{x_c^{\rightarrow} - x_{\times}}\right)\right), \end{aligned} \tag{5.5}$$

where $\theta_{a,c}$ represents the angle between the radar and the velocity vector of scatterer c and is not to be confused with the angles in the state space. The further away a dominant scatterer is from the centroid of rotation, the larger the distance that the scatterer moves given the same angular velocity, as illustrated in Figure 5.35. By making the angular velocity the subject of the formula in Equation

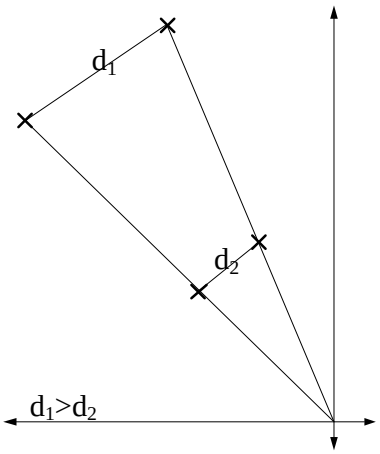

Figure 5.35: Illustration of the difference in distance travelled by dominant scatterers located at different distances from the centroid of rotation. When the rotation rate is constant, the distance travelled is always the largest for a dominant scatterer located the furtherest away from the centroid of rotation.

5.5 and substituting the maximum cross-range location for any scatterer and the range observation as the down range location results in a minimum possible angular velocity for the target

$$\omega_{\min,c} = \frac{v_{r,c}}{\sqrt{(R_c - x_{\times})^2 + {x_{\max}^{\perp}}^2}\cos\left(\frac{\pi}{2} + \tan^{-1}\left(\frac{x_{\max}^{\perp}}{R_c - x_{\times}}\right)\right)}. \tag{5.6}$$

Finding the maximum of the minimum angular velocities determined for each dominant scatterer results in the minimum angular velocity of the target for the specific particle due to the rigid body

assumption,

$$\omega_{\min} = \max_{c} \omega_{\min,c}. \tag{5.7}$$

The relationship between the range observation and the down range and cross-range locations of each scatterer is given by

$$R_c = \sqrt{x_c^{\rightarrow 2} + x_c^{\perp 2}}. \tag{5.8}$$

Solving for the down range location and substituting into Equation 5.5 results in

$$v_{r,c} = \omega \sqrt{\left(\sqrt{R_c^2 - x_c^{\perp 2}} - x_\times\right)^2 + x_c^{\perp 2}} \cos\left(\frac{\pi}{2} + \tan^{-1}\left(\frac{x_c^{\perp}}{\sqrt{R_c^2 - x_c^{\perp 2}} - x_\times}\right)\right). \tag{5.9}$$

After determining the minimum angular velocity for the particle, the angular velocity state is initialised according to

$$\omega \sim U(\omega_{\min}, \omega_{\max}), \tag{5.10}$$

where $\omega_{\max}$ is the maximum angular velocity fixed in simulation. The sampled angular velocity is then substituted into Equation 5.9. With the knowledge of the radial velocity and range for each scatterer, the only unknown variable in the equation is the cross-range location. Once the cross-range location was inferred for each scatterer, the value was substituted into Equation 5.8 to obtain a corresponding down range location. The down range and cross-range locations for each scatterer were then converted into the polar domain. This process was repeated for the initialisation of each particle.

5.3.3 Unscented Particle Filter Approach

The UPF has been shown to perform well in applications in which the likelihood density is peaked relative to the state transition density as illustrated in Figure 5.36.

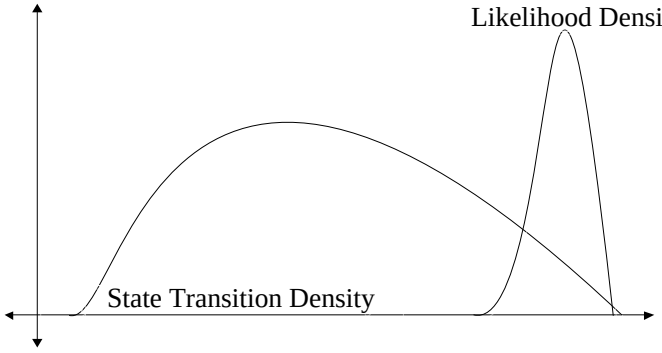

Figure 5.36: Illustration of the likelihood density in terms of the state space and state transition density.

This is due to the fact that the proposal distribution takes the latest observation into account. This allows the filter to move the particles into areas which result in high likelihoods. However, the problem faced in this specific application, was that the state transition density, based on the motion model, was peaked relative to the prior distribution. This resulted in the degeneration of the estimates obtained from the UPF. Unlike the BPF, the weight for each particle in the UPF is dependent on the state transition density, as noted by Equation 3.23. The mismatch between the prior distribution and state transition density resulted in the weights obtaining a value of zero due to particles being moved to locations in the state space where the state transition density approaches zero. The state transition density for Model II is relatively peaked to prevent ambiguities from occurring in the delta phase measurement.

5.3.4 Bootstrap Particle Filter Approach

The results obtained by applying the BPF to the target illustrated by Figure 5.28 were plagued by PF degeneracy. The degeneracy resulted in a poor representation of the underlying filtering distribution. The filter degeneracy is highlighted by the ESS curve in Figure 5.37. The PF was initialised with 10000 particles, for this particular run, at the second time step, only an equivalent of 7.24 particles represented regions of interest in the filtering distribution. Resampling superficially increases the ESS as several particles are duplicated many times. However, this cannot improve the approximation of the filtering distribution. The degeneracy is linked to a lack of noise in the observation space. This results in a highly peaked likelihood density. Increasing the number of particles used to represent the filtering distribution did not improve the results. A suboptimal method to reduce the degeneracy was

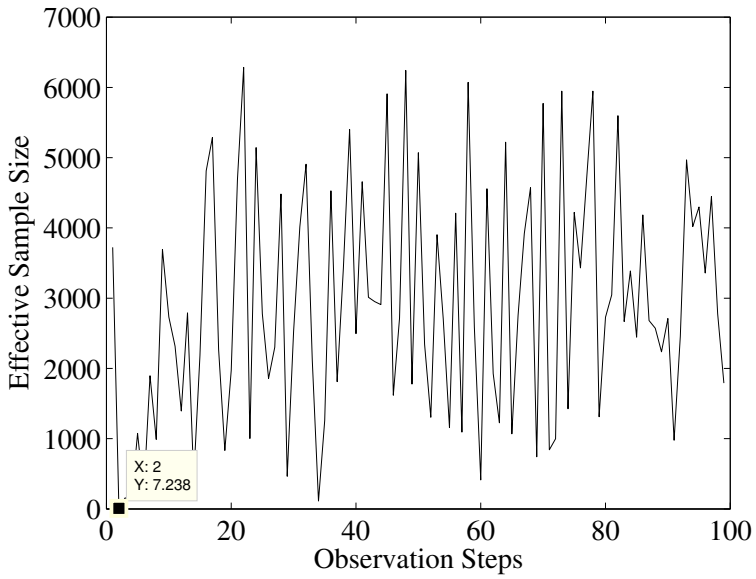

Figure 5.37: ESS curve obtained when the BPF was applied to inferring the states associated with the target in Figure 5.28.

implemented. This method consisted of artificially increasing the variance of the observations in the state space model. The BPF was run with a 10 fold increase in both the variance for the delta phase and range observations. This resulted in a boost in the ESS and an approximated filtering distribution in the vicinity of the true states. Firstly, validation of utilising 10000 particles was performed by varying the number of particles and taking note of the accuracy of the angular velocity state. The root mean-square-error (RMSE) was used as a measure of accuracy. The RMSE measures the difference between values predicted by an estimator and the true values as given by,

$$\text{RMSE} = \sqrt{\frac{1}{n}\sum_{i=1}^{n}\left(\hat{X}_i - X_i\right)^2}, \tag{5.11}$$

where X_i represents the true value, $\hat{X}_i$ represents the estimated value, which corresponds to the mean of the approximate filtering distribution in this application, and n represents the number of samples. The results, with the maximum initial target velocity arbitrarily selected as 0.2 rad/s, are illustrated in Figure 5.38.

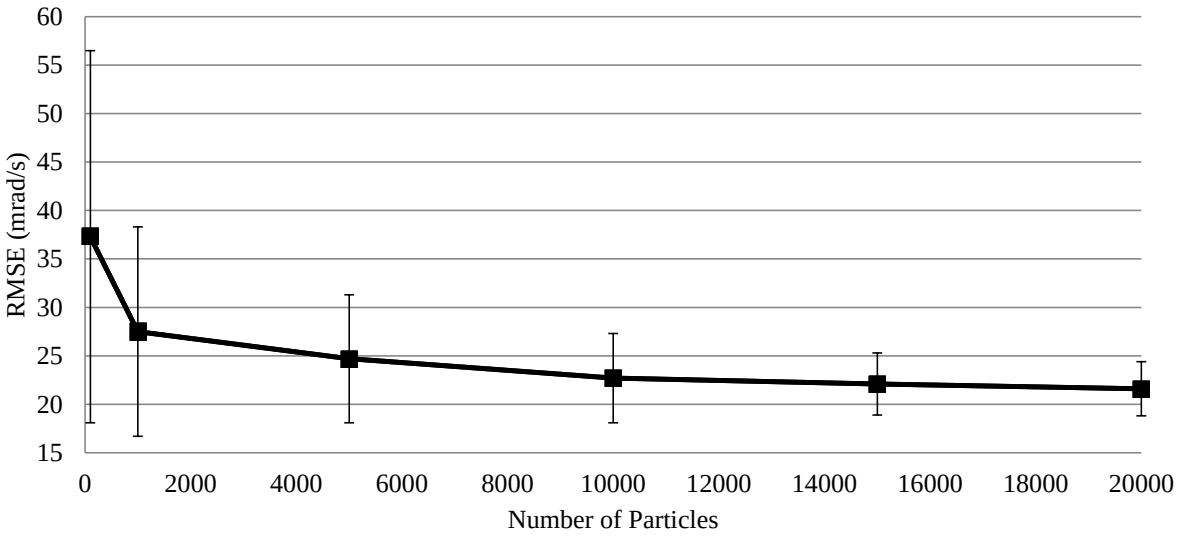

Figure 5.38: Relationship between the RMSE and the number of particles used to represent the filtering distribution in the BPF. The error bars represent the standard deviation of the RMSE over 50 simulations runs.

Figure 5.38 illustrates that utilising more than 10000 particles did not result in a significant gain in accuracy and only increased the computational complexity of the algorithm. The relationship between PF degeneracy and the number of particles is highlighted by the error bars in Figure 5.38. The RMSE is dependent on the square of the difference of the true value and the mean of the distribution represented by the particles in the PF. The square differences are averaged together for all time steps when determining the RMSE, as highlighted by Equation 5.11. A uniform distribution is used to initialise the angular velocity state. The mean of a uniform distribution is the value located at the midpoint of the distribution. Utilising a small number of particles to represent the uniform distribution at the first time step is insufficient, such as utilising 100 particles which corresponds to the first data point in Figure 5.38. There are not enough particles available to represent the entire initialisation region. On certain runs all the particles could be initialised close to the true value of the first time step, and stay in the vicinity of the true value for all further time steps. In this case a very low RMSE value is obtained. At the other extreme, all the particles could be initialised far away from the true value at the first time step and are unable to converge to the true value, resulting in a very high RMSE value. Utilising a large number of particles to represent the distribution in the PF allows for the particles to sufficiently approximate the initial uniform distribution. The mean of the distribution represented by the particles at the first time step thus corresponds to the midpoint of the uniform distribution. This value may still be relatively far away from the true value of the state at the first time

step. As time proceeds the particles tend towards the true value and the mean gets closer to the true value. However, the difference between the mean and true state at the first time step, which is always large, is included in the averaging across all time steps, resulting in it being impossible to obtain a very low RMSE value. Since the particles always converge to the true value, it is also not possible to obtain a very high RMSE value either. The final result is a more stable RMSE value when a larger amount of particles are used to represent the distribution. These results did not vary significantly with an increased number of simulation runs as illustrated by the results in Figure 5.39.

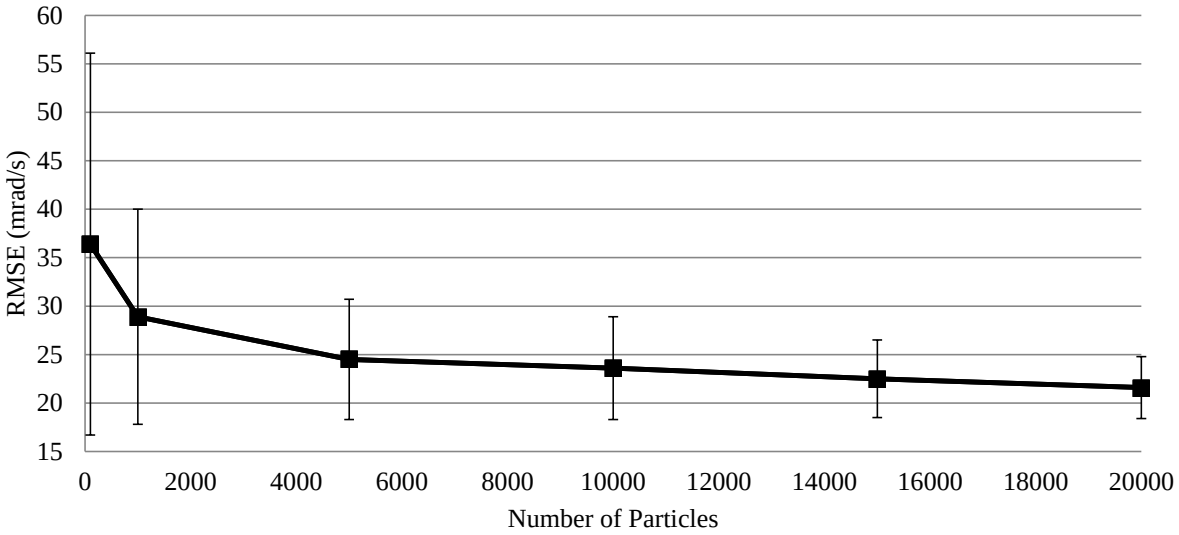

Figure 5.39: Relationship between the RMSE and the number of particles used to represent the filtering distribution in the BPF. The error bars represent the standard deviation of the RMSE over 200 simulations runs.

The marginal filtering distributions converted into the down range and cross-range dimensions and ESS are given in Figures 5.40 to 5.46 below for a target with a maximum initial target velocity of 0.11 rad/s. The selection of this value translates into an application where the target is considered to be initially rotating at an unknown varying rate between zero and a rate two turn of an aircraft. The effect of increasing the variance of the observations in the state space model is clearly evident in Figures 5.40 (a) and 5.43 (b). The support of the approximate distribution is not centered about the true states. Without the increase in variance, these particles would obtain a much lower weighting and could result in filter degeneration.

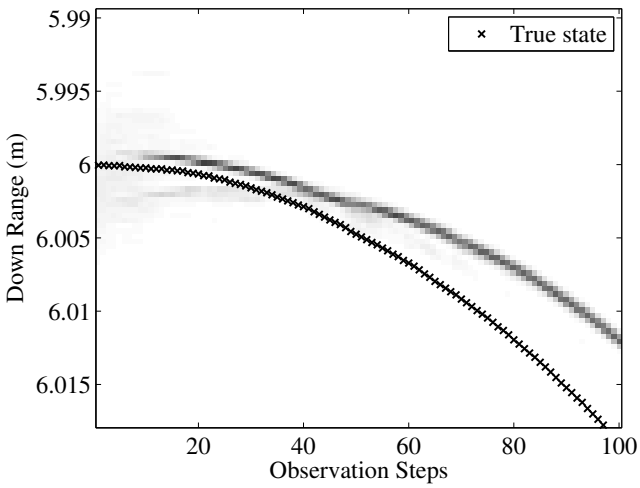

(a) The marginal filtering distribution of $x_1^{\rightarrow}$. Zero of down range dimension shifted to 10000.

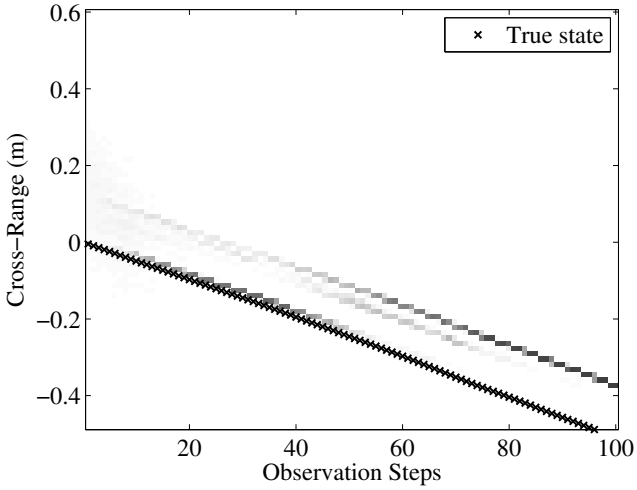

(b) The marginal filtering distribution of $x_1^{\perp}$.

Figure 5.40: Marginal filtering distributions for the states associated with dominant scatterer 1 through the BPF.

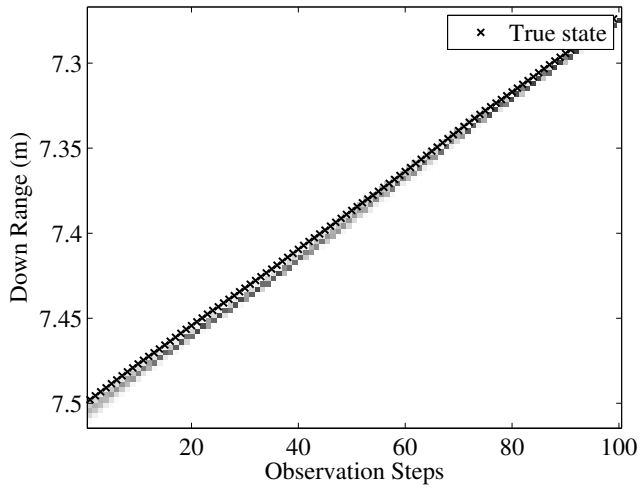

(a) The marginal filtering distribution of $x_2^{\rightarrow}$. Zero of down range dimension shifted to 10000.

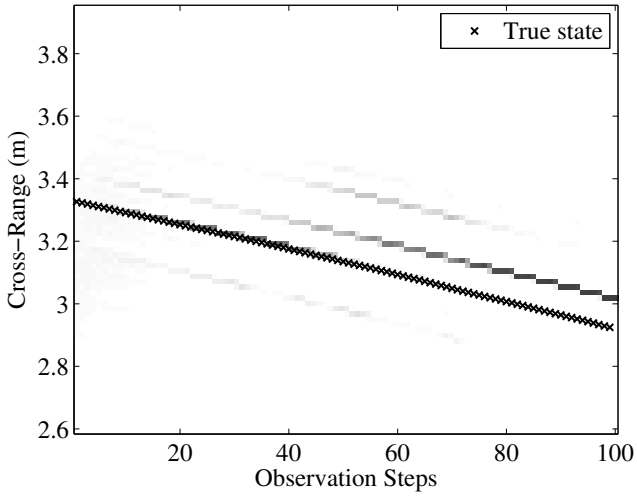

(b) The marginal filtering distribution of $x_2^{\perp}$.

Figure 5.41: Marginal filtering distributions for the states associated with dominant scatterer 2 through the BPF.

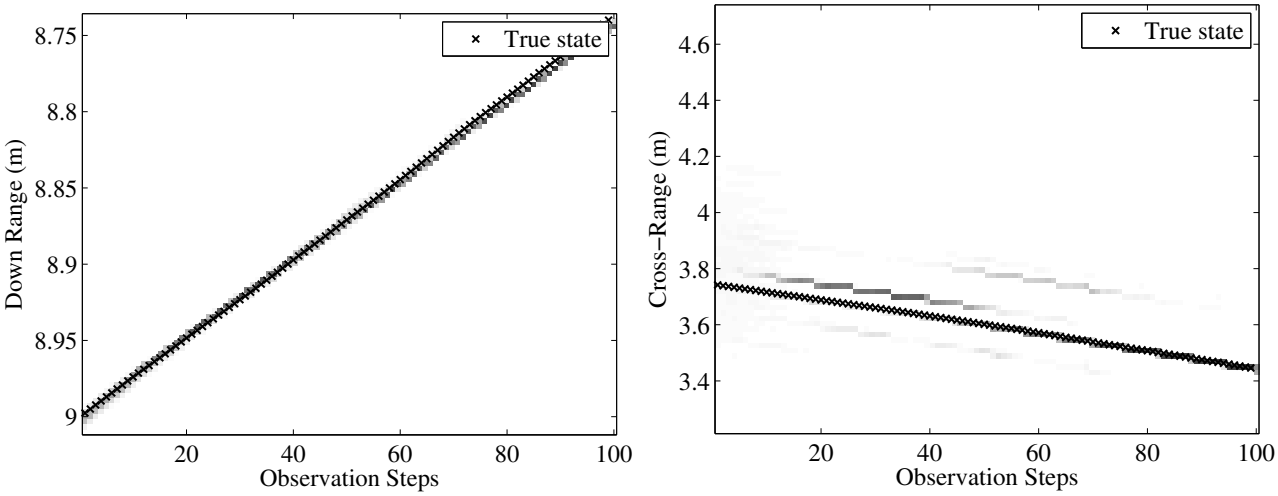

(a) The marginal filtering distribution of $x_3^{\rightarrow}$. Zero of down range dimension shifted to 10000.

(b) The marginal filtering distribution of $x_3^{\perp}$.

Figure 5.42: Marginal filtering distributions for the states associated with dominant scatterer 3 through the BPF.

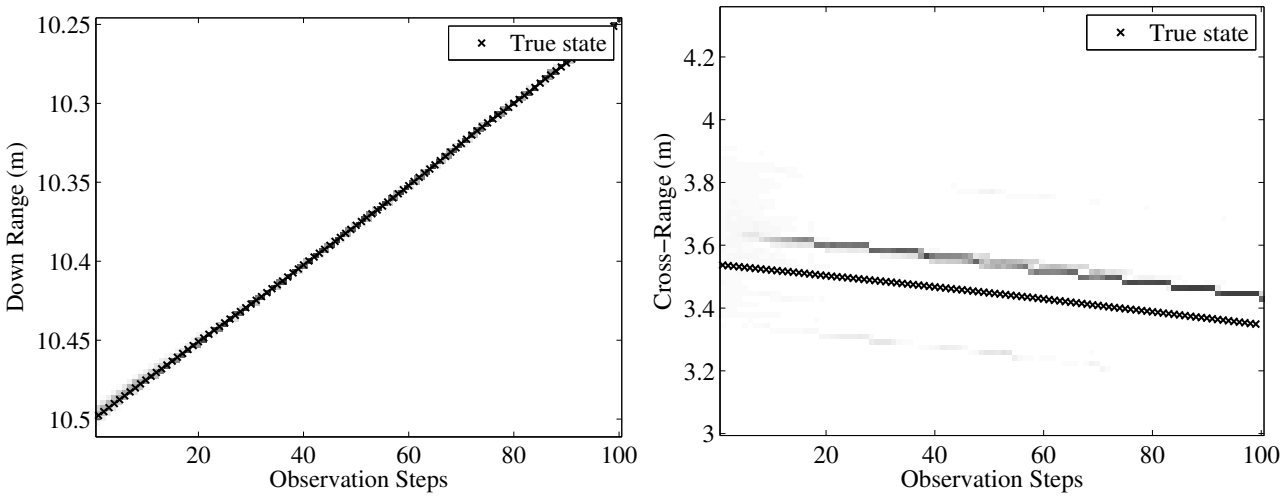

(a) The marginal filtering distribution of $x_4^{\rightarrow}$. Zero of down range dimension shifted to 10000.

(b) The marginal filtering distribution of $x_4^{\perp}$.

Figure 5.43: Marginal filtering distributions for the states associated with dominant scatterer 4 through the BPF.

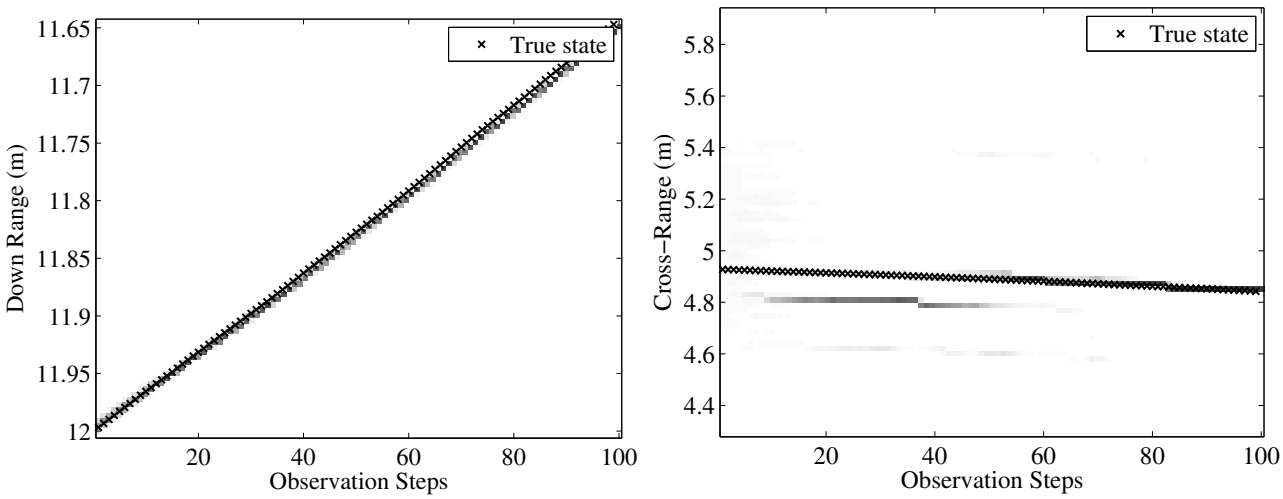

(a) The marginal filtering distribution of $x_5^{\rightarrow}$. Zero of down range dimension shifted to 10000.

(b) The marginal filtering distribution of $x_5^{\perp}$.

Figure 5.44: Marginal filtering distributions for the states associated with dominant scatterer 5 through the BPF.

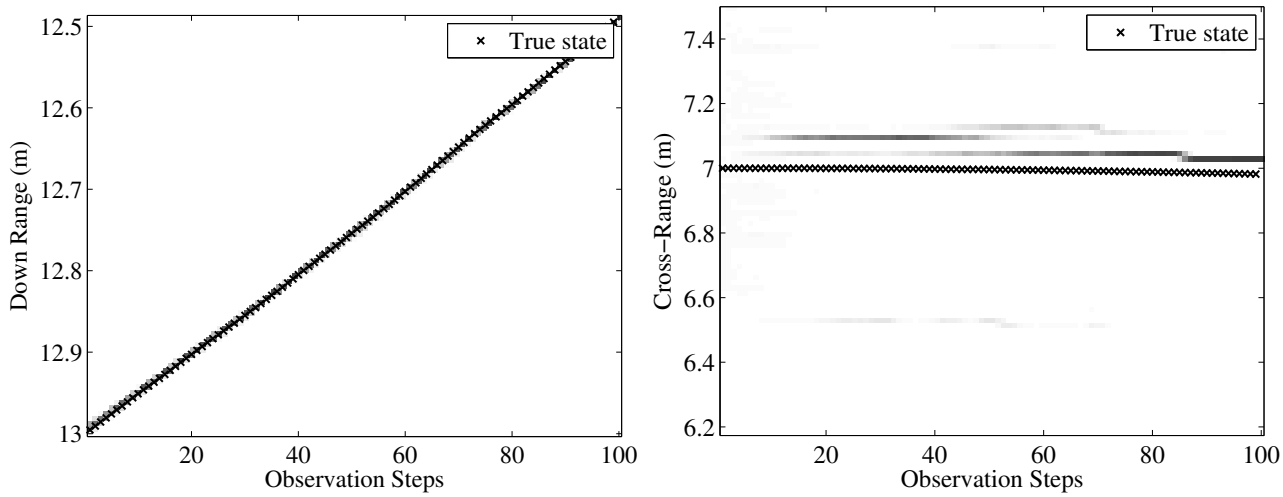

(a) The marginal filtering distribution of $x_6^{\rightarrow}$. Zero of down range dimension shifted to 10000.

(b) The marginal filtering distribution of $x_6^{\perp}$.

Figure 5.45: Marginal filtering distributions for the states associated with dominant scatterer 6 through the BPF.

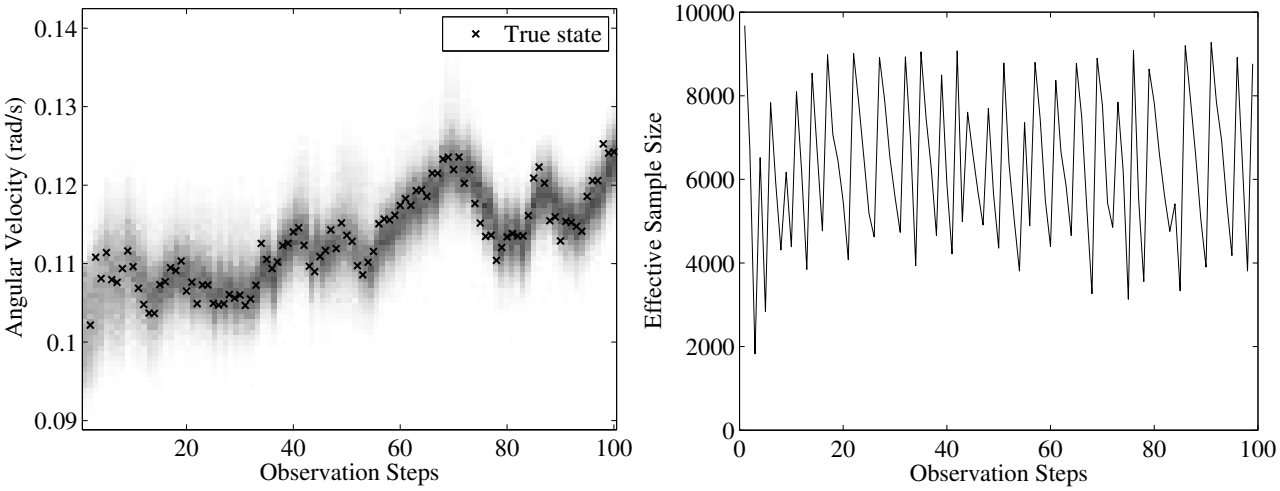

(a) The marginal filtering distribution of ω_r

(b) ESS curve obtained when the BPF with increased observation variance was applied.

Figure 5.46: Marginal filtering distributions of the radial velocity through the BPF, and corresponding ESS curve.

Increasing the observation variance allowed more particles to survive, reducing filter degeneration. This allowed for successful tracking at the expense of an increased error in the inferred estimates. The RMSE was used to measure the consistency of the results obtained. The simulation used to obtain the results in Figures 5.40 to 5.46 was run 50 times. The RMSE was computed for each state over all 50 simulation runs and is given in Table 5.5. Additionally, Table 5.5 also specifies the standard deviation of the RMSE which illustrates to what degree the RMSE varies over the 50 simulation runs.

Table 5.5: RMSE calculated over 50 independent Monte Carlo runs.

State	$x_1^{\rightarrow}$ (mm)	$x_1^{\perp}$ (mm)	$x_2^{\rightarrow}$ (mm)	$x_2^{\perp}$ (mm)	$x_3^{\rightarrow}$ (mm)	$x_3^{\perp}$ (mm)	$x_4^{\rightarrow}$(mm)
RMSE	2.1	81.2	2.3	115.4	2.2	141.5	2.1
σ_{RMSE}	1.4	43.5	0.9	57.5	1.0	76.9	1.1
State	$x_4^{\perp}$ (mm)	$x_5^{\rightarrow}$ (mm)	$x_5^{\perp}$ (mm)	$x_6^{\rightarrow}$ (mm)	$x_6^{\perp}$ (mm)	ω (mrad/s)	
RMSE	122.4	1.8	146.4	1.7	190.5	4.5	
σ_{RMSE}	62.2	0.9	74.6	0.9	102.7	1.6	

The RMSE increases for the estimates in the cross-range states for the dominant scatterers which are

observed to have less motion in the cross-range dimension during the observation period.

At the final time step, the PF approximation of the joint marginal filtering distribution, for all the states relating to the location of the dominant scatterers, was converted into the down range and cross-range dimensions. Plotting this data resulted in a 2D image. The standard technique used in radar to obtain a 2D image of a target undergoing motion utilising HRR profiles obtained from a stationary radar is referred to as ISAR. The two dimensional image obtained from the PF results and from standard ISAR[1] processing utilising the same HRR profiles are presented in Figure 5.47.

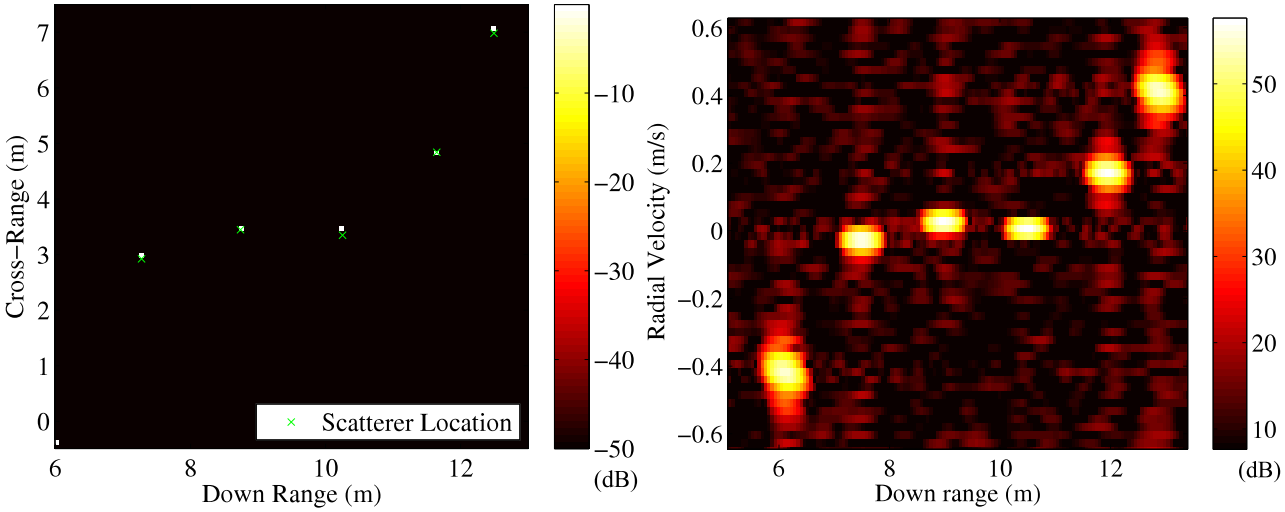

(a) The log marginal filtering distribution for the states corresponding to the locations of the dominant scatterers. Zero of down range dimension shifted to 10000.

(b) ISAR image produced through standard Doppler processing techniques. Zero of down range dimension shifted to 10000.

Figure 5.47: Comparison of the final log marginal filtering distribution to standard ISAR processing.

The effect of decreasing the number of dominant scatterers being tracked was investigated by eliminating dominant scatterers 1 and 3 to 6 of the target illustrated in Figure 5.28. The resulting marginal filtering distributions are illustrated in Figures 5.48 and 5.49.

[1]The standard ISAR processing performed is discussed in Appendix A.

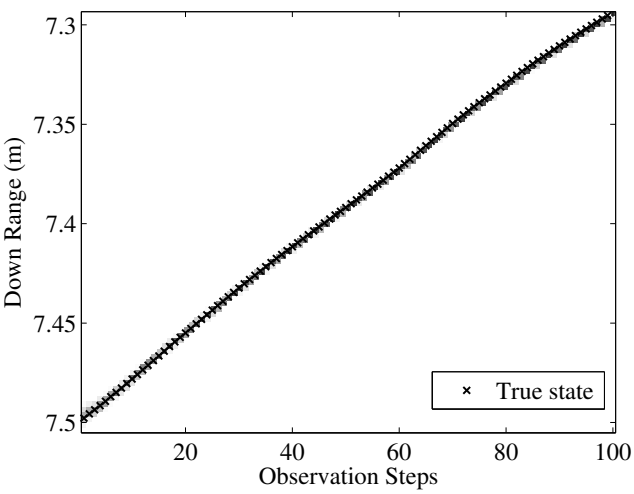

(a) The marginal filtering distribution of $x_2^{\rightarrow}$. Zero of down range dimension shifted to 10000.

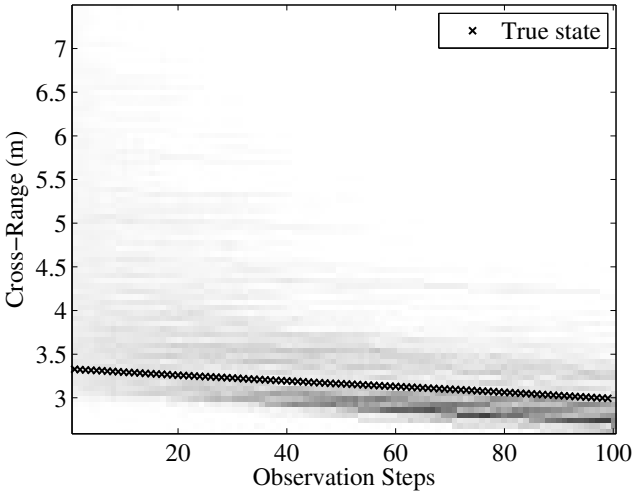

(b) The marginal filtering distribution of $x_2^{\perp}$.

Figure 5.48: The marginal filtering distributions obtained at each time step for Model II, through the BPF, for a target consisting of a single dominant scatterer.

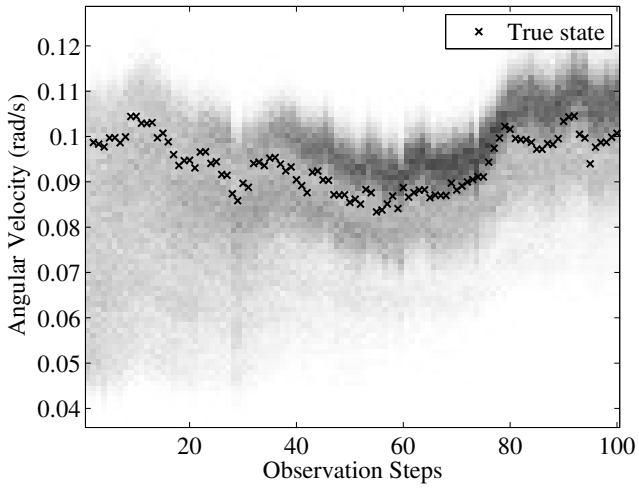

Figure 5.49: The marginal filtering distribution for the angular velocity obtained at each time step for Model II, through the BPF, for a target consisting of a single dominant scatterer.

Decreasing the number of dominant scatterers has the effect of decreasing the dimensionality of the state space. The advantages of decreasing the dimensionality of the state space include:

1. An increase in the ESS, which essentially translates into a better representation of the filtering

distribution given a fixed number of particles.

2. A decrease in computational complexity.

The disadvantage of decreasing the dimensionality of the state space is a larger variance on the filtering distribution as there is less information available at each time step.

CHAPTER 6

CONCLUSIONS & FUTURE WORK

6.1 SUMMARY & CONCLUSIONS

6.1.1 Joint Static Parameter & State Estimation with Range Only Measurements

Section 5.2.2 illustrated that the framework for standard particle filtering does not support the estimation of static parameters. It was shown that by adding the static parameters in the state space leads to severe filter degeneracy. Several different techniques have been proposed to overcome this problem. The PMMH sampler was implemented and successfully estimated the static parameters and states associated with Model I. The disadvantage of the PMMH sampler is the fact that like all standard MCMC methods, it is not a sequential algorithm and thus requires observations from all time steps. The PMMH sampler requires the application of a PF for each MCMC iteration. This leads to a substantial increase in computational time when compared to a PF approach.

The target must undergo a substantial amount of rotation to obtain information about the cross-range location of the dominant scatterers. A full range history for each of the dominant scatterers is required during the time in which measurements are obtained. This was assumed in the simulation, however, in reality this may not be possible due to occlusions and scattering affects which may occur.

6.1.2 State Estimation with Range & Delta Phase Measurements

The introduction of the delta phase measurements substantially decreased the amount of motion required to be observed in order to successfully track the dominant scatterers and the motion of the target.

It was shown that the BPF is better suited than the UPF for applications which contain a prior distribution with a substantially larger variance then the noise perturbing the motion model, a peaked likelihood density and an ambiguous state to observation space mapping. The delta phase observation is highly informative but introduces several challenges due to the ambiguous nature of the observation.

Figure 5.47 compared the results obtained with the PF approach and the standard Doppler processing equivalent. The particles in the PF represent the most likely hypothesis for the true state given the noisy observations, where as the ISAR image contains unwanted artifacts due to Fourier processing. In terms of the PF approach, a tradeoff between accuracy and degeneration of state estimates, dependent on the number of dominant scatterers tracked, was identified. Doppler processing is not dependent on the number of scatterers present in the HRR profiles. The ISAR image is not given directly in terms of the cross-range and further processing would be required to convert the radial velocity dimension into the cross-range dimension. Table 6.1 highlights the differences between ISAR and the PF approach presented.

Table 6.1: A comparison between ISAR and the PF approach presented in this dissertation.

	ISAR	**PF Approach**
Type of scatterers processed	All	Dominant Only
Computational complexity	Low	High
Dimension dependent	N/A	Yes
Dependent on data association	N/A	Yes
Motion parameter estimates	No	Yes
Cross-range directly available	No	Yes
Type of processing	Batch	Batch/Sequential
Extension of results to a 3-D space	Challenging	Straightforward

6.2 PROPOSALS FOR FURTHER RESEARCH

This dissertation has highlighted the advantages and disadvantages of a Monte Carlo approach to the non-linear tracking of an extended target observed by a HRR radar. There are several different avenues available for future research including:

1. Extending the target to a 3-D plane. This would allow for the implementation of a more realistic target.

2. Implementation of a more advanced motion model. Increasing the dimension of the target plane results in several additional degrees of motion.

3. Extending the simulator to account for dominant scatterer occlusions depending on the location of the radar relative to the target.

4. Room for improvement of the filter initialisation procedure.

5. Extension of the filtering framework to accommodate data association and a variable number of dominant scatterers.

6. Extension of the simulator to include clutter and other interference caused by unwanted radar returns from the environment, or by the radar returns from non-dominant scatterers.

7. Extension of the filtering framework to accommodate clutter and other interference.

8. Investigation of techniques that reduce PF degeneration, such as MCMC adaptations [33].

9. The observation model for the phase measurement varies by a large degree when multiple dominant scatterers are present in the same range bin. Extension of the filtering framework to accommodate multiple observation models, as in [63], can be investigated to cater for when dominant scatterers overlap.

10. Investigation of techniques capable of performing joint state and static parameter estimation sequentially [64].

11. Application of the Monte Carlo techniques on real world HRR radar data.

REFERENCES

[1] M. Dixon and G. Wiener, "TITAN: Thunderstorm Identification, Tracking, Analysis, and Nowcasting- Radar-based Methodology," *J. Atmos. Oceanic Technol.*, vol. 10, no. 6, pp. 785–797, Dec. 1993.

[2] I. Bekkerman and J. Tabrikian, "Target Detection and Localization Using MIMO Radars and Sonars," *IEEE Trans. Signal Process.*, vol. 54, no. 10, pp. 3873 –3883, Oct. 2006.

[3] S. Jacobs and J. O'Sullivan, "Automatic target recognition using sequences of high resolution radar range-profiles," *IEEE Trans. Aerosp. Electron. Syst.*, vol. 36, no. 2, pp. 364 –381, April 2000.

[4] D. A. Ausherman, A. Kozma, J. L. Walker, H. M. Jones, and E. C. Poggio, "Developments in Radar Imaging," *IEEE Trans. Aerosp. Electron. Syst.*, vol. AES-20, no. 4, pp. 363 –400, July 1984.

[5] S. S. Blackman, *Multiple-Target Tracking with Radar Applications*. Norwood, MA: Artech House, 1986.

[6] D. R. Wehner, *High Resolution Radar*, 2nd ed. Norwood, MA: Artech House, 1995.

[7] B. Ballard, C. Darron, L. Gostin, B. Hudson, J. Kemp, J. Scheer, and G. Showman, "Dominant scatterer identification testing with an integrated X-band radar system," in *Proc. IEEE Radar Conf.*, May 2001, pp. 18 –22.

[8] M. A. Richards, J. A. Scheer, and W. A. Holm, *Principles of Modern Radar, Volume I - Basic Principles*. SciTech Publishing, 2010.

[9] M. Xing, Z. Bao, and B. Pei, "Properties of high-resolution range profiles," *Optical Engineering*,

vol. 41, no. 2, pp. 493–504, Feb. 2002.

[10] S. Wong, "High Range Resolution Profiles as Motion-Invariant Features for Moving Ground Targets Identification in SAR-Based Automatic Target Recognition," *IEEE Trans. Aerosp. Electron. Syst.*, vol. 45, no. 3, pp. 1017 –1039, July 2009.

[11] W. Nel, E. Giusti, M. Martorella, and M. Gaffar, "A time domain phase-gradient based ISAR autofocus algorithm," in *2011 IEEE CIE Int. Conf. Radar*, vol. 1, Oct. 2011, pp. 541 –544.

[12] J. Li, H. Ling, and V. Chen, "An algorithm to detect the presence of 3D target motion from ISAR data," *Multidim. Syst. Sign. Proc.*, vol. 14, no. 1, pp. 223–240, July 2003.

[13] V. C. Chen and W. J. Miceli, "Effect of roll, pitch, and yaw motions on ISAR imaging," *Proc. SPIE 3810, Radar Proc. Tech. App. IV*, pp. 149–158, Sept. 1999.

[14] W. Nel, D. Stanton, and M. Gaffar, "Detecting 3-D rotational motion and extracting target information from the principal component analysis of scatterer range histories," in *Int. Radar Conf. - Surveilance for a Safer World*, Oct. 2009, pp. 1–6.

[15] Y. Zhang, Y. Xiao, and S. Hu, "3D motion and geometric information system of single-antenna radar based on incomplete 1D range data," *J. Systems Eng. & Electronics*, vol. 22, no. 3, pp. 412–420, June 2011.

[16] L. Hammarstrand, M. Lundgren, and L. Svensson, "Adaptive Radar Sensor Model for Tracking Structured Extended Objects," *IEEE Trans. Aerosp. Electron. Syst.*, vol. 48, no. 3, pp. 1975 –1995, July 2012.

[17] B. Shapo, M. Stuff, C. Kreucher, and R. Majewski, "Detection and tracking of prominent scatterers in SAR data," in *Proc. SPIE*, vol. 8394, no. 83940G, June 2012.

[18] M. Skolnik, *Introduction to Radar Systems*, 3rd ed. McGraw-Hill: New York, 2001.

[19] "IEEE Standard Radar Definitions," *IEEE Std 686-2008 (Revision of IEEE Std 686-1997)*, pp. c1 –41, 21 2008.

[20] L. Du, H. Liu, Z. Bao, and J. Zhang, "A two-distribution compounded statistical model for Radar HRRP target recognition," *IEEE Trans. Signal Process.*, vol. 54, no. 6, pp. 2226 – 2238,

June 2006.

[21] C. Cook and M. Bernfeld, *Radar Signals: An introduction to theory and application*. Norwood, MA: Artech House, 1993.

[22] B. Mahafza, *Radar Systems Analysis and Design Using Matlab*, 2nd ed. Chapman & Hall/CRC, 2000.

[23] S. Bruscoli, F. Berizzi, M. Martorella, and M. Bernabò, "Stepped frequency waveform design with application to SMR," in *14th European Signal Proc. Conf. (EUSIPCO 2006)*, Sept. 2006.

[24] A. Yilmaz, O. Javed, and M. Shah, "Object tracking: A survey," *ACM Comput. Surv.*, vol. 38, no. 4, Dec. 2006.

[25] M. Kolawole, *Radar Systems, Peak Detection and Tracking*. Elsevier Science, 2002.

[26] G. Pulford, "Taxonomy of multiple target tracking methods," *IEE Proceedings Radar, Sonar & Navigation*, vol. 152, no. 5, pp. 291–304, Oct. 2005.

[27] J. Vermaak, S. Godsill, and P. Perez, "Monte Carlo filtering for multi target tracking and data association," *IEEE Trans. Aerosp. Electron. Syst.*, vol. 41, no. 1, pp. 309–332, Jan. 2005.

[28] D. Reid, "An algorithm for tracking multiple targets," *IEEE Trans. Auto. Control*, vol. 24, no. 6, pp. 843–854, Dec. 1979.

[29] R. Karlsson and F. Gustafsson, "Monte Carlo data association for multiple target tracking," in *IEE Target Tracking: Alg. & App.*, vol. 1, Oct. 2001, pp. 13/1–13/5.

[30] H. Gauvrit, J.-P. Le Cadre, and C. Jauffret, "A formulation of multitarget tracking as an incomplete data problem," *IEEE Trans. Aerosp. Electron. Syst.*, vol. 33, no. 4, pp. 1242–1257, Oct. 1997.

[31] Y. Bar-Shalom, X. R. Li, and T. Kirubarajan, *Estimation with Applications to Tracking and Navigation*, 1st ed. Wiley-Interscience, June 2001.

[32] X.-R. Li and V. P. Jilkov, "A survey of maneuvering target tracking: approximation techniques for nonlinear filtering," *Proc. SPIE 5428, Signal & Data Proc. Small Targets*, pp. 537–550, Aug.

2004.

[33] O. Cappe, S. Godsill, and E. Moulines, "An Overview of Existing Methods and Recent Advances in Sequential Monte Carlo," *Proc. IEEE*, vol. 95, no. 5, pp. 899 –924, May 2007.

[34] M. Arulampalam, S. Maskell, N. Gordon, and T. Clapp, "A tutorial on particle filters for online nonlinear/non-Gaussian Bayesian tracking," *IEEE Trans. Signal Proc.*, vol. 50, no. 2, pp. 174 –188, Feb. 2002.

[35] E. A. Wan and R. Van Der Merwe, "The unscented Kalman filter for nonlinear estimation," in *IEEE Com. & Control Symp. Adaptive Systems Signal Proc.* IEEE, Oct. 2000, pp. 153–158.

[36] S. J. Julier and J. K. Uhlmann, "New extension of the Kalman filter to nonlinear systems," in *Proc. of AeroSense: 11th Int. Symp. Aero./Defence Sensing, Sim. & Control*, vol. Multi Sensor Fusion, Tracking and Resource Management II., April 1997, pp. 182–193.

[37] A. Kong, J. S. Liu, and W. H. Wong, "Sequential Imputations and Bayesian Missing Data Problems," *J. Amer. Statist. Assoc.*, vol. 89, no. 425, pp. 278–288, March 1994.

[38] D. B. Rubin, "A noniterative sampling/importance resampling alternative to the data augmentation algorithm for creating a few imputations when fractions of missing information are modest: the SIR algorithm," *J. Amer. Statist. Assoc.*, vol. 82, no. 398, pp. 543–546, June 1987.

[39] N. Gordon, D. Salmond, and A. Smith, "Novel approach to nonlinear/non-Gaussian Bayesian state estimation," *IEE Proc. F Radar and Signal Proc.*, vol. 140, no. 2, pp. 107–113, April 1993.

[40] J. S. Liu, *Monte Carlo Strategies in Scientific Computing*. New York: Springer, Jan. 2008.

[41] J. D. Hol, T. B. Schon, and F. Gustafsson, "On Resampling Algorithms for Particle Filters," in *2006 IEEE Nonlinear Stat. Signal Proc. Workshop*, Sept. 2006, pp. 79 –82.

[42] R. van der Merwe, N. de Freitas, A. Doucet, and E. Wan, "The Unscented Particle Filter," in *Advances Neural Inf. Proc. Systems 13*, Nov. 2001.

[43] F. Daum and J. Huang, "Curse of dimensionality and particle filters," in *2003 IEEE Proc. Aero. Conf.*, vol. 4, March 2003, pp. 4–1979 – 4–1993.

[44] A. Doucet, N. Gordon, and V. Krishnamurthy, "Particle filters for state estimation of jump Markov linear systems," *IEEE Trans. Signal Proc.*, vol. 49, no. 3, pp. 613 –624, March 2001.

[45] A. Doucet, S. Godsill, and C. Andrieu, "On sequential Monte Carlo sampling methods for Bayesian filtering," *Statistics & Computing*, vol. 10, no. 3, pp. 197–208, July 2000.

[46] M. Isard and A. Blake, "CONDENSATION - Conditional Density Propagation for Visual Tracking," *Int. J. Computer Vision*, vol. 29(1), pp. 5–28, Aug. 1998.

[47] M. K. Pitt and N. Shephard, "Filtering via Simulation: Auxiliary Particle Filters," *J. Amer. Statist. Assoc.*, vol. 94, no. 446, pp. 590–599, June 1999.

[48] J. Carpenter, P. Clifford, and P. Fernhead, "An improved particle filter for non-linear problems," *IEE Proc. Radar, Sonar & Navigation*, vol. 146, pp. 2–7, Feb. 1999.

[49] A. M. Johansen and A. Doucet, "A note on auxiliary particle filters," *Statist. & Probability Lett.*, vol. 78, no. 12, pp. 1498 – 1504, Sept. 2008.

[50] S. Julier, "The scaled unscented transformation," in *Proc. 2002 Amer. Cont. Conf.*, vol. 6, May 2002, pp. 4555–4559.

[51] J. Olsson, O. Cappé, R. Douc, and Éric Moulines, "Sequential Monte Carlo smoothing with application to parameter estimation in nonlinear state space models," *Bernoulli*, Feb. 2008.

[52] H. K. Hurzeler, M, *Sequential Monte Carlo Methods in Practice*. New York: Springer, 2001, ch. Approximating and maximising the likelihood for a general state space model, pp. 159–175.

[53] G. Kitagawa, "A self-organizing state-space model," *J. of the Amer. Statist. Assoc.*, pp. 1203–1215, Sept. 1998.

[54] W. Wan-ping, L. Sheng, and X. Ting-wen, "Particle filter for state and parameter estimation in passive ranging," in *IEEE Int. Conf. Intelligent Computing & Intelligent Systems, ICIS 2009.*, vol. 3, Nov. 2009, pp. 257–261.

[55] G. Storvik, "Particle filters for state-space models with the presence of unknown static parameters," *IEEE Trans. Signal Proc.*, vol. 50, no. 2, pp. 281–289, Feb. 2002.

[56] C. Andrieu, A. Doucet, and V. Tadic, "On-Line Parameter Estimation in General State-Space Models," in *44th IEEE Conf. Decision & Control, 2005 & European Control Conf. CDC-ECC '05.*, Dec. 2005, pp. 332 – 337.

[57] C. Andrieu, A. Doucet, and R. Holenstein, "Particle Markov chain Monte Carlo methods," *J. R. Stat. Soc. Ser. B Stat. Methodol.*, vol. 72, no. 3, pp. 269–342, June 2010.

[58] D. A. Cook, "Synthetic Aperture Sonar Motion Estimation and Compensation," Master's thesis, School of Electrical and Computer Engineering, Georgia Institute of Technology, 2007.

[59] A. De Freitas and J. De Villiers, "Multiple scatterer tracking in high range resolution radar," in *15th Int. Conf. Information Fusion*, July 2012, pp. 1683–1688.

[60] P. Stoyle, "Point scatterers in radar imaging," in *Proc. SPIE*, vol. 3462, Oct. 1998.

[61] M. Y. A. Gaffar, "Maritime Classification Processor: Report on TD0.5 alpha trial," CSIR, Tech. Rep. 5840-HADAS-10017, Jan. 2011.

[62] Y. Wang and B. Chaib-draa, "An adaptive nonparametric particle filter for state estimation," in *IEEE Int. Conf. on Robotics and Automation*, May 2012, pp. 4355–4360.

[63] F. Caron, M. Davy, E. Duflos, and P. Vanheeghe, "Particle Filtering for Multisensor Data Fusion with Switching Observation Models: Application to Land Vehicle Positioning," *IEEE Trans. Signal Proc.*, vol. 55, pp. 2703–2719, June 2007.

[64] N. Chopin, P. E. Jacob, and O. Papaspiliopoulos, "SMC2: an efficient algorithm for sequential analysis of state space models," *J. R. Stat. Soc. Ser. B Stat. Methodol.*, vol. 75, no. 3, pp. 397–426, June 2013.

[65] B. Haywood and R. J. Evans, "Motion compensation for ISAR imaging," in *Proc. of ASSPA '89*, April 1989, pp. 113–117.

[66] B. D. Steinberg, "Microwave imaging of aircraft," in *Proc. IEEE*, vol. 76, Dec. 1988, pp. 1578–1592.

APPENDIX A

ISAR PROCESSING

The processing performed to obtain the ISAR image in Chapter 5 is separated into three steps:

1. Radial motion compensation,

2. auto focusing,

3. and Doppler processing.

A discrete HRR profile is represented in vector form

$$\boldsymbol{r} = \begin{bmatrix} A_1 e^{j\theta_1} & \dots & A_N e^{j\theta_N} \end{bmatrix}, \tag{A.1}$$

where $A_n e^{j\theta_n}$ is the polar form of the complex value in range bin n, N is the total number of range bins and $n = [1,\dots,N]$. A set of HRR profiles is represented as a matrix

$$\begin{bmatrix} \boldsymbol{r}_1 \\ \vdots \\ \boldsymbol{r}_M \end{bmatrix} = \begin{bmatrix} A_{11} e^{j\theta_{11}} & \dots & A_{1N} e^{j\theta_{1N}} \\ \vdots & A_{mn} e^{j\theta_{mn}} & \vdots \\ A_{M1} e^{j\theta_{M1}} & \dots & A_{MN} e^{j\theta_{MN}} \end{bmatrix} \tag{A.2}$$

where M is the total number of discrete HRR profiles and $m = [1,\dots,M]$. Haywood's ISAR motion compensation algorithm [65] was firstly applied to the set of HRR profiles, in order to perform radial motion compensation. This is achieved by firstly identifying the range profile which contains the maximum amplitude value, A_{mn}, in the matrix. The corresponding range profile is selected as the reference HRR profile, $\boldsymbol{r}_{ref}$. Each of the HRR profiles are then correlated with the reference HRR profile,

$$\boldsymbol{c}_m = \text{corr}(\boldsymbol{r}_{ref}, \boldsymbol{r}_m) \qquad \forall m = 1,\dots,M. \tag{A.3}$$

The location corresponding to the maximum correlation indicates the number of range bins that are required to be shifted for alignment with the reference HRR profile,

$$d_m = -\text{location}[\max(\boldsymbol{c}_m)] - M \qquad \forall m = 1,\ldots,M. \tag{A.4}$$

However, the bin shifts are not smooth and hence a low order polynomial is fit to the range bin shifts, $d_1,\ldots,d_M$.

$$s_m = \text{polyfit}(d_m) \qquad \forall m = 1,\ldots,M. \tag{A.5}$$

The smoothed shifts are applied to each of the HRR profiles in the frequency domain

$$\boldsymbol{r}'_m = \text{IFFT}\left(\boldsymbol{\Phi}\text{FFT}\left(\left[\begin{array}{ccccc} A_{m1}e^{j\theta_{m1}} & \ldots & A_{mN}e^{j\theta_{mN}} \end{array}\right]\right)\right), \tag{A.6}$$

where FFT and IFFT represent the FFT and inverse FFT operations respectively, and $\boldsymbol{\Phi}$ is the phase shift vector

$$\boldsymbol{\Phi} = \left[\begin{array}{ccccc} e^{\frac{j2\pi s_m}{N}} & \ldots & e^{\frac{j2\pi n s_m}{N}} & \ldots & e^{j2\pi s_m} \end{array}\right]. \tag{A.7}$$

The range aligned HRR profiles are then compensated for phase changes caused by range shifts which are only fractions of a wavelength. The auto focusing method used to achieve this was the dominant scatterer algorithm (DSA) [66]. The DSA utilises the phase of a single dominant scatterer to compensate the phase of all the range aligned HRR profiles. Firstly the amplitude variance for each range bin is calculated over all the HRR profiles. The range bin with the minimum amplitude variance, b_{ref}, is considered to consist of a dominant scatterer and is utilised as the phase synchronising source. The phase of each HRR profile is then compensated according to the phase of the reference range bin

$$\boldsymbol{r}''_m = e^{-j\theta_{b_{ref}}}\boldsymbol{r}'_m. \tag{A.8}$$

After phase compensation, the phase of the reference range bin is constant. The final step is to perform Doppler processing on the auto focused range aligned HRR profiles. Prior to the Doppler processing, a Chebyshev window, with a sidelobe magnitude of 45 dB below the mainlobe magnitude, was applied to the auto focused range aligned HRR profiles. The Doppler processing then consisted of the application of a one-dimensional FFT on each range bin of the set of processed HRR profiles.